Shape Coexistence in the Proton-Unbound Nucleus ^{177}Au

Thesis submitted in accordance with the requirements of the University of Liverpool for the degree of Doctor in Philosophy

by

Fuad Arif Ali

Oliver Lodge Laboratory

2014

This thesis is dedicated to my mother, Rakhta, my father, Arif,

to my wife, Kashan,

and to my children, Maile and Mina.

Abstract

Excited states of the proton-unbound nucleus ^{177}Au have been populated following the ^{92}Mo(^{88}Sr,2pn) reaction in an experiment performed at the University of Jyväskylä Accelerator Laboratory. Gamma rays detected in the JUROGAM spectrometer were correlated with the characteristic α decays of ^{177}Au detected following a recoil implantation in the GREAT spectrometer. A large number of transitions ($\sim$ 60 γ rays) have been assigned unambiguously to ^{177}Au and ordered into four collective band structures and other single-particle excitations. Several intruder configurations formed by single-proton excitations across the $Z = 82$ shell gap have been established. These have been interpreted as $\pi i_{13/2}$, $\pi f_{7/2} \oplus h_{9/2}$ and $\pi h_{9/2}$ prolate configurations. It has been established that the $\pi i_{13/2}$ and $\pi f_{7/2} \oplus h_{9/2}$ bands have decay paths to both the positive-parity mixed ($1/2^+ \oplus 3/2^+$) ground state and the negative-parity $11/2^-$ isomer, which is unusual in this mass region. Structures based on the coupling of the odd π $h^{-1}_{11/2}$ proton hole to excitations of the ^{178}Hg core have been established in the excitation level scheme. An oblate $\pi h^{-1}_{11/2} \otimes {}^{178}\mathrm{Hg}(2^+_1)$ state and a prolate strongly coupled band based on the $\pi h^{-1}_{11/2} \otimes {}^{178}\mathrm{Hg}(0^+_2)$ configuration have been identified. The decay paths from the strongly coupled band and the search for evidence of electric monopole decays are discussed.

Acknowledgements

First of all I would like to show my gratitude to my supervisors Dr David Joss and Professor Rodi-Herzberg for allowing me to undertake this research at the University of Liverpool. I would like to thank them for their invaluable support, patience and guidance during my studies as a PhD student. I also wish to thank Professor Robert Page for his help in providing further support in my analysis as well as proof-reading parts of my thesis.

Many thanks to my wife, Kashan, and my children Maile and Mina, who have always been there for me throughout turbulent times. Their love and patience has been unwavering throughout my life; without you this work would have not been possible.

I would especially like to thank my dearest father, Arif Ali, my mother, Rakhta Yousuf, my beloved sisters Renas, Hawra and Dekan, and to my brothers Hama, Zana and Hamed for their love and encouragement during my studies.

I would like to sincerely acknowledge the receipt of funding from the Ministry of Higher Education in the Kurdistan Region, Iraq, through the Human Capacity Development Program (HCDP).

I wish to thank all of my fellow PhD students and the post-doctoral staff in the nuclear physics group that I have worked with in the Department of Physics. Whilst working at the University, I have benefited from the support of several very helpful people, which include Daniel Cox, Rob Carroll, John Revill, Alex Thornthwaite, Andrew Mistry, Peter Hampson, Joe McKenna, Amina Patel, Christopher McPeake and Faye Wearing for their kind support and patience within the past three and half years. l wish you all the best of luck for the future.

Thanks to all the staff at the Physics Department of the University of Jyväskylä for the help and hospitality they have provided, particularly Professor Paul Greenlees for his dedication and expert input during the times I visited the JYFL Accelerator Laboratory. I would like to acknowledge all of the collaborators involved in this research especially Dr

Martin Venhart from the Slovak Academy of Sciences and Professor John Wood from the Georgia Institute of Technology.

Finally, a special thanks goes to all of the other people I have not mentioned above but have also provided support to me during my studies.

Contents

List of Figures

List of Tables

Chapter 1

Introduction

The atomic nucleus is a unique ensemble of strongly interacting fermions. The Segrè chart shown in the Fig. 1.1 displays around three thousand unique ensembles of protons and neutrons that occur naturally or have been synthesised in nuclear reactions. Considerable experimental and theoretical efforts have been made to understand the structure of exotic nuclei at the extremes of the nuclear landscape. This thesis provides new information on the structure of the neutron-deficient nuclide ^{177}Au, which lies on the proton-drip line - the locus of points where the proton separation energy changes sign and the nucleus becomes unbound to proton emission. This thesis aims to provide information on the relative locations of single-particle orbitals near the drip line through the study of single-proton excitations that are manifested through the phenomenon of shape coexistence in ^{177}Au.

The excitations of the nucleus can arise from the rearrangement and coupling of single particles or through the large-scale collective motion of its constituent nucleons. The origin of collective motion in atomic nuclei from the complicated interactions of their constituent protons and neutrons is a central theme in nuclear physics [1, 2]. A key manifestation of coherent behaviour in nuclei is the coexistence of several distinctly deformed configurations that lie within a range of excitation energies that is narrow when compared with the mass scale of the nucleus (*c.f.* $\sim$800 keV compared to $\sim 1\times10^{8}$ keV) [3]. Coexisting structures are sensitive to the interplay between the stabilising presence of shell gaps and the

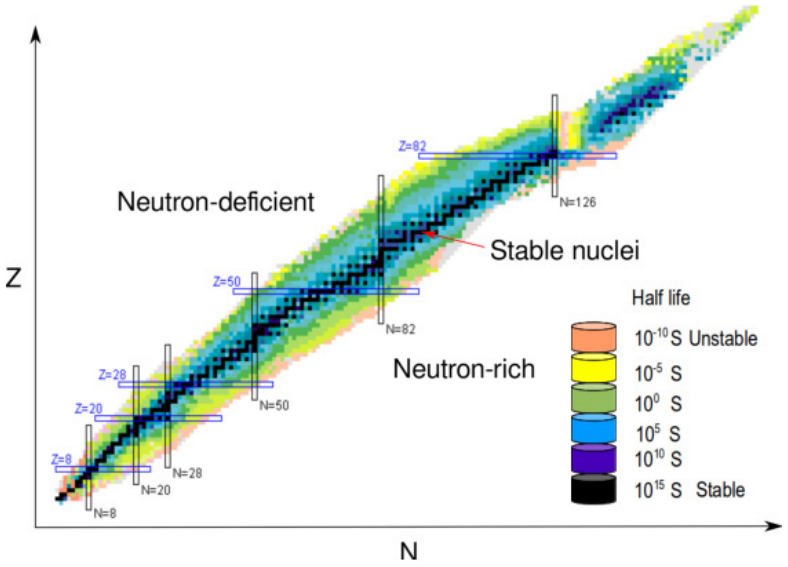

Figure 1.1: The chart of nuclides showing the stable, neutron-rich and the neutron-deficient nuclides.

deformation-driving tendencies of residual interactions between single-particle orbitals [3]. Spectroscopic measurements of excited states in odd-Z nuclei like ^{177}Au provide a sensitive probe of the single-proton states below and above the $Z = 82$ shell gap. The single-proton (hole) configurations formed by rearranging the odd-proton about the $s_{1/2}, d_{3/2}$ and $h_{11/2}$ orbitals below the shell gap and the $h_{9/2}, f_{7/2}$ and $i_{13/2}$ intruder states above it provide unique information about the relative excitation energy of the single-particle configurations in a proton unbound nucleus. Consequently, experimental observations of coexisting structures provide stringent constraints on contemporary theoretical frameworks that describe nuclear structure [4, 5, 6, 7, 8].

The most extensively characterised region of low-energy shape coexistence is found in the vicinity of the $Z = 82$ proton shell gap and the neutron midshell at $N = 104$ [3]. Since the discovery of the phenomenon in the Hg isotopes [9], shape coexistence has been well established in many even-even nuclei below the $Z = 82$ proton shell gap including the Pb [10, 11], Hg [9, 12], Pt [13], Os [14] and W [15] isotopes. However, a comprehensive knowledge of shape coexistence in lightest odd-Z nuclei such as Tl and Au has not yet been achieved since odd-Z nuclei can exhibit more complicated excitation spectra than their doubly even neighbours. Moreover, the more neutron-deficient isotopes are synthesised

with low production cross sections following fusion evaporation reactions, which can also produce large γ-ray and radioactive decay backgrounds arising from other reaction channels including fission. However, there are experimental signatures of shape coexistence at low spin in the neutron-deficient Au isotopes from in-beam and decay spectroscopy measurements [16, 17, 18, 19, 20, 21] where rotational bands based on proton intruder and hole configurations have been observed.

To overcome the experimental challenges presented by low production cross sections and high γ-ray backgrounds a recoil-decay tagging [22, 23, 24] experiment has been performed at the University of Jyväskylä Accelerator Laboratory. The experiment exploited the JUROGAM γ-ray multi-detector array [25] combined with the Recoil-Ion-Transport-Unit- Separator [26, 27, 28, 29] and the GREAT focal-plane detector [30] in conjunction with the Total-Data-Readout data acquisition system [31]. The experiment enabled the extension of the excitation level scheme of ^{177}Au nuclei to include new collective bands associated with $\pi h_{9/2}$ and $\pi f_{7/2}$ intruder configurations and the $h^{-1}_{11/2}$ proton hole structures.

The subsequent chapters are detailed hereafter. Chapter 2 describes the theoretical background underlying the current work, in particular the appropriate models for nuclear structure and the decay modes as well as a brief description of the shape coexistence phenomenon. Chapters 3 highlight the aspects related to the experimental methodology and apparatus. Chapter 4 presents the results and their interpretation. Finally, Chapter 5 presents a summary of the main findings and the prospects for future work.

Chapter 2

Concepts in Nuclear Physics

2.1 Nuclear Models

The observable properties of the atomic nucleus arise from the complex interactions between nucleons. This many-body problem is often intractable from an analytical perspective, particularly for large nucleon numbers, and we rely on models that incorporate an average potential (mean field) with an effective interaction to reproduce observable features. Often nuclear models can be limited in their descriptions across the range of the nuclear chart and modifications to specific formalisms may be required. In this chapter, the fundamental background physics relevant to this work is presented. In the following sections a brief explanation of the Liquid Drop model, Shell Model and Nilsson Model are presented.

2.1.1 Liquid Drop Model

The liquid drop model was the first classical macroscopic model of the atomic nucleus [32, 33, 34]. This model treats the nucleus as a spherical charged liquid drop of well defined density and radius. The model has been successful in providing insights into the fission and fusion process, collective effects such as vibrations and rotations and reproduces the general variation of the binding energy for most nuclei, see equation 2.1. The semi-empirical mass formula [32, 33] expresses the binding energy in terms of the relative contributions of the

geometry (volume and surface), charge and quantum effects (asymmetry and pairing) such that

$$B_E(A,Z) = a_v A - a_s A^{2/3} - a_c Z^2 A^{1/3} - a_i (A-2Z)^2 A^{-1} \pm \delta, \tag{2.1}$$

where a_v,a_s,a_c, a_i are coefficients related to the volume, surface, Coulomb and asymmetry terms, respectively. The pairing term δ can take positive, zero or negative values for even-even, odd-even and odd-odd nuclei, respectively. However, the nuclear binding energy can be enhanced at certain 'magic' proton and neutron numbers suggesting that the liquid drop model is not incorporating all features relevant to a global description of the nuclear structure. The measurements of nucleon separation energies, nuclear charge radii and the first excited state of the nucleus indicated that the nucleus exhibits a shell structure analogous to that observed in the electronic structure of atoms. These empirical data resulted in the development of the nuclear shell model, which assumes that the nucleons move independently in a nuclear potential generated by the interactions of all constituent nucleons.

2.1.2 Shell Model

Generating a nuclear potential arising from inter-nucleon interactions in a many-body system comprising a large number of interacting nucleons is often intractable from an analytical perspective. In an effort to explain the variations of nucleon separation energies and other empirical data, Mayer [35] and Haxel, Jensen and Suess [36] independently developed the nuclear shell model, which considered each particle moving independently in a uniform average potential $V(r)$ created by the interactions of all the other nucleons. There are different formulations of the nuclear potential ranging from the square well and harmonic oscillator potentials that are easily solvable to more realistic potentials such as the Woods-Saxon potential [37]. A selection of different potentials is shown in Figure 2.1.

The Woods-Saxon potential is defined as

$$V(r) = \frac{-V_0}{1 + exp[\frac{r-R}{a}]}, \tag{2.2}$$

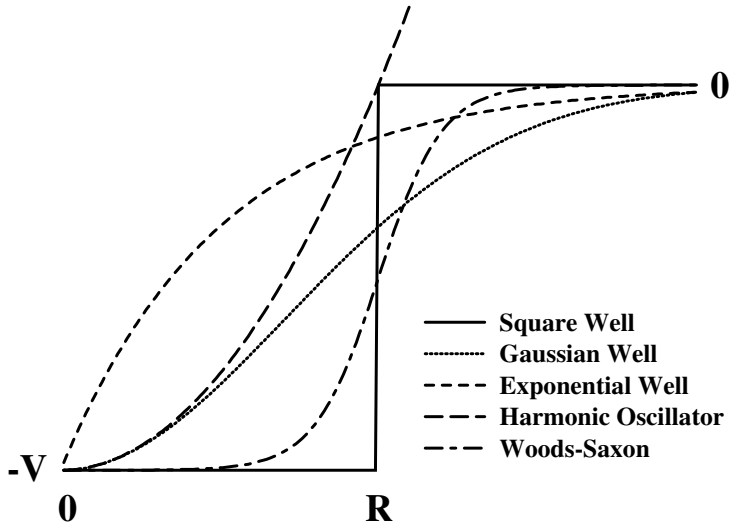

Figure 2.1: Comparison of different potential wells. This figure is reproduced courtesy of E.S Paul [38].

where V_0 refers to the well depth, $[r - R]$ are the nuclear radii and a is the surface diffuseness. This formulation provides a reasonable description of a mean field potential generated from a short-range interaction between nucleons and the diffuseness of the nuclear surface. The Woods-Saxon potential reproduces the first three magic numbers.

The Woods-Saxon potential must be modified to provide a better description of heavier nuclei. This modification takes into account the interaction occurring between the nucleon intrinsic spin, s, and orbital angular momentum l [36, 39]. This modification to include the spin-orbit interaction can be written as

$$V = V(r) + V_{l.s}(r). \tag{2.3}$$

Figure 2.2 shows how the incorporation of the $l.s$ term to the potential reproduces the magic numbers observed experimentally. The spherical shell model is most applicable for describing single-particle excitations near closed shells. Nuclei with large numbers of valence nucleons exhibit collective excitations at low energy and the spherical shell model is no longer applicable.

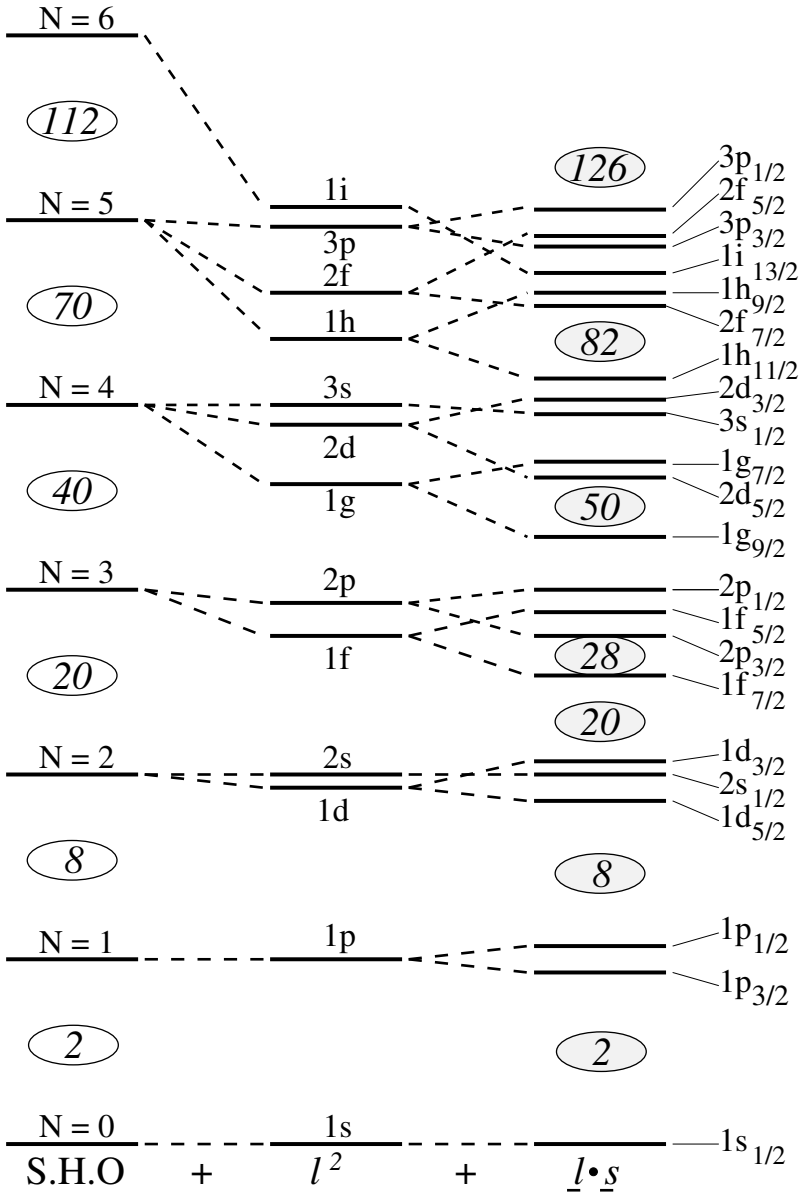

Figure 2.2: A pictoral representation of single particle energy eigenvalues using the Woods-saxon potential before (left) and after (right) the spin-orbit term is introduced. Figure is reproduced from Reference [38]

2.2 Deformation and Rotation

2.2.1 Nuclear Deformation

In the vicinity of closed shells, the nucleus is spherical due to the fact that the nucleonic orbits are oriented isotropically. However, away from the closed shells the nucleus is susceptible to deformation because of the correlations between valence nucleons. The onset of deformation relieves the degeneracy of the shell model states and the competition between the polarising power of nucleons in specific orbitals and the pairing forces drives the nuclear shape equilibrium from spherical to ellipsoidal shapes. The nuclear shape is defined in polar coordinates by the radius $R(\theta, \phi)$ of the nucleus [40] expanded into spherical harmonics $Y_\lambda^\mu(\theta, \phi)$

$$R(\theta, \phi) = R_0 \left[1 + \alpha_{00} + \sum_{\lambda=1}^{\infty} \sum_{\mu=-\lambda}^{\lambda} \alpha_{\lambda\mu} Y_\lambda^\mu(\theta, \phi) \right], \tag{2.4}$$

where α_{00} is a coefficient that constrains the nucleus to have a constant volume, R_0 is the radius of the spherical nucleus of the same volume and the $\alpha_{\lambda\mu}$ are the Hill-Wheeler coordinates [41] that define the distortion from an equilibrium spherical shape. The symbol, λ, corresponds to the multipolarities in the expansion in equation 2.4: $\lambda = 0$ and 1 represents only the expansion and contraction of the whole surface. For small deformations $\lambda = 2, 3, 4$ correspond to quadrupole, octupole and hexadecapole degrees of freedom, respectively.

The Hill-Wheeler coordinates, $\alpha_{\lambda\mu}$, are related to the quadrupole deformation parameter β_2 and β_4 allowing the expansion in equation 2.4 to be written as

$$R(\theta) = CR_0 \left[1 + \sqrt{\tfrac{5}{4\pi}} \beta_2 P_2(\cos\theta) + \sqrt{\tfrac{9}{4\pi}} \beta_4 P_4(\cos\theta) \right], \tag{2.5}$$

where P_2 and P_4 are Legendre polynomials.

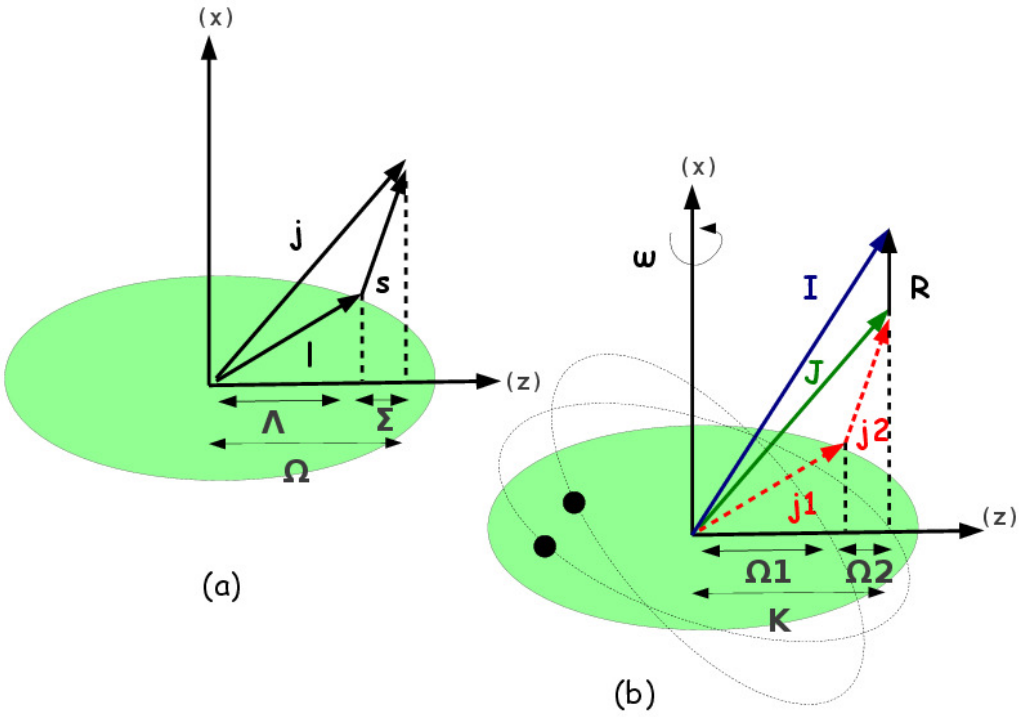

Figure 2.3: (a) Schematic illustration of the total angular momentum for a single valence particle. (b) Schematic illustration of the coupling of two valence nucleons to the collective rotation of the core in a defomed nucleus.

2.2.2 Nuclear Rotation

An axially deformed nucleus can be considered as a core surrounded by valence nucleons. Figure 2.3(a) shows a schematic coupling of the single-particle intrinsic spin, s with the orbital angular momentum, l, resulting in the vector sum of j. The projections of s and l onto the symmetry axis (z) are denoted by Λ and Σ, respectively. Figure 2.3(b) indicates the coupling of single-particle angular momentum vectors j_1 and j_2 to the angular momentum of the core R. The total intrinsic angular momenta J is

$$J = \sum_i j_i, \tag{2.6}$$

while the vector sum of the individual single-particle projections on the symmetry axis yields, K, where

$$K = \sum_i \Omega_i. \tag{2.7}$$

Nuclear rotation about an axis perpendicular to the symmetry axis (z) produces a total angular momentum (I) that is equal to the vector sum of the angular momenta of the rotating core (R) and the individual valence nucleons outside the deformed core (J), which can be expressed as

$$I = R + J. \tag{2.8}$$

The relation between energy and the angular momentum in a rotating axially deformed nucleus is expressed as

$$E_{rot}(I) = \frac{\hbar^2}{2\Im^{(0)}} I(I+1), \tag{2.9}$$

where $\Im^{(0)}$ is the static moment of inertia [42]. Equation 2.9 reproduces the typical $I(I+1)$ level spacings observed in rotational bands. Experimentally a direct measurement of the differences between various configurations built on distinct band heads can be found by plotting the kinematic moment of inertia as a function of rotational frequency.

2.2.3 Nilsson Model

Most nuclides are located at non-magic numbers and are expected to have some degree of deformation. The magnitude of deformation can have a great influence on the single-particle energies particularly for high-j orbitals experiencing the spin-orbit interaction. The Nilsson Model [43] is based on axially deformed harmonic oscillator potential. The variation of the single-particle energy of the nuclear states as a function of quadrupole deformation is calculated and presented in Figure 2.4. Such plots of the single-particle energy against deformation parameter are known as Nilsson diagrams (usually irrespective of the potential adopted). Each state in the Nilsson diagram is identified by the asymptotic quantum numbers

$$\Omega^{\pi}[Nn_z\Lambda], \tag{2.10}$$

where π is the parity of the state, N is principal quantum number and n_z is number of oscillator quanta along the symmetry axis. The projection of total angular momentum onto symmetry axis Ω is defined as $\Sigma + \Lambda = \Lambda + \frac{1}{2}$ as shown in Fig. 2.3(a). Each level in the Nilsson diagram may be occupied by two degenerate nucleons in time-reversed orbits

of projections $\pm\Omega$. The onset of deformation relieves the degeneracy of the spherical shell model states, which are split according to their spatial orientations relative to the axially symmetric core. For prolate shapes ($\epsilon_2 > 0$), the low-Ω projections have the largest overlap with the core and are lowered in energy. For oblate shapes ($\epsilon_2 < 0$), the converse is true. Orbitals with high-j are lowered by the spin-orbit interaction so that they can be lowered in energy until they intrude into the shell below. These unnatural parity states are often called intruder orbitals and are particularly relevant to this work.

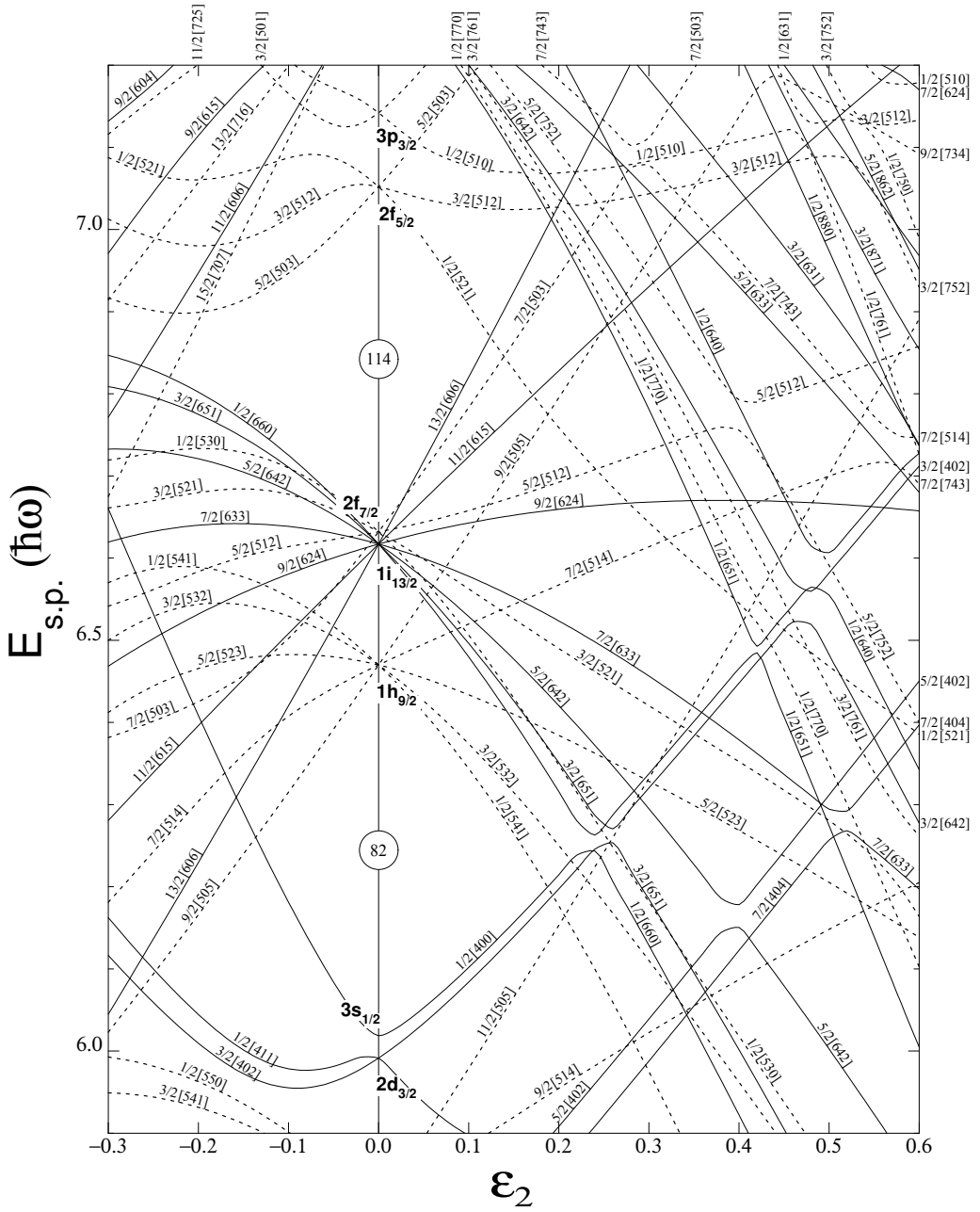

Figure 2.4: Nilsson Diagram for the protons in the $Z = 82$ region [44]. The diagram shows how the degeneracy of the spherical shell model single-particle states is relieved as a function of quadrupole deformation ϵ_2. The deformation parameter ϵ_2 and its relationship to the related parameter β_2 is given in reference [45].

2.3 Electromagnetic Transitions

Nuclear reactions and decays can synthesise a nucleus in an excited state. There are two principal electromagnetic mechanisms by which an excited nucleus can lose energy and angular momentum in a transition from an initial state to a final state; these are γ-ray emission or internal conversion.

2.3.1 Gamma-ray transitions

An excited nucleus may de-excite from an initial state with spin and parity I_i^π to a final state I_f^π by the emission of a γ-ray photon. Since energy is conserved in this process the difference between the excitation energies of the two states is approximately given by the energy of the γ-ray transition E_γ where

$$E_\gamma = E_i - E_f. \tag{2.11}$$

In classical physics, changing charge and current distributions generate fluctuating electric and magnetic fields that result in the emission of electromagnetic radiation. The radiation field can be described in terms of a multipole expansion where the terms depend on the multipole moments $M(\sigma L)$ where σ denotes electric or magnetic character and L is the multipole order. Weisskopf estimated the transition probability due to a single nucleon changing orbital [46], which can be deduced from time dependent perturbation theory as

$$T_{f\to i}^{(\sigma L)} = \frac{8\pi}{\hbar}\frac{L+1}{L[(2L+1)!!]^2}\left(\frac{E_\gamma}{\hbar c}\right)^{2L+1} B(\sigma L; I_i \to I_f), \tag{2.12}$$

where $B(\sigma L; I_i \to I_f)$ is the reduced transition probability, which is defined as

$$B(\sigma L; I_i \to I_f) = \frac{1}{2I_i+1}|\langle I_f|\, M(\sigma L)\, |I_i\rangle\,|^2, \tag{2.13}$$

where $|\langle I_f|\, M(\sigma L)\, |I_i\rangle\,|^2$ is the reduced matrix element. Selection rules for γ-ray emission are obtained from these matrix elements and the conservation of angular momentum such

that

$$|I_i - I_f| \leq L \leq I_i + I_f. \tag{2.14}$$

Moreover, parity conservation imposes further restrictions for electric and magnetic transitions such that

$$\Delta\pi(EL) = (-1)^L, \tag{2.15}$$

$$\Delta\pi(ML) = (-1)^{L+1}. \tag{2.16}$$

Hence, transitions with $E1, M2, E3, M4, ...$ multipolarities are parity changing while transitions with $E0, M1, E2, M3, E4, ...$ are not[1]. Equation 2.14 implies that several multipolarities may be allowed in a transition between two states, however the lower multipole orders are favoured due to their larger transition probabilities. Transitions of mixed multipolarity are also allowed. Various experimental methods allow the distinction of different γ-ray multipolarities such as the measurement of angular distributions and linear polarizations [47].

The Weisskopf estimates are related to the reduced matrix element and may be used to compare with experimental measurements of transition rates to determine whether a transition has a single-particle origin or collective contributions exist. Table 2.1 shows estimated value of the transition probabilities and reduced transition probabilities for different multipole orders. It should be noted that for the transition rates for electric mutipoles are greater than for magnetic transitions of the same order.

Changes in nuclear structure can be observed from the transition rates. For instance, the reduced transition probability for $E2$ transitions is dependent on the electric charge distribution or quadrupole moment Q_0. The $B(E2)$ is defined as

$$B(E2; I_i \rightarrow I_f) = \frac{5}{16\pi} e^2 Q_0^2 |\langle I_i K_i 20 | I_f K_f \rangle|^2, \tag{2.17}$$

whereas $M1$ transitions depend on the difference in intrinsic and rotational gyromagnetic

[1] $M0$ transitions do not occur since there are no magnetic monopoles and $E0$ decays proceed only by internal conversion as a consequence of angular momentum conservation.

σ L	Transitions Probabilities (s^{-1})	Weisskopf Units (s^{-1})
E1	$T(E1) = 1.587 \times 10^{15}$. $B(E1)$. E^3	$B_{sp}(E1) = 1.0 \times 10^{14}$. $A^{\frac{2}{3}}$. E^3
E2	$T(E2) = 1.223 \times 10^{9}$. $B(E2)$. E^5	$B_{sp}(E2) = 7.3 \times 10^{7}$. $A^{\frac{4}{3}}$. E^5
E3	$T(E3) = 5.698 \times 10^{2}$. $B(E3)$. E^7	$B_{sp}(E3) = 3.4 \times 10^{1}$. A^2 . E^7
E4	$T(E4) = 1.694 \times 10^{-4}$. $B(E4)$. E^9	$B_{sp}(E4) = 1.1 \times 10^{-5}$. $A^{\frac{8}{3}}$. E^9
M1	$T(M1) = 1.779 \times 10^{13}$. $B(M1)$. E^3	$B_{sp}(M1) = 5.6 \times 10^{13}$. E^3
M2	$T(M2) = 1.371 \times 10^{7}$. $B(M2)$. E^5	$B_{sp}(M2) = 3.5 \times 10^{7}$. $A^{\frac{2}{3}}$. E^5
M3	$T(M3) = 6.387 \times 10^{0}$. $B(M3)$. E^7	$B_{sp}(M3) = 1.6 \times 10^{1}$. $A^{\frac{4}{3}}$. E^7
M4	$T(M4) = 1.889 \times 10^{-6}$. $B(M4)$. E^9	$B_{sp}(M4) = 4.5 \times 10^{-6}$. A^2 . E^9

Table 2.1: Transition probabilities $T(\sigma L)$ expressed in terms of reduced transition probabilities $B(EL)$ ($\mathrm{e}^2\mathrm{fm}^{2L}$) and $B(EL)$ ($\mu_N^2\mathrm{fm}^{2L-2}$) and the Weisskopf estimates B_{sp} expressed in ($\mathrm{e}^2\mathrm{fm}^{2L}$) and ($\mu_N^2\mathrm{fm}^{2L-2}$) for electric and magnetic transitions, respectively. The transition energies are measured in MeV.

ratios $(g_K - g_R)$ such that

$$B(M1; I_i \to I_f) = \frac{3}{4\pi}(g_K - g_R)^2 |\langle I_i K_i 10 | I_f K_f \rangle|^2. \tag{2.18}$$

2.3.2 Internal conversion

Electronic wavefunctions may have finite amplitudes at the nuclear radius and the nucleus can de-excite by the emission of an atomic electrons [48, 49]. The electron is emitted with a kinetic energy T_e given by

$$T_e = (E_i - E_f) - B_e \tag{2.19}$$

where E_i and E_f are the excitation energies of the initial and final nuclear states and B_e is the binding energy of the electrons, which varies for different electronic orbitals. The vacancy created in this process is filled by an electron from a higher orbital and subsequently leads to the emission of an X-ray, which may be detected in coincidence with the conversion electrons. Internal conversion competes with γ-ray emission particularly well at low transition energies in heavy nuclides. The ratio between these two modes is expressed in terms of the total internal conversion coefficient, α, which is defined as

$$\alpha = \frac{\Gamma_e}{\Gamma_\gamma} = \frac{N_e}{N_\gamma}, \tag{2.20}$$

where Γ_e (Γ_γ) and N_e (N_γ) represent the width for electrons (γ rays) and number of electrons (γ rays) observed per excited nucleus. Therefore, the total transition width, Γ_t can be calculated from an accurate determination of α

$$\Gamma_t = \Gamma_\gamma + \Gamma_e \tag{2.21}$$

$$\Gamma_t = \Gamma_\gamma(1 + \alpha) \tag{2.22}$$

Internal conversion is sensitive to the transition multipolarity, which can be determined from intensity ratios of K, L, M, ... electron lines. Internal conversion is crucial for $0^+ \rightarrow 0^+$ transitions, which cannot decay by γ-ray emission.

2.4 Alpha Decay

Alpha decay is a two-body radioactive decay process that is observed mostly in the neutron-deficient nuclides above Z=50. In this decay mode the parent nucleus transforms into a daughter nucleus by the emission of a ^{4}He cluster (α particle) and the release of energy, Q, according to the expression

$${}^{A}_{Z}X_N \rightarrow {}^{A-4}_{Z-2}Y_{N-2} + \alpha + Q. \tag{2.23}$$

The net energy released in the α decay is called the Q-value, which corresponds to the total kinetic energy of the daughter nucleus and the α particle [50]. The Q-value can be deduced from the α-particle energy by considering energy and momentum conservation since

$$E_\alpha = \left(\frac{A-4}{A}\right) Q. \tag{2.24}$$

The description of the α-decay process requires a quantum mechanical model. The first successful model was introduced by Gamow [51] and by Gurney and Condon [52, 53]. In these early theories α decay was considered as a two-body problem where a preformed α particle moves within the potential of the daughter nucleus. The preformed α cluster moves in a spherical potential well $V(r)$ of depth V_0. In classical mechanics, the

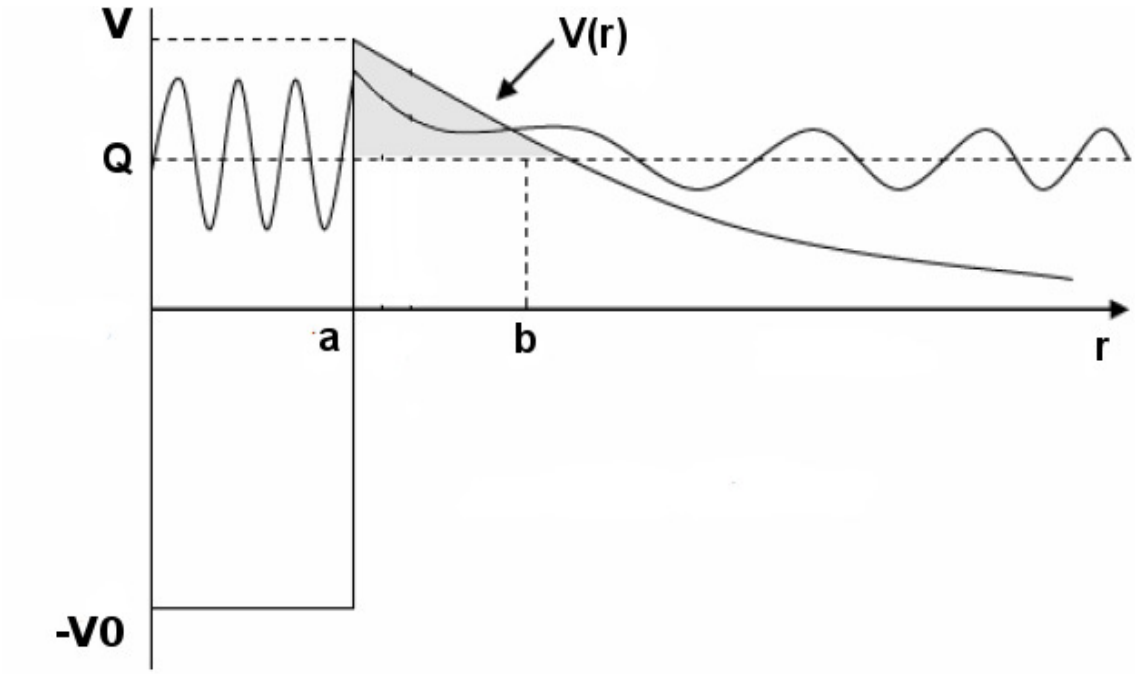

Figure 2.5: Schematic illustration of α decay as a quantum tunnelling process. a is the radius of the nucleus and b is the distance where the α particle has escaped.

α particle is bound by the potential and there is no way to penetrate the barrier. In the contrast, quantum mechanics allows a probability, P, of the α-particle tunnelling through the potential barrier as shown in Figure 2.5. The probability of tunnelling is given by

$$P = \mathrm{e}^{-2G}, \tag{2.25}$$

where G is the Gamow factor given by

$$G = \sqrt{\frac{2m}{\hbar^2}} \int_a^b \sqrt{V(r) - Q} dr, \tag{2.26}$$

where a and b are inner and outer turning points (see Fig. 2.5) and the other symbols have their usual meanings. Equation 2.25 can be rewritten in terms of the integrated Gamow factor as

$$P = \mathrm{e}^{-2\sqrt{\frac{2m}{\hbar^2 Q}}\frac{zZe^2}{4\pi\epsilon_0}\left[arccos\sqrt{x} - \sqrt{x(1-x)}\right]}, \tag{2.27}$$

where $x = a/b$, which are the parameters indicated in Fig. 2.5. The tunnelling probability is strongly dependent on the orbital angular momentum carried by α particle, the atomic

number of the daughter nucleus and the energy of the α particle. Rasmussen [54] expressed the probability as

$$P = \exp\left[-\int_a^b \frac{\sqrt{2\mu}}{h}\sqrt{V(r) + \frac{2Ze^2}{r} + \frac{\hbar^2}{2\mu r^2}l(l+1) - Q_\alpha}\right] dr. \tag{2.28}$$

Since the α decay energy is discrete and well defined it can be used for nuclide identification in highly selective tagging techniques.

2.5 Intruder states and shape coexistence

Shape coexistence is the phenomenon where nuclear configurations with very different deformations 'coexist' within a narrow range of excitation energies. Shape coexistence has been one of the most important phenomena for describing the origin of multiple deformed configurations in nuclei near the $Z = 82$ shell gap. The manifestation of shape coexistence is stated by Wood and Heyde [3] as the susceptibility of the nucleus to the competing tendencies of closed- and sub-shells that stabilise spherical shapes and the correlation energy obtained from the residual interactions between protons and neutrons, which makes the nucleus adopt a deformed shape.

In the context of the shell model, intruder states can be obtained by exciting a pair of nucleons across a shell gap as shown in the right side of Fig. 2.6. Assuming a closed proton shell configuration as found in the Pb isotopes, the energy of the lowest-lying excited 0^+ states can be expressed as [3]

$$E_{intruder} = 2(\varepsilon_{j\pi} - \varepsilon_{\hat{j}\pi}) + \Delta E^{\pi\pi}_{pair} + \Delta E^{\pi\upsilon}_{M} + \Delta E^{\pi\upsilon}_{Q}, \tag{2.29}$$

where the $2(\varepsilon_{j\pi} - \varepsilon_{\hat{j}\pi})$ term describes the unperturbed energy needed to create a $2p$-$2h$ configuration, which is defined by the proton single-particle energies. The $\Delta E^{\pi\pi}_{pair}$ term describes the pairing energy gain, the $\Delta E^{\pi\upsilon}_{M}$ term describes the monopole correction to the proton single-particle energy and the $\Delta E^{\pi\upsilon}_{Q}$ describes the proton-neutron quadrupole binding energy. The formula shows that the energy of the intruder states are dictated by the change in proton and neutron single-particle configurations. For example, the

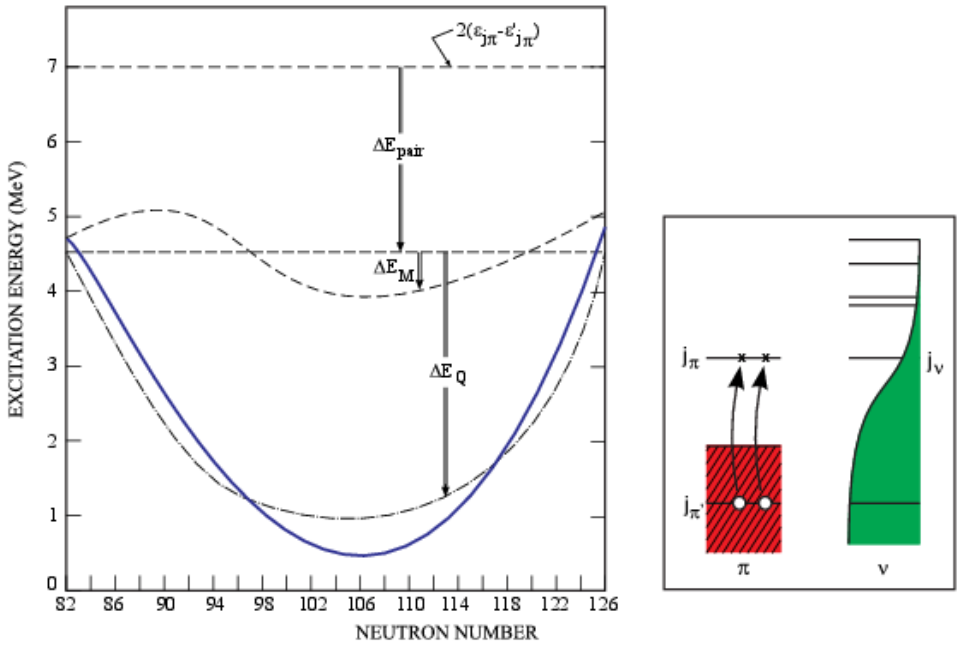

Figure 2.6: Contributions to the energy of the lowest lying 0_2^+ intruder state for heavy nuclei. The right hand side shows a schematic representation of the excitation process. This figure is reproduced from reference [3].

quadrupole interaction arises from the interactions between protons and neutron and has the greatest contribution in lowering the excitation energy of the intruder states when there is a maximum number of valence neutrons. In the case of Pb nuclei and their neighbours this corresponds to the neutron midshell at $N = 104$. The intruder parabolas in nuclei with $Z \sim 82$ tend to minimise near $N = 104$ but not always exactly highlighting the subtleties of the various interactions incorporated into equation 2.29.

The excitation of multiple pairs can happen, which modifies the pairing energy gains. The Au isotopes are known to have coexisting deformed configurations at low excitation energy of this type. For example, ^{187}Au has $\pi(3h)$, $\pi(1p-4h)$, $\pi(2p-5h)$ and $\pi(3p-6h)$ states with associated collective bands [55, 17]. It has been suggested that similar excitations should be seen in the other Au isotopes and consequently this work on ^{177}Au is a part of a wider programme of research that aims to determine the intruder systematics and elucidate the underlying interactions.

Chapter 3

Experimental Methodology

In order to obtain detailed information about the structure of exotic nuclei they must be created in an excited state and studied using spectroscopic techniques. This thesis probes the structure of the neutron-deficient nuclide ^{177}Au using the techniques of γ-ray spectroscopy in conjunction with selective tagging methods. This chapter discusses the reaction mechanism for synthesising ^{177}Au at moderately high spins and the detector systems and methods employed to identify electromagnetic and particle emissions. Specifically, the suite of spectrometer systems based at the Accelerator Laboratory of the University of Jyväskylä used to perform the experiment is presented.

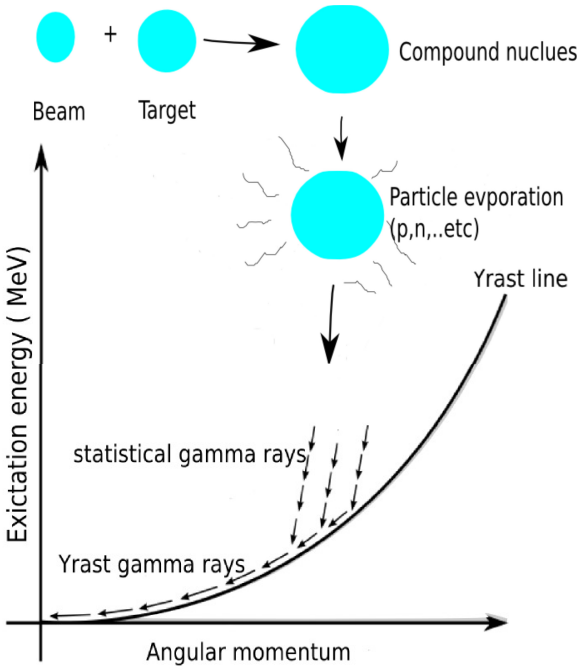

Figure 3.1: A schematic illustration of the stages of a fusion-evaporation reaction on an energy-angular momentum diagram.

3.1 Heavy Ion Fusion Evaporation Reactions

The fusion-evaporation reaction mechanism results from the collision of an accelerated ion beam with a static target. As a result of the collision the two nuclei are fused together to form a compound nucleus, which is highly excited in terms of energy and angular momentum [56]. Figure 3.1 shows a plot of the excitation energy versus angular momentum of the compound nucleus with a schematic view of the decay path. The compound nucleus initially loses excitation energy by evaporating particles, however, this stage of the reaction does not dissipate much angular momentum. In the neutron-deficient regions of the nuclear chart the protons are relatively loosely bound and exit channels involving protons are favoured. The reaction exit channel (or number of evaporated particles) depends on the energy and angular momentum that the compound nucleus obtains relative to the yrast line. The residual nuclei will shortly reach an excitation energy less than one nucleon separation energy from the yrast line after various combinations of protons, neutrons and α particles have been evaporated. This represents a threshold for particle emission and

γ-ray emission becomes the dominant decay mode. Initially, the residual nuclei decay by statistical γ rays that appear as a continuum due to the high density of the states from which they are emitted. These high-energy γ rays lose excitation energy but not much spin. When the evaporation residues achieve an excitation energy close to the yrast line, which represents the locus of maximum angular momentum values obtainable for a given excitation energy, γ rays are emitted in cascades from discrete states. The detection and analysis of these yrast cascades can provide an insight into the structure of the residual nucleus.

3.2 Experimental Apparatus

The experiment performed in this thesis used the JUROGAM γ-ray spectrometer in conjunction with the RITU gas-filled separator and the GREAT focal plane spectrometer. The coupling of these devices is shown in Fig. 3.2 and described in the following sections.

3.2.1 The JUROGAM γ-ray Spectrometer

The JUROGAM spectrometer [25] is designed to detect γ-ray transitions emitted at the target position. The spectrometer consists of 39 hyperpure Ge detectors of which 15 are phase I-type Compton-suppressed Ge detectors [57] and 24 are four-fold segmented clover detectors [58]. The detectors are positioned in four rings at angles 157.6° (5 phase I detectors), 133.57° (10 phase I detectors), 104.5° (12 clover detectors) and 75.5° (12 clover detectors) with respect to the beam direction. A major challenge in the development of germanium detector arrays was overcoming the poor peak-to-background ratio caused by incomplete energy detection in the HPGe detector caused by γ rays scattering out of the detector volume. This was solved by surrounding the detectors with the inorganic scintillator Bismuth Germanate (BGO) and using it as an anticoincidence detector [59, 60]. The peak-to-background ratio is increased by discarding any γ events that are detected in both the BGO and germanium detector.

The clover detector crystals are four-fold segmented. The γ rays above 200 keV are more likely to interact in the detector medium by the Compton scattering mechanism

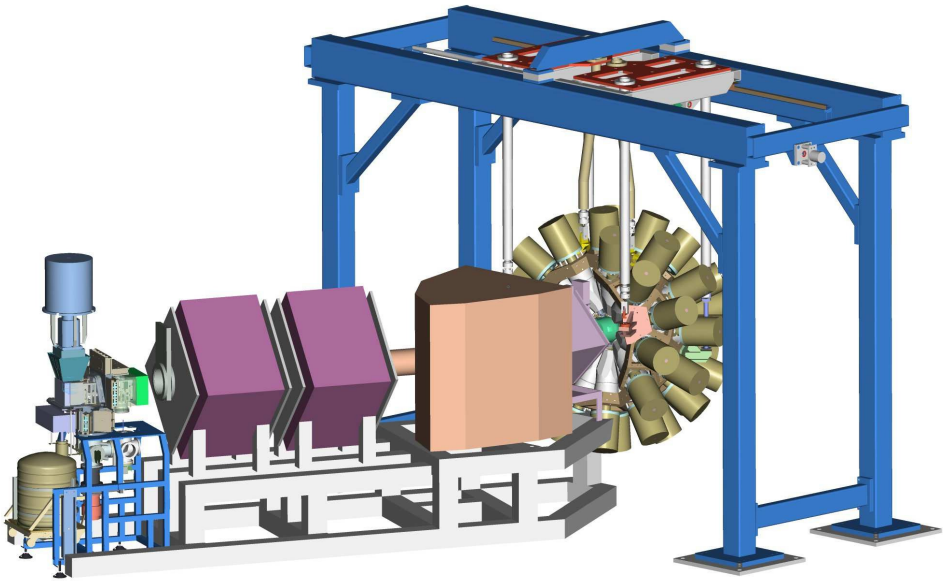

Figure 3.2: A schematic drawing of the coupling of the JUROGAM γ-ray spectrometer array (right), the RITU gas-filled separator (middle) and the GREAT focal-plane spectrometer (left) [61].

and can scatter from one crystal into a neighbouring one thereby depositing a fraction of its incident energy in each crystal. The segmentation of the clovers allows the user to reconstruct the incident γ-ray energy from Compton scattered events between neighbouring crystals. Figure 3.3 compares the spectra of the combined ^{241}Am, ^{152}Eu and ^{133}Ba calibration source with and without the add-back correction. The low-energy γ rays ($E_\gamma < 200$ keV) interact by photoelectric absorption and are barely affected by the addback procedure. However, Compton scattering is the dominant interaction process in the 200-1000 keV energy range so a significant enhancement of the peak-to-background ratio and the JUROGAM detection efficiency is achieved. The detection efficiency of JUROGAM with and without addback for single γ rays was determined to be 3.2% and 3.9% at 1.3 MeV, respectively.

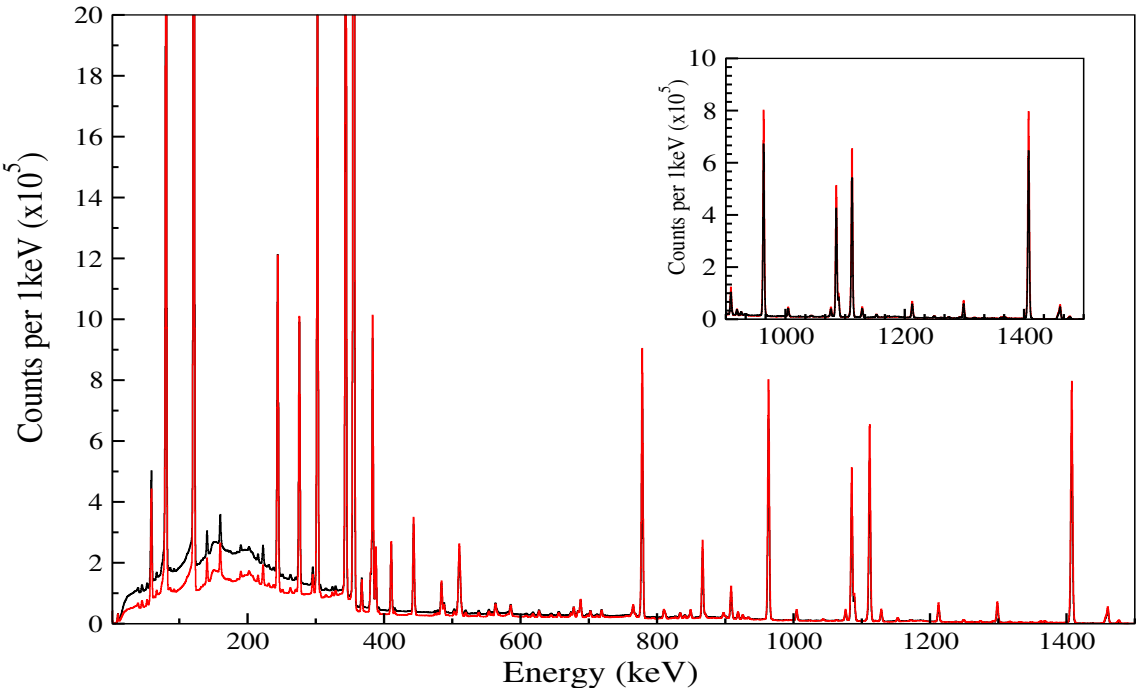

Figure 3.3: Spectra of the combined ^{241}Am, ^{152}Eu and ^{133}Ba calibration source with (red line) and without (black line) the add back correction. The corrected spectrum has a lower Compton background. The inset shows the enhancement in the peak areas of the high-energy transitions arising from the addback correction.

3.2.2 The Recoil Ion Transport Unit (RITU)

The Recoil Ion Transport Unit (RITU) [26, 27, 28, 29], shown in Fig. 3.4, is a gas-filled magnetic separator that transports evaporation residues (recoils) from the target position to the focal plane detection system. RITU is crucial for separating the unreacted beam, fission fragments and beam-like products from the fusion-evaporation residues using a combination of quadrupole (Q) and dipole (D) magnets in a QDQQ configuration. The initial quadrupole provides strong vertical focusing of the recoil cone to the acceptance of the dipole magnet. The dipole magnet is filled with dilute helium gas at pressure $0.5-1$ mbar with a maximum magnetic field strength 1.2 T. When the recoils pass through the dipole chamber they undergo charge exchange collisions with the gas molecules, which change the charge states of the recoiling fusion products. Consequently, the residues emerge from RITU in an average charge state. The recoiling nuclei follow a trajectory according to their average-charge state in the magnetic field of the dipole. Therefore, the magnetic rigidity $B\rho$, is key to the separation of evaporation products and scattered ion

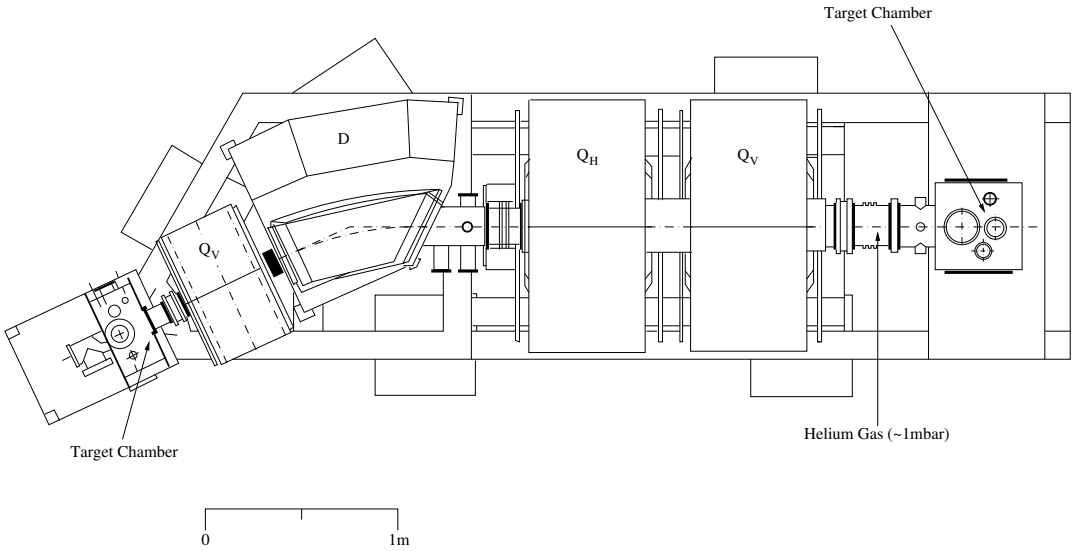

Figure 3.4: A plan view of the Recoil Ion Transport Unit gas-filled separator. This figure is reproduced from reference [62].

beams and can be determined as

$$B\rho = \frac{mv}{eq_{ave}}, \tag{3.1}$$

where m and q_{ave} are the mass and average-charge state of the particle, ρ is the radius of curvature of the trajectory and e is the charge of an electron. An approximation that uses the Thomas-Fermi model of the atom yields the average charge state

$$q_{ave} = \left(\frac{v}{v_0}\right) Z^{1/3}, \tag{3.2}$$

where v, v_0 and Z are the reaction product velocity, Bohr velocity and proton number, respectively. Equation 3.1 and Eq. 3.2 can be used to estimate the separation between the species

$$B\rho = 0.0227 \left(\frac{A}{Z}\right)^{1/3}, \tag{3.3}$$

where A is the mass number.

The other two remaining quadrupole magnets provide horizontal and vertical focusing of the recoiling reaction products to match the optical image size to the coverage of the GREAT implantation detector. The flight time from the target position to the focal plane detectors is approximately 1 μs.

3.2.3 The GREAT Focal Plane Spectrometer

The GREAT spectrometer is a focal-plane detection system placed at the focal plane of RITU and designed to detect recoil implantations and their subsequent radioactive and electromagnetic decays [30]. The GREAT spectrometer comprises five different detectors that are used to detect protons, α particles, β particles, γ rays, X-rays and conversion electrons. They are described here in the order that they are met travelling in the beam direction. A schematic picture of components of the GREAT spectrometer is shown in Fig. 3.5.

Multi-Wire Proportional Counter (MWPC)

A multi-wire proportional gas counter is situated 20 cm upstream from the implantation detector at the entrance of GREAT. It works as a transmission detector. The dimensions of the MWPC aperture are 131 mm horizontal $\times$ 50 mm vertical with a centred 1 mm wire. It has two mylar foils as entrance and exit windows, which separate the isobutane filling gas of the MWPC from the helium gas of RITU and the vacuum of the other GREAT detectors. The detection of the evaporation products can be achieved by ionization of the isobutane gas in the MWPC. The principle function of the MWPC is to distinguish between the transmitted recoiling nuclei and their subsequent decay events in the DSSD. This can be made by setting a two-dimensional gate on a matrix plotting energy loss in the MWPC versus time of flight between MWPC and DSSD.

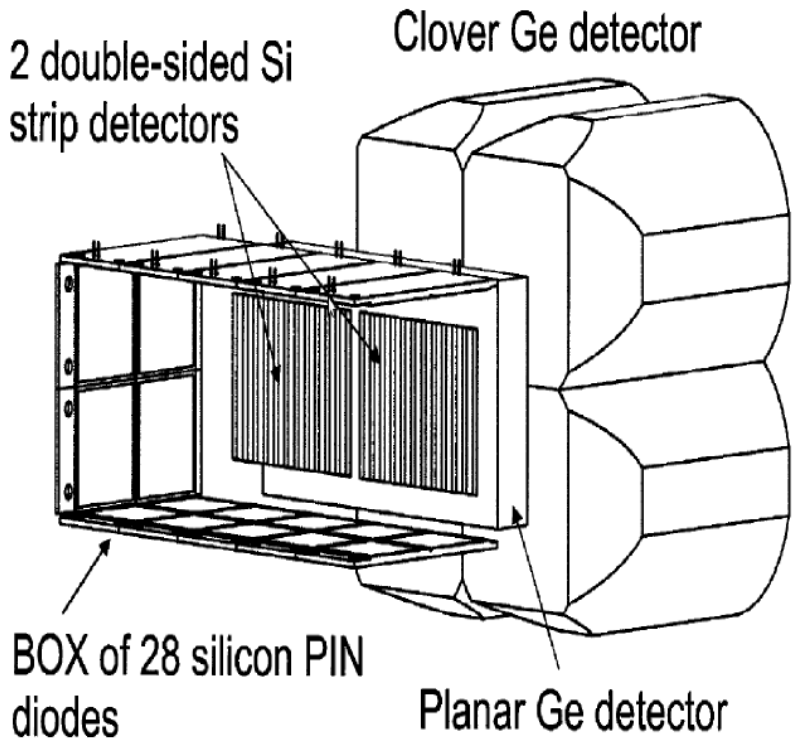

Figure 3.5: A schematic illustration of the GREAT focal plane. This figure is reproduced from reference [30].

Double-sided Silicon Strip Detectors (DSSDs)

The recoils are implanted into one of two adjacently mounted Double-sided-Silicon-Strip-Detectors (DSSDs). DSSDs are used to detect the recoil ions and their subsequent decay modes. Each detector has a dimension of 60 mm $\times$ 40 mm and a depth of 300 μm. A gap of 4 mm separates the left and right sides of the detectors. Each of the two sided-detectors has a 1 mm pitch both in both horizontal and vertical directions resulting in 4800 independent pixels. Such a high pixellation allows accurate spatial correlations to be performed.

Silicon PIN Diodes array

The silicon PIN diode detectors are arranged in a 'shoebox' arrangement orthogonal to the front face of the DSSDs, see Fig. 3.5. Each PIN diode has dimensions of 28 mm $\times$

28 mm with a thickness of 500 μm. The PIN diodes can be used to detect conversion electrons or α-particles that escape in the backward direction from the DSSDs.

Planar Germanium Strip Detector

The planar Ge detector is suitable for the measurement of low-energy γ rays, X-rays and high-energy β particles that escape from the DSSD. The planar detector is a double-sided position-sensitive detector that is placed directly behind the DSSDs at a distance of about 10 mm. The active area of this detector is 120 mm $\times$ 60 mm with a thickness of 15 mm with a 5 mm strip pitch on both faces yielding 228 pixels. The detector is evacuated behind a thin beryllium window in order to reduce the attenuation of photons.

Clover Detectors

There is a clover-type detector situated above the DSSD outside the vacuum chamber. The clover detector has a higher efficiency than the planar detector for γ-ray energies above 200 keV. The clover detector comprises four crystals of diameter of 70 mm before shaping and length 105 mm long. The crystals are tapered along the first 30 mm of their length. The clover is mostly used for the detection of γ rays depopulating long-lived isomeric states.

3.2.4 Total Data Read-out (TDR) Data Acquisition System

The total data readout (TDR) acquisition system is designed to eliminate the problem of common dead time from the composite detection system [31]. The TDR is a trigger-less data acquisition system allowing for timestamped events to be constructed in the software rather than by conventional hardware triggering. The TDR system enables the recording of signals from each individual detector component independently without any hardware triggering. The signals are read out by the electronics and processed as in Fig. 3.6. The signals are manipulated by a number of commercial amplifiers, constant-fraction-discriminators and analogue-to-digital converters. The signal is time stamped with reference to a system wide clock to a precision of 10 ns and then sent to the buffer.

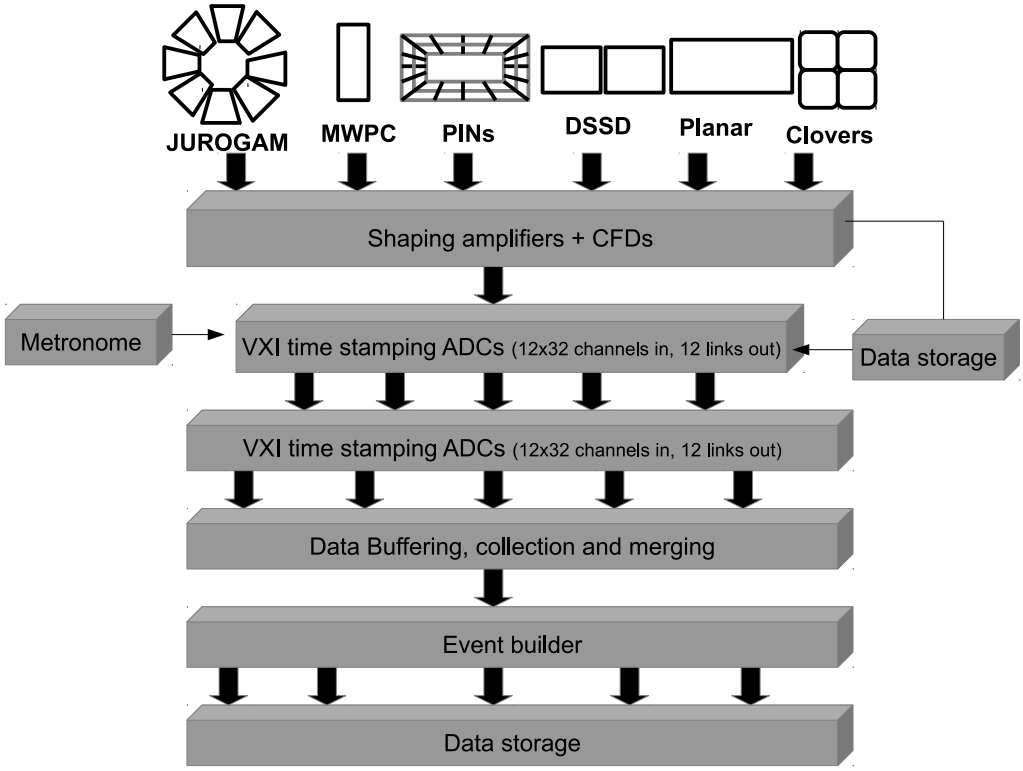

Figure 3.6: A schematic representation of the Total Data Readout (TDR) triggerless data acquisition system.

The event builder constructs the events for storage.

3.2.5 Analysis Software (GRAIN)

The analysis of the raw TDR data stream can be achieved using the GRAIN software package [63]. GRAIN is a Java-based software package, designed to manipulate and rebuild the events for online and offline analysis. GRAIN is developed and maintained by the Accelerator Laboratory of the University of Jyväskylä. A user with a Java sort code can perform correlations, create histograms and extract results from the data by visualising them through a graphical user interface, which can be run on any platform.

3.2.6 Detector Calibrations

Energy Calibrations

The detector systems provide only an electrical output signal, which is a current proportional to the incident energy. Without reference to a known energy these signals have no meaning. In order to perform high-resolution spectroscopy and data analysis an accurate energy calibration must be performed. This is done by converting the output electrical signal from the detectors to a calibrated energy using a standard radioactive source as a reference. The relationship between the ADC channels and the corresponding energy can be described by a quadratic fit function as

$$E = a + bx + cx^2. \tag{3.4}$$

Different sources are used to calibrate the various detector systems. Stationary calibrated ^{241}Am and ^{152}Eu-^{133}Ba sources of γ radiation are used for the energy calibration of the JUROGAM spectrometer array and the focal-plane Germanium detectors. These sources have γ-ray emissions spanning the broad energy range from 60 keV to 1408 keV.

Two calibrations can be performed for the implantation detectors; these are the internal and external calibration for initial online and detailed offline data analysis, respectively. For the external calibration, a triple-α source (^{239}Pu, ^{241}Am, ^{244}Cm) is used to make an external calibration of the DSSD detectors. However, in the external calibration some of the decay energy is lost in the dead layer on the DSSD surface. Thus an additional error is introduced in the calibration. An internal calibration can be performed by using the known α-decay energies of the implanted nuclei following a fusion-evaporation reaction.

Efficiency Calibration

An efficiency calibration is crucial for an accurate measure of the relative and absolute intensities of γ rays. To determine the γ-ray detection efficiency of the JUROGAM array, a stationary calibrated radioactive ^{152}Eu-^{133}Ba source was placed at the target position. In addition, a ^{241}Am source was also used to provide an additional data point in the

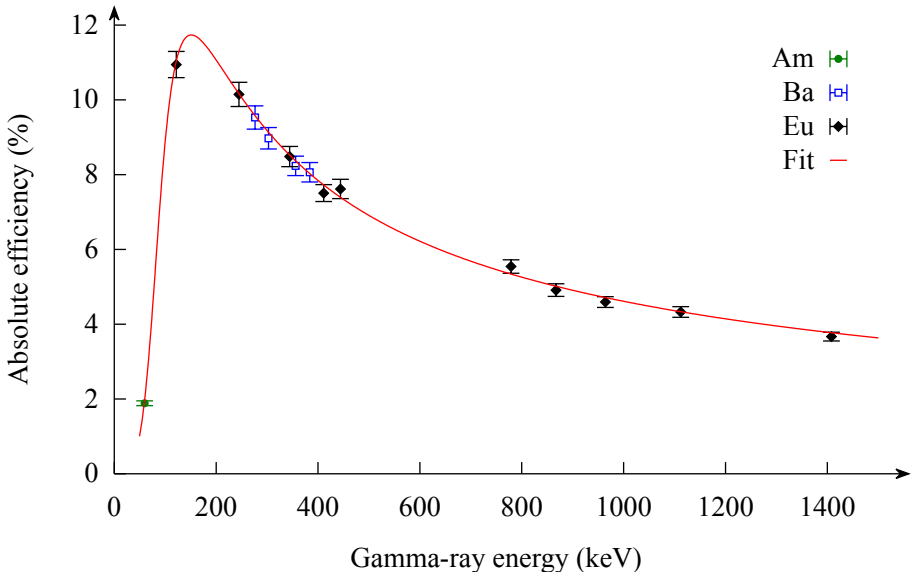

Figure 3.7: The efficiency curve for the JUROGAM γ-ray spectrometer array measured using the standard radioactive sources. This curve was extracted following the addback procedure.

low-energy region.

The detection efficiency of γ rays of a given energy is defined by the ratio of the number of γ rays detected to the total number of emitted γ rays. The absolute efficiency of the spectrometer array at a given energy was calculated using the area of the peak (N) at that energy, the activity of the standard sources (A), tabulated branching ratio of the transition (I) and the collection time (t) of the measurements with the relationship

$$\varepsilon_{abs} = \frac{N}{A\ I\ t}. \tag{3.5}$$

The γ-ray detection efficiency curve for JUROGAM was fitted to the measured data using the EFFIT program from the Radware software package [64] and is presented in Fig. 3.7. The fitted function is defined as

$$\varepsilon_{fit} = exp\left[\left(A + B\ log\left(\frac{x}{100}\right) + +C\ log\left(\frac{x}{100}\right)^2\right)^{-G} + \left(D + E\ log\left(\frac{x}{1000}\right) + F\ log\left(\frac{x}{1000}\right)^2\right)^{-G}\right]^{-1/G}. \tag{3.6}$$

The parameters for the fitted function in Fig. 3.7 are A= 2.60, B= 3.70, C=0.00, D=

1.53, E= −0.59, F= 0.00, G=3.12 and x is the γ-ray energy. Thus, the absolute efficiency of the JUROGAM spectrometer is measured to be 3.9% at 1.3 MeV.

Doppler-shift correction

The JUROGAM spectrometer array is constructed on a frame of four rings at forward and backward polar angles relative to the beam direction. The γ rays detected in JUROGAM are emitted from nuclei recoiling away from the target position and are Doppler shifted according to the relation

$$E \approx E_0 \left(1 + \frac{v}{c} \cos\theta\right), \tag{3.7}$$

where E is the Doppler-shifted energy, E_0 is the true transition energy, v/c is the velocity of the recoil as a fraction of the velocity of the light and θ is the detector angle relative to the beam direction. The relation is only approximate since the term including the Lorentz factor has been omitted. Figure 3.8(a) shows the Doppler shifted spectra obtained from the detectors at 75.5° and 157.6° relative to the beam direction. Figure 3.8(a) shows that the detectors at the forward angles (75.5°) are Doppler shifted to higher energies and backward angles (157.6°) are Doppler shifted to lower energies. Consequently, a Doppler correction is required to ensure that the γ-ray peaks detected in spectrometers at different polar angles are aligned. In order to correct the γ-ray energies, the v/c is measured by plotting a graph of the fractional energy shift $(E - E_0)/E_0$ of γ rays against the cosine of the detector angle from the ^{177}Au α-tagged spectra. The gradient yields the v/c value, which is this experiment was measured to be $v/c = 0.046$. Figure 3.8(b) demonstrates that the γ-ray spectra from both angles are located at the true energy of the transition following a Doppler correction.

3.3 Correlation Methods

The JUROGAM spectrometer array is designed to detect γ ray transitions emitted at the target position in order to perform in-beam γ-ray spectroscopy. Gamma-ray spectroscopy experiments probing the structure of highly neutron-deficient nuclei face several challenges.

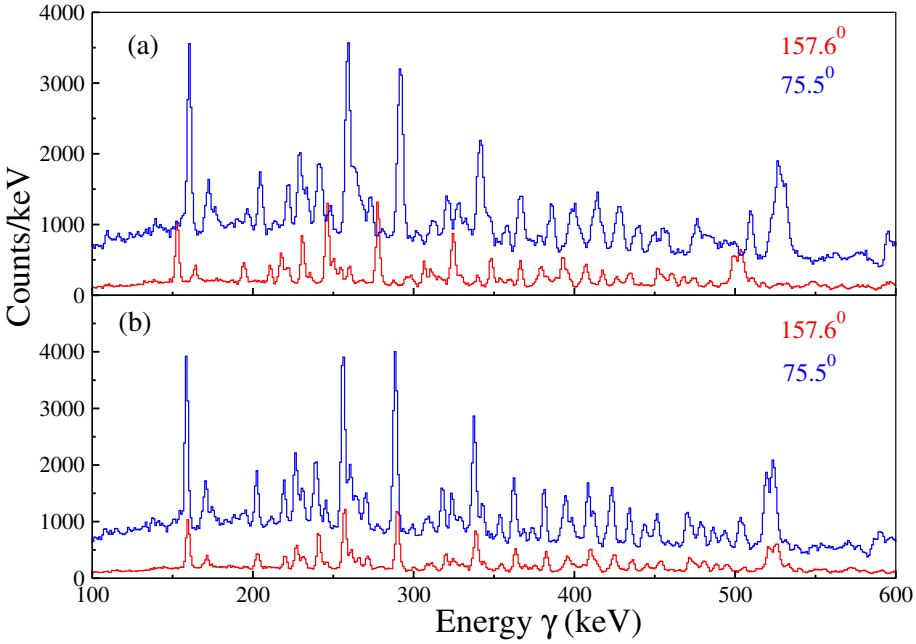

Figure 3.8: (a) Doppler-shifted γ-ray spectra obtained from the JUROGAM detectors at 75.5° and 157.6° relative to the beam direction. (b) The same spectra following a Doppler-shift correction.

The nuclei of interest are often produced at low fractions of the total fusion cross sections relative to the total reaction cross section. Furthermore large γ-ray backgrounds can originate from the nuclei produced in stronger reaction channels including fission following fusion evaporation. The Coulomb excitation of the beam and target nuclei can also add to the background. The reduction of these large γ-ray backgrounds can be achieved by coupling the JUROGAM spectrometer array to the RITU gas-filled separator and the GREAT focal-plane spectrometer to make recoil-decay tagged γ correlations. The recoil-decay tagging technique is a highly effective method for identifying nuclei of interest by spatial and temporal correlations of their characteristic radioactive decays [22, 23, 24].

3.3.1 Recoil Identification

It is important to be able to distinguish between recoil and scattered beam implantations in the DSSD. The GREAT MWPC has a central role in making this distinction possible. When the residual species are transported from the target position to the DSSDs via RITU they pass through the MWPC and generate signals in it. Energy loss and time-of-flight

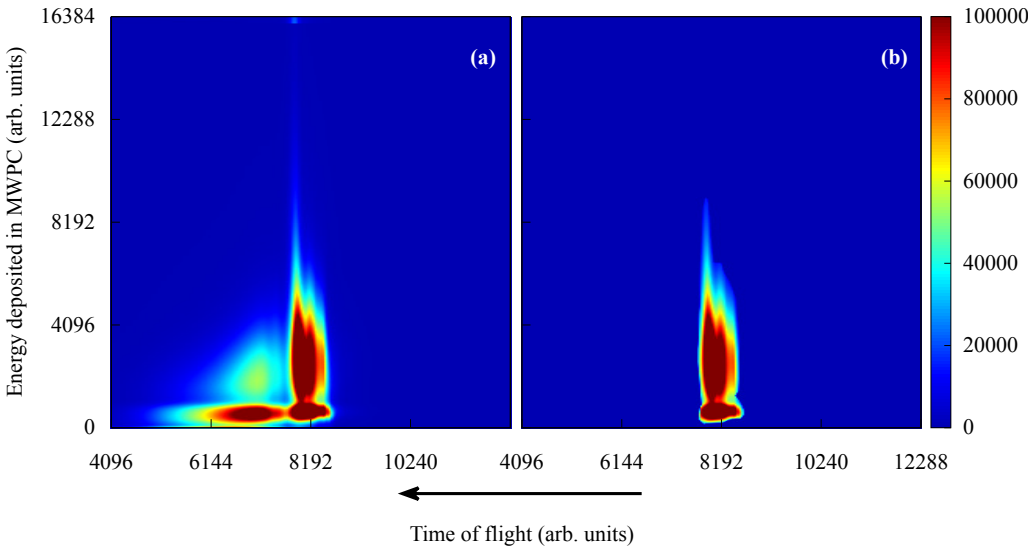

Figure 3.9: (a) A matrix plotting ion time-of-flight deduced from the time differences between the GREAT MWPC and DSSDs versus the energy deposited in MWPC (b) Recoiling fusion evaporation residues selected by a two-dimensional gate.

(in conjunction with the DSSD) ensure discrimination between fusion evaporation residues and scattered beam. In general, the recoils are the higher-Z ions and deposit more energy and produce more ionisation in MWPC. The velocity of the heavier recoils is much less than the velocity of the lighter unreacted beam and consequently the difference between the time signals in the MWPC and DSSD is longer for the recoils. The recoils are identified by setting a two-dimensional gate on an matrix of energy deposited in the MWPC against the time of flight of the ions measured between MWPC and DSSD as shown in Fig. 3.9.

3.4 γ-Recoil Delayed Coincidences

Prior to performing recoil-decay tagging correlations it is important to associate γ rays detected at the target position with recoil implantations that are detected in delayed coincidence at the focal plane. Gamma ray - recoil correlations that allow for the flight time of residues through the RITU separator are obtained by plotting a matrix of time-of-flight of recoils between the GREAT MWPC and DSSD against the time difference for detecting a γ ray in JUROGAM time and a recoil implantation at the GREAT DSSD. Figure 3.10(a) shows a plan view of this matrix. Figure 3.10(b) shows a further selection

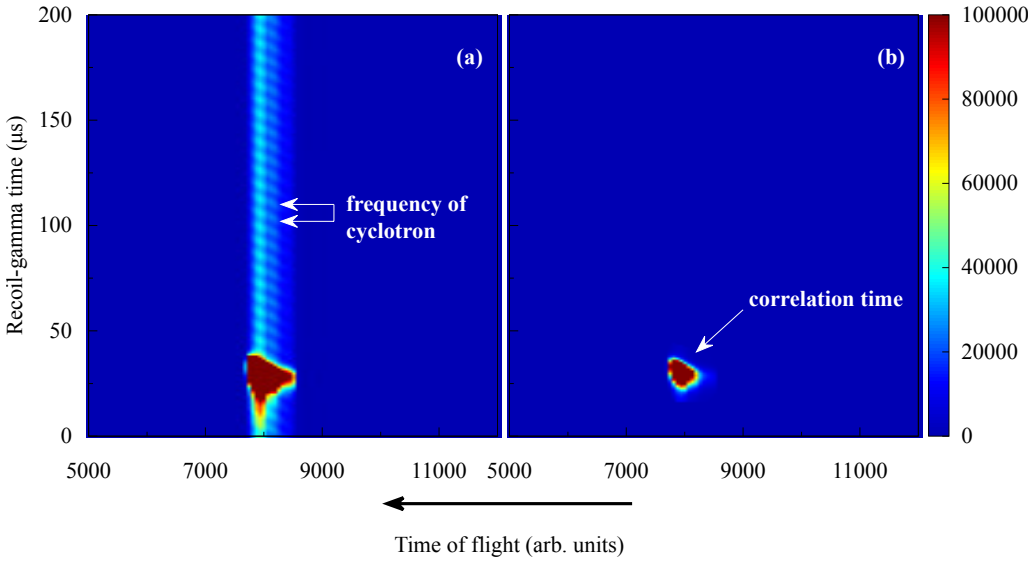

Figure 3.10: (a) A two-dimensional matrix of recoil-γ time difference versus the time of flight of ions between the GREAT MWPC and DSSD. (b) Subset of events passing a gate on part of the matrix.

by making another two-dimensional gate around a subset of γ-recoil delayed coincidences that pass the two-dimensional gate shown in Fig. 3.9(b).

3.4.1 The Recoil Decay Tagging (RDT) Technique

The recoil-decay tagging technique can be used for in-beam studies of excited states in heavy neutron-deficient nuclei that would be inaccessible with conventional in-beam methods. The method relies on correlating γ rays detected at the target position with recoil implantations and their subsequent characteristic radioactive decays in a detector system at the focal plane of a recoil separator. The coupling of the JUROGAM and GREAT spectrometers with the RITU recoil separator and used in conjunction with the TDR timestamping data acquisition system has allowed the neutron-deficient nuclide ^{177}Au to be investigated with recoil-decay tagging.

The high degree of pixellation in the DSSDs allows precise spatial correlations between recoil implantations and their subsequent α decays. The recoil-decay correlations are performed using the GRAIN software package. The GRAIN sort code uses a three-dimensional array called the *tagger*, which uses the x and y DSSD strips to define the pixels and stacks recoils and subsequent recoils or decays in the z direction. The principle

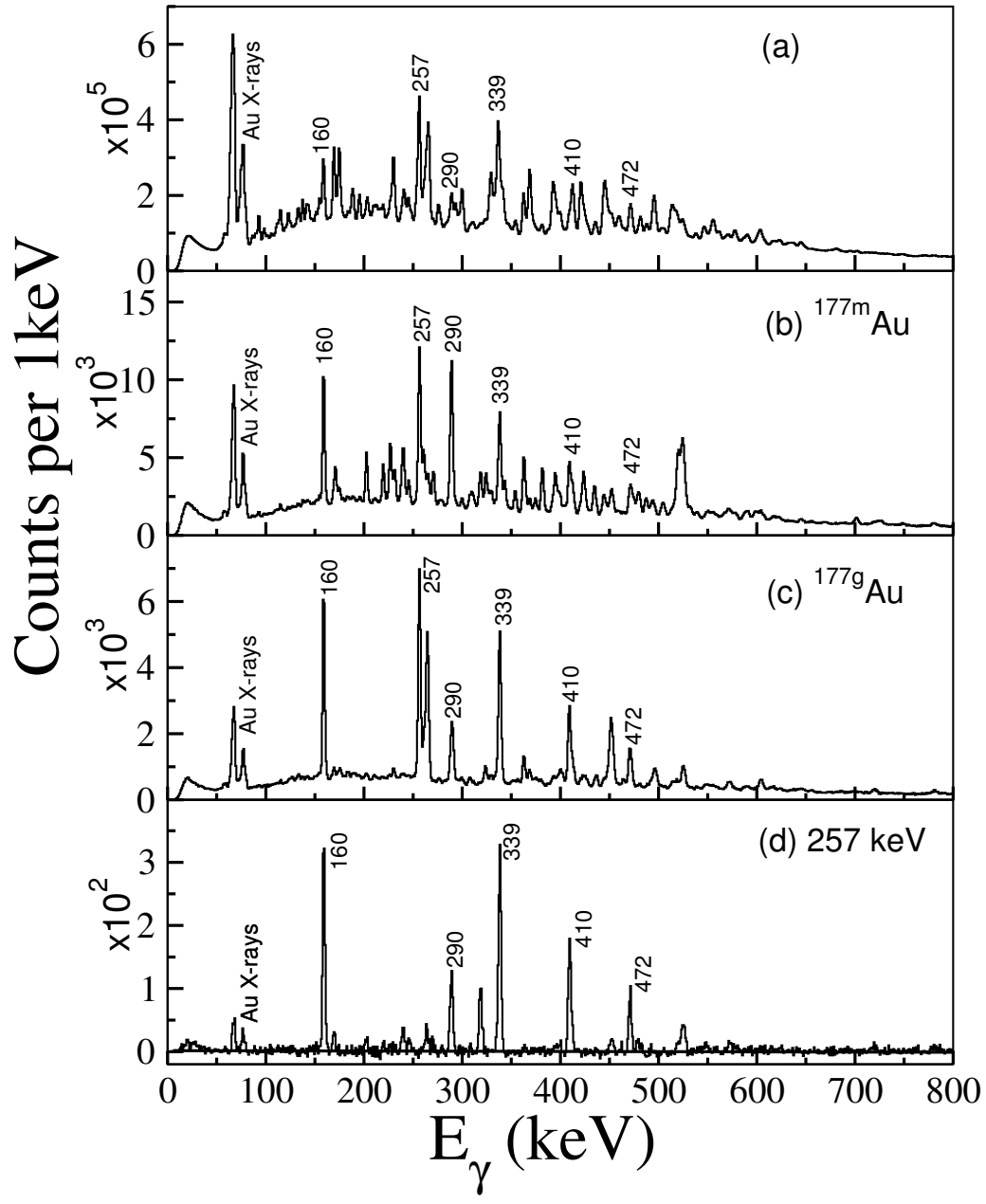

Figure 3.11: (a) Gamma rays in delayed coincidence with a recoil implantation at the GREAT DSSD. (b) Gamma rays selected by recoils that are followed by the characteristic α decays of the $11/2^-$ isomer in ^{177}Au within the same DSSD pixel. (c) Gamma rays selected by recoils that are followed by the characteristic ground-state α decays of ^{177}Au within the same DSSD pixel.(d) Gamma rays in coincidence with the 257 keV transition in ^{177}Au generated from a $\gamma-\gamma$ matrix tagged by an $\alpha(^{177m}$Au) decay. The 257 keV transition was assigned to the $i_{13/2}$ intruder band in ^{177}Au in the earlier work by Kondev *et al.* [20]. The correlation time was limited to 3900 ms, which corresponds to approximately three half-lives.

work of the tagger array is to detect and store the events for a pre-determined time. For example, if a recoil implantation is detected it is put in the first array element in the tagger. The subsequent array elements can be occupied by either a radioactive decay or another recoil. Thus specific nuclides can be identified by correlating recoils and their decays within a defined correlation time, which is usually set at 2 - 4 half-lives depending on the recoil implantation rate.

Figure 3.11 shows the selectivity of the recoil-decay tagging technique. Figure 3.11(a) shows all γ rays in delayed coincidence with a recoil implantation at the GREAT DSSD. Figure 3.11(b) and Fig. 3.11(c) show the γ rays selected by recoils followed by characteristic α decays of ^{177}Au within the same DSSD pixel. The correlation time was limited to 3900 ms, which corresponds to approximately 3 half-lives.

Recoil-decay tagged $\gamma-\gamma$ coincidence matrices can be used to establish the relationships between γ rays populated in the de-excitation process. In this work, such matrices were sorted using the GRAIN software package [63] and exported for analysis in the Radware software package [64]. Figure 3.11(d) highlights a typical γ-ray coincidence spectrum generated from a $\gamma - \gamma$ matrix tagged by an $\alpha(^{177}\text{Au})$ decay.

3.5 Angular Correlations

A γ-ray transition has a multipolarity that results in a specific angular intensity distribution. Experimental measurements of the angular correlations between coincident γ rays can be used to determine the relative spins of excited nuclear states and in some cases provide information on the multipole mixing ratio, δ [65, 48]. The JUROGAM array has detectors positioned at different angles relative to the beam direction and allows the measurement of the directional correlation of oriented states.

The angular correlation analysis requires the detection of two γ rays emitted sequentially within the same cascade where the orientation axis is defined by the initial γ ray detected in the sequence. The angular correlation measurement requires the construction of asymmetric $E_{\gamma 1}(\theta_1) - E_{\gamma 2}(\theta_2)$ matrices where θ_1 and θ_2 correspond to the detector angles at extreme (157.64°) and perpendicular (75.5° and 104.5°) angles in the array.

The directional correlation of orientated states (DCO) ratio [66] is determined from γ-ray intensities extracted from these matrices using the formula

$$R_{DCO} = \frac{W(\theta_1, \theta_2, \Delta\phi)}{W(\theta_2, \theta_1, \Delta\phi)} \equiv \frac{I_{\gamma\gamma}(\theta_1, \theta_2[gate], \Delta\phi)}{I_{\gamma\gamma}(\theta_2, \theta_1[gate], \Delta\phi)}, \tag{3.8}$$

where θ and ϕ are the polar and azimuthal angles, respectively. The dependence on the azimuthal angle ϕ can be neglected since the measurement was taken over all $\Delta\phi$. In this work the α-tagged spectra were used to perform such analysis.

Chapter 4

Shape Coexistence in the Proton-Unbound Nucleus, ^{177}Au

Excited states of the neutron-deficient nuclide ^{177}Au have been populated following the ^{92}Mo(^{88}Sr,2pn) reaction in an experiment performed at the University of Jyväskylä Accelerator Laboratory. Gamma rays detected in the JUROGAM spectrometer were correlated with the characteristic α decays of ^{177}Au detected following a recoil implantation in the GREAT spectrometer. A large number of transitions (~ 60 γ rays) have been assigned unambiguously to ^{177}Au and ordered into four collective band structures and single-particle excitations. These new rotational bands are interpreted in terms of coexisting proton hole and proton intruder configurations near the $Z = 82$ shell closure.

4.1 Motivation and previous work

Shape coexistence refers to the phenomenon where two or more nuclear shapes that are based on different underlying configurations lie at very similar (usually low) excitation energies. The phenomenon arises from the interplay between the stabilising effect of closed shells and the correlated residual interactions that occur between nucleons. Shell gaps promote relatively stable spherical shapes where the rearrangement of nucleons to produce deformed excited configurations results in a cost in excitation energy. The residual interactions between nucleons, however, can produce a correlation energy gain, which is dependent on the number of valence nucleons and tends to force the nucleus to adopt deformed shapes. The structure of coexisting configurations may be interpreted in terms of shell model or mean-field theoretical approaches. An intuitive interpretation of shape coexistence arises from the consideration of specific configurations based on multiple particle-hole (mp-nh) excitations across closed shells, which provide the basis for low-lying collective bands.

One of the most extensively characterised regions of low-energy shape coexistence is found in the vicinity of the $Z = 82$ proton shell gap and the neutron midshell at $N = 104$ [67, 68, 69]. The first instance of shape coexistence in this mass region was observed in the Hg isotopes from optical hyperfine spectroscopic measurements [9]. These experiments revealed a large isotope shift between ^{185}Hg and ^{187}Hg [9], which provided a model independent indication of an increase in the mean-square charge radius between the ground states of these isotopes. Subsequent in-beam spectroscopy experiments led to the interpretation of the odd-even staggering of isotope shifts in the Hg isotopes as arising from deformed bands based on excited 0^+ states. Shape coexistence has been established extensively in other even-Z nuclei below the proton shell gap at $Z = 82$ including Pb [10, 11], Hg [9, 12], Pt [13] and Os [70, 14] isotopes.

There are gaps in our knowledge of shape coexistence in odd-A nuclei such as Tl ($Z = 81$) and Au ($Z = 79$). This arises because odd-A nuclei can exhibit far more complicated excitation spectra than their doubly even neighbours. Moreover, these isotopes are mostly studied at low cross sections following fusion evaporation reactions, which can also produce large γ-ray / decay backgrounds arising from other reaction products including fission.

There are suggestions that shape coexistence should occur at low spin in the neutron-deficient Au isotopes from in-beam and decay spectroscopy measurements [71, 18, 55, 17, 21, 16] where rotational bands based on proton intruder and hole configurations have been observed based on excitations from the $s_{1/2}$, $d_{3/2}$ and $h_{11/2}$ orbitals below the $Z = 82$ shell gap to the $h_{9/2}$, $f_{7/2}$ and $i_{13/2}$ orbitals above it. This work reports the observation of several new coexisting band structures in the neutron-deficient nucleus ^{177}Au.

The isotope ^{177}Au was first observed by Siivola who identified the 6115 keV α decay from the $11/2^-$ state at the Lawrence Radiation Laboratory at Berkeley in 1968 [72]. The first insight into the higher-spin excited states came from an in-beam γ-ray spectroscopy experiment using GAMMASPHERE in conjunction with the Fragment Mass Analyser [20]. In this experiment Kondev *et al.* used the recoil decay tagging technique to unambiguously identify the yrast band in ^{177}Au through correlations with the distinct $\alpha(^{177}\text{Au})$ decays. The yrast band was assigned to be a prolate band built upon the intruder $1/2^+[660](i_{13/2})$ proton orbital that decays through a fragmented decay path to lower spin states. The level scheme established by Kondev *et al* is shown in Figure 4.1. The excitation energy of the $11/2^-$ state has subsequently been established to be 189(16) keV above the $1/2^+$ state in the radioactive decay study of ^{181m}Tl by Andreyev *et al.* performed at the SHIP separator in GSI [73].

The lowest $9/2^-$ state of ^{177}Au has been tentatively assigned as the $h_{9/2}$ proton-intruder configuration based on a single-proton excitation across the $Z = 82$ shell gap into the $9/2^-[505]$ Nilsson configuration. This assignment is made on the basis of similarities identified by Venhart *et al.* in the structure of ^{179}Au elucidated in the α decay of ^{183}Tl [74]. The emerging picture of these bands in the heavier odd-Au isotopes show a decoupling of the $h_{9/2}$ from axially symmetric Pt cores. This work reports the first observation of the collective bands built on the $9/2^-$ ($h_{9/2}$) and $7/2^-$ ($f_{7/2}$) intruder band heads. Proton-hole configurations in the $s_{1/2}$, $d_{3/2}$ and $h_{11/2}$ orbitals that couple to the underlying even-even Hg cores are known to form the basis of coexisting states at low energy in this mass region [11]. Such proton-hole configuration are anticipated to play a major role in odd-A Au isotopes. For example, the $11/2^-$ states that lie above the low-lying α-decaying $11/2^-$

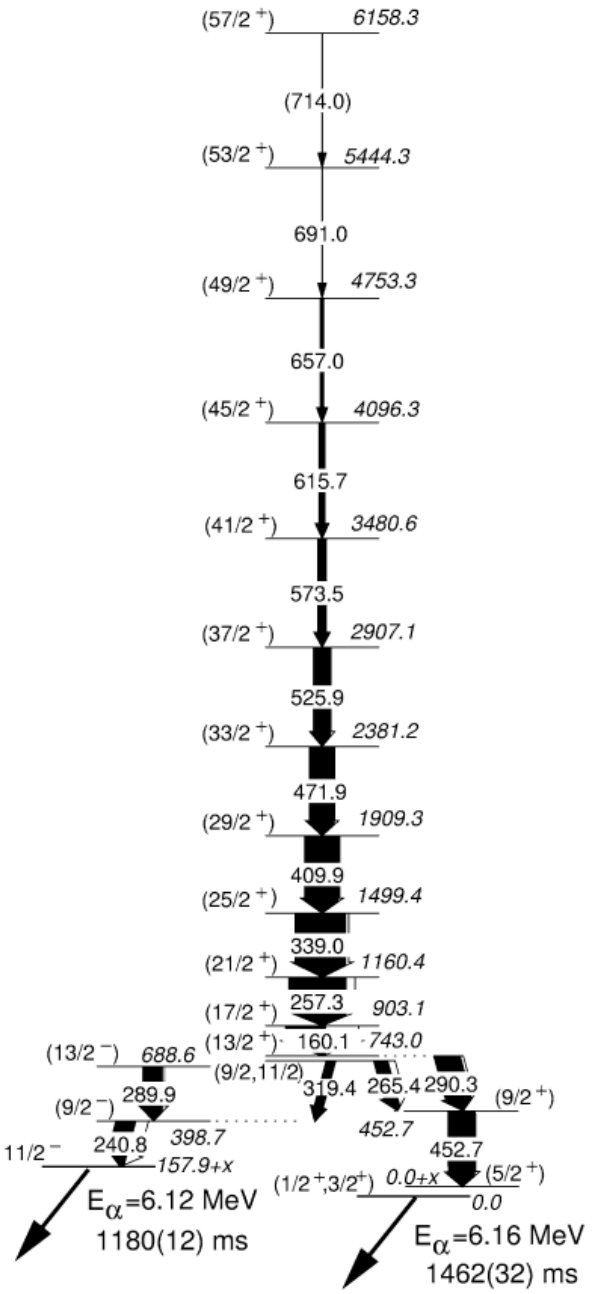

Figure 4.1: Previous level scheme for ^{177}Au deduced by Kondev *et al.* The transition energies are given in keV and their relative intensities are proportional to the widths of the arrows.

isomer are interpreted as predominantly $h_{11/2}$ holes coupled to the $2p-4h$ deformed even-even Hg cores [55, 17]. The corresponding $11/2^-$ states in the odd-A Au isotopes are expected to be the $11/2^-[505]$ Nilsson structure coupled to the excitations of the Hg core. A good experimental signature of this configuration would be the presence of a strongly coupled band. Such evidence is currently sparse since the level schemes are either incomplete (e.g. ^{185}Au) [75] or not linked into the level scheme at a firm excitation energy (e.g. ^{181}Au) [76]. This work provides the first observation of a strongly coupled ($h^{-1}_{11/2}\otimes$ Hg) band in the neutron-deficient Au isotopes where the decay from the excited $11/2^-$ band head is elucidated.

4.2 The Experiment

The fusion evaporation reaction ^{92}Mo(^{88}Sr,2pn) was used to populate the excited states of ^{177}Au. The K130 cyclotron of the Accelerator Laboratory of the University of Jyväskylä accelerated the ^{88}Sr ions to a bombarding energy of 378 MeV. The beam was incident on a ^{92}Mo target of nominal thickness 600 μg/cm^2. Gamma rays emitted at the target position were detected in the JUROGAM Ge-spectrometer array [25]. Reaction products were transported to the focal plane of the RITU gas-filled separator [27, 28, 29] where they were implanted into the DSSDs of the GREAT spectrometer [30]. Fusion products were separated from unreacted beam using energy loss in the GREAT multiwire proportional counter and (with the DSSDs) time of flight measurements. All detector signals were processed independently in the GREAT total data readout (TDR) data acquisition system. Each individual detector signal was timestamped to a precision of 10 ns so that temporal and spatial correlations to be performed. The data were sorted and analysed using the GRAIN [63] and Radware [64] software packages.

4.3 Results

4.3.1 The α-decaying states in ^{177}Au

Previous decay spectroscopy measurements of ^{177}Au have revealed that the ground state and a low-lying isomeric state decay by the emission of an α particle. Studies of the ground-state α decay from ^{181}Tl have limited the ground-state spin in ^{177}Au to be $1/2^+$ and placed the isomer, which is assigned to be the $11/2^-$ configuration, at an excitation energy of 189(16) keV above the ground state [73]. More recent laser spectroscopy measurements of ^{177}Au have confirmed the ground-state and isomer spins to be $1/2^+$ and $11/2^-$, respectively [77].

The α-decay half-lives of the ground and isomeric states have been measured in this work. Figure 4.2(a) shows the spectrum of α particles that are observed up to 3900 ms after a recoil implantation in same DSSD pixel of the GREAT spectrometer. The centroids of the ^{177}Au α decays are distinct however the peak shapes overlap, which could influence the measured half-lives. To mitigate this effect γ rays that are detected at the target position and feed each of the α-decaying states exclusively have been used to suppress the background arising from correlations with the overlapping decay. Figures 4.2(b) and (c) show α decays that are correlated with the 265 keV and 203 keV γ rays that feed the ground state and the isomer, respectively. The γ rays are not unique to a specific nucleus and sit on a background of Compton scattered γ rays, which results in a large background of other α decays. However, the relative peak areas of the ^{177}Au decays in Figures 4.2(b) and (c) indicate that some level of suppression is apparent and the data can be biased in favour of a particular α-decay peak.

Figure 4.3 shows the decay curves extracted from the time differences between the detection of a γ-biased recoil and its subsequent α decay within the same DSSD pixel. The decay curve for the α decay from the ground state has been fitted with an exponential function with additional background corrections to allow for multiple recoil implantations in the same pixel within the correlation time such that

$$(A_0 e^{-\lambda_A t} + c) f(t), \tag{4.1}$$

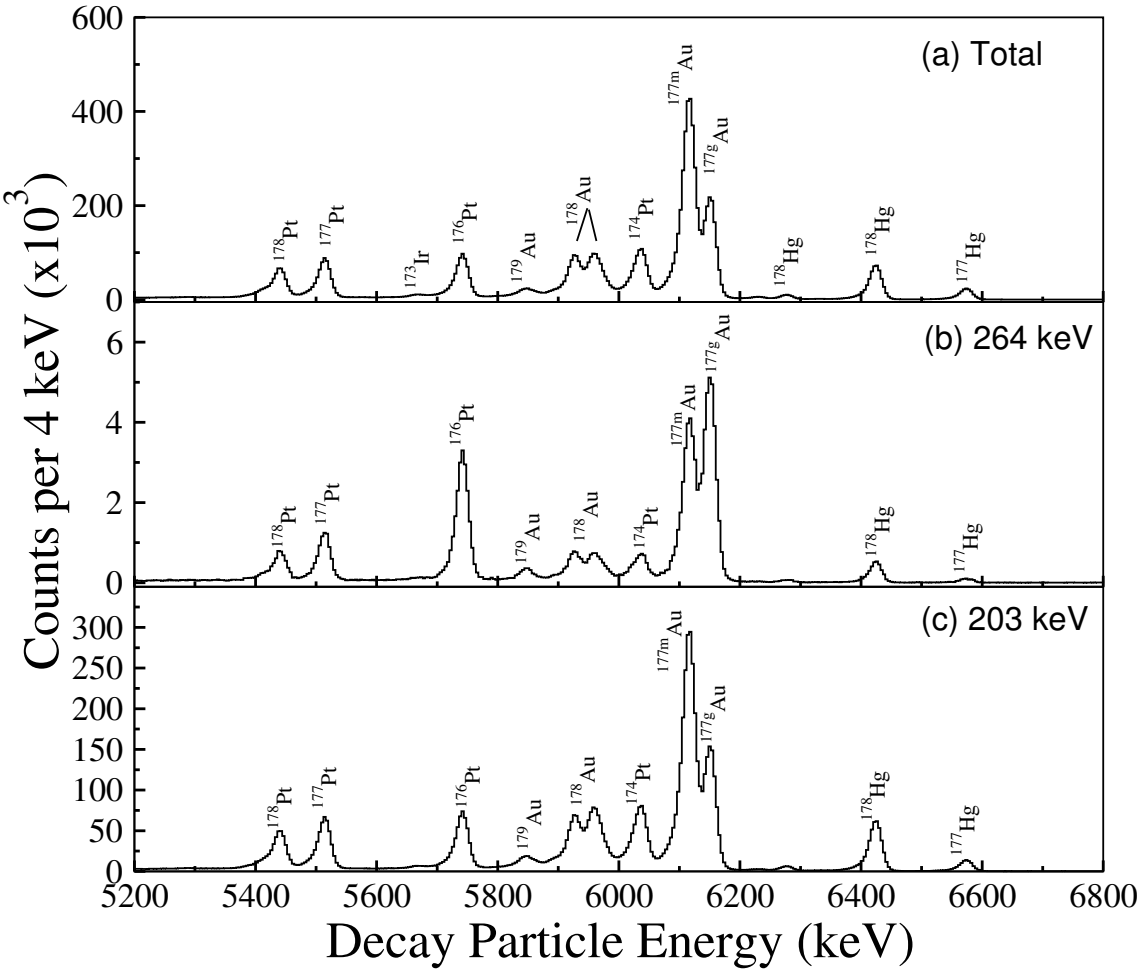

Figure 4.2: (a) Decay particle energy spectrum of all decays occurring within 3900 ms of an ion implantation into the same DSSD pixel. (b) Spectrum with the same recoil-decay correlation with the additional requirement of a coincidence with the 265 keV γ-ray transition that feeds the $3/2^+$ state at 25 keV above the ground state (see Fig. 4.7). (c) Spectrum with the same recoil-decay correlation with the additional requirement of a coincidence with the 203 keV γ-ray transition, which is placed in the strongly coupled band (Band 4 in Fig. 4.8).

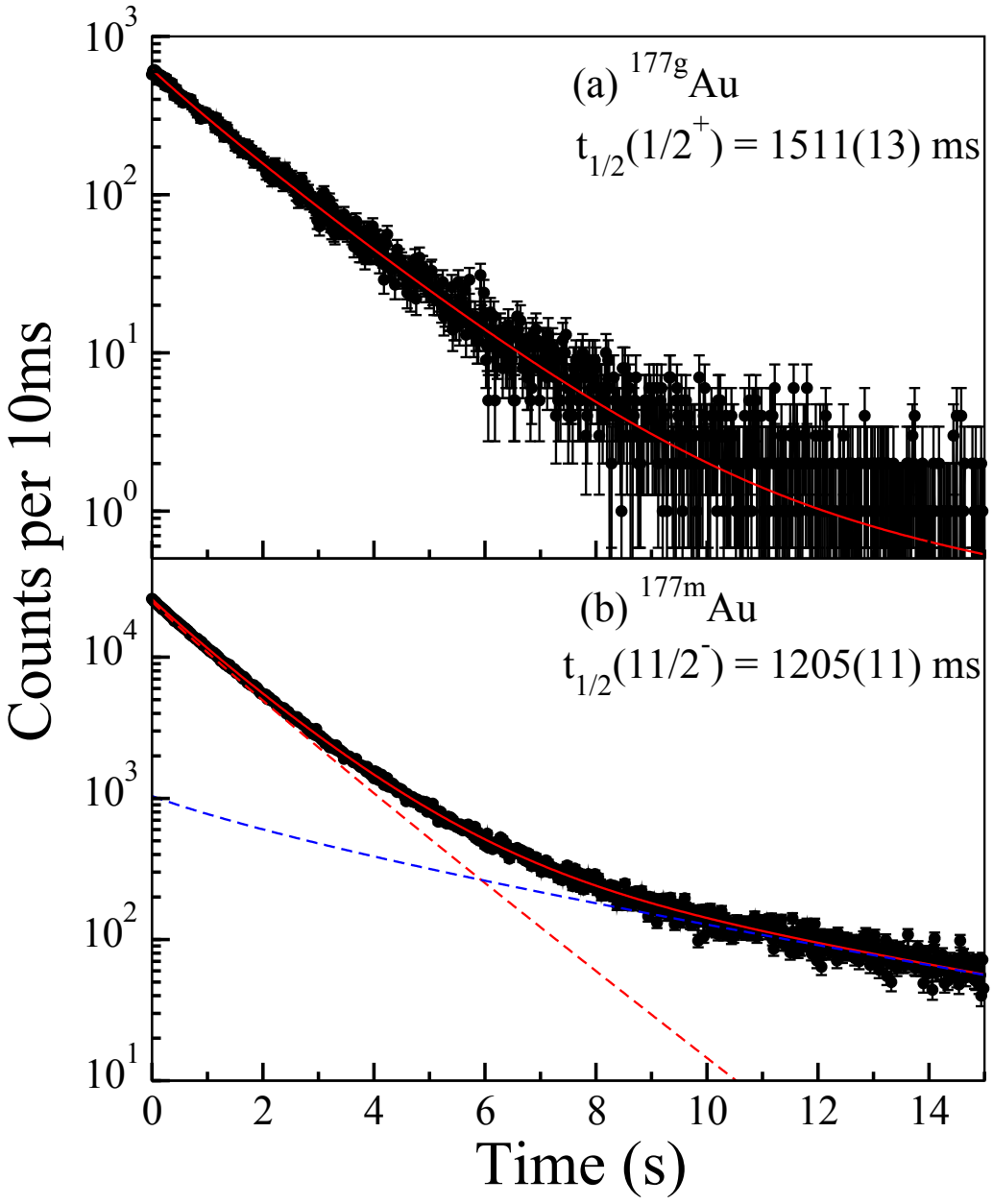

Figure 4.3: Time differences between ion implantations and the characteristic α decays of ^{177}Au within the same DSSD pixel in the GREAT spectrometer. (a) The decay curve corresponding to ions that are followed by the 6153 keV α decay originating from the ground state that are also correlated with the 265 keV γ-ray transition detected in the JUROGAM spectrometer. (b) The decay curve corresponding to ions that are followed by the 6118 keV α decay originating from the $11/2^-$ isomer that are also correlated with the 203 keV γ-ray transition detected in the JUROGAM spectrometer. The fitted decay curves and their components are shown as solid and dashed lines, respectively. The red dashed line corresponds to the decay of the $11/2^-$ α-decaying isomer in ^{177}Au whereas the blue dashed line accounts for overlapping α decays and the random recoil implantations.

where A_0 is the initial number of nucleus A, λ_A is the decay constant, t is the time, c is a term that accounts for a flat background and $f(t)$ corrects for multiple implantations within the same DSSD pixel. The function $f(t)$ is deduced from the time difference between successive recoil implantations that are followed by an α particle within the same DSSD pixel and was obtained by fitting a sum of four exponential functions, which is normalised such that

$$f(t) = \sum_{i=1}^{4} a_i e^{-b_i t} \tag{4.2}$$

where a_i is the amplitude and b_i is the decay constant for the i^{th} term. The recoil - α-decay time difference spectra and fitted decay curves for the ground state are shown in Fig. 4.3(a). The α-decay half-life from the ground state is measured to be $t_{1/2} = 1511(13)$ ms.

The fitting function for the decay curve for the ground-state α-emission is relatively simple since the overlap with the lower energy $11/2^-$ α decay can be eliminated by a careful α-particle energy selection. The decay curve of the α emission from the $11/2^-$ isomer will have some unavoidable background component arising from the higher energy ground-state α decays due to radiation damage in the DSSD. The decay curve for the $11/2^-$ isomer is shown in Figure 4.3(b). The fitted decay curve is described by the sum of two exponential terms arising from the overlapping α-decays and the random recoil implantation factor $f(t)$ defined in Eq. 4.2 such that

$$(A_0 e^{-\lambda_A t} + B_0 e^{-\lambda_B t}) f(t). \tag{4.3}$$

The half-life of the $11/2^-$ isomeric state has been measured to be $t_{1/2} = 1205(11)$. A comparison of the present measurements with those compiled from the literature are displayed in Fig. 4.4 and listed in Table 4.1.

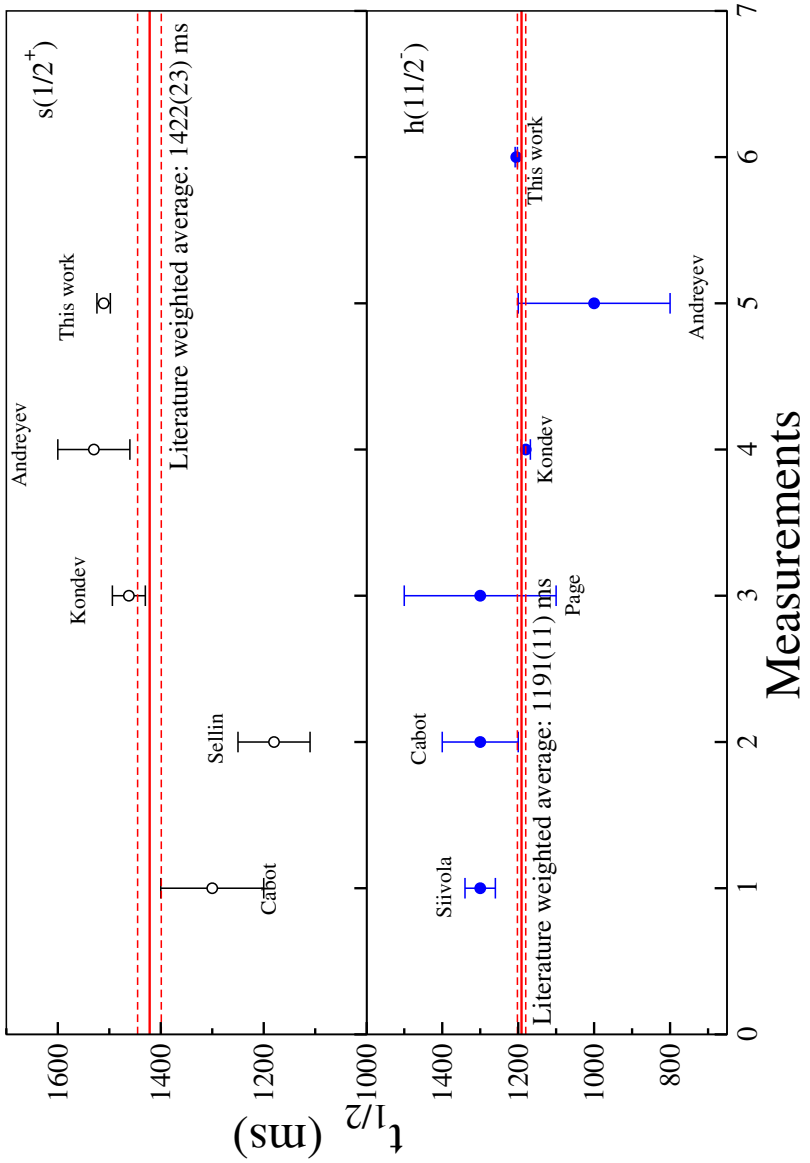

Figure 4.4: Comparison of measured half-lives with previous measurements. The solid red line indicates the error weighted mean half-life from the literature values. The dashed red lines indicate one standard deviation of the weighted mean value.

Table 4.1: Comparison of the measured α-decay properties in ^{177}Au.

Author	Year	Reference	Decay	E_α (keV)	$t_{1/2}$ (ms)	b_α (%)	Measurement Method
This work			Isomer	6118(6)	1205(3)	-	Decay correlation
			Ground state	6153(6)	1511(13)	-	
A. Siivola	[1968]	[72]	Isomer	6115(100)	1300(40)	-	Decay measurement
			Ground state	-	-	-	
H. Gauvin	[1973]	[78]	Isomer	-	-	-	Gas jet
			Ground state	6150(10)	-	-	
C. Cabot	[1974]	[79]	Isomer	6110(10)	1300(100)	65	Gas jet
			Ground state	6150(10)	1300(100)	35	
P.J. Sellin	[1991]	[80]	Isomer	-	-	-	Decay correlation
			Ground state	-	1180(70)	-	
R.D. Page	[1996]	[81]	Isomer	6118(9)	1300(200)	-	Decay correlation
			Ground state	6154(10)	-	-	
F.G. Kondev	[2001]	[20]	Isomer	6120	1180(12)	-	Decay correlation
			Ground state	6160	1462(32)	-	
A.N. Andreyev	[2009]	[73]	Isomer	6124(7)	1000(200)	66(10)	Decay correlation
			Ground state	6161(10)	1530(70)	40(6)	

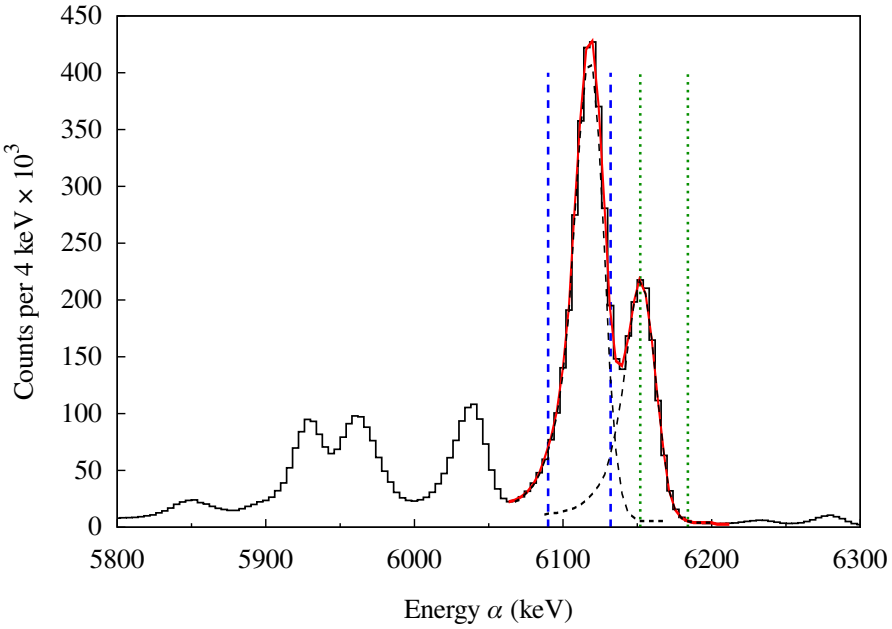

Figure 4.5: Alpha-decay spectrum indicating the total peak fit and the overlapping components. The vertical dashed (blue) and dotted (green) lines indicate the limits for the α-particle energy gates used in the recoil decay tagging correlations.

4.3.2 Recoil-decay tagging of γ-ray transitions in ^{177}Au

The recoil decay-tagging technique allows γ-rays detected at the target position to be correlated with ion implantations and their subsequent decays at the focal plane of a recoil separator. The decay properties of ^{177}Au listed in Table 4.1 are suitable for recoil decay tagging. Since there is some overlap of the ground-state and isomer α-decay peaks some care has been taken over the α decay energies used for tagging. Figure 4.5 shows fits to the overlapping peak shapes and indicates the gates used in demanding recoil-α correlations.

Figure 4.6(a) shows γ rays that are correlated with the ground-state α-decay of ^{177}Au. The search time for α decays following a recoil implant in the same pixel of the DSSD was limited to 3900 ms, which corresponds to approximately three half-lives. A total of 6.1×10^5 $\alpha(^{177g}\text{Au})$-tagged γ events were measured under these conditions. Gamma-ray transitions from the known $i_{13/2}$ band first observed by Kondev *et al.* [20] are clearly visible in Fig. 4.6(a). The γ-ray transitions correlated with the α-decay from the $11/2^-$ isomer are shown in Fig. 4.6(b). This spectrum was produced with a recoil-α correlation

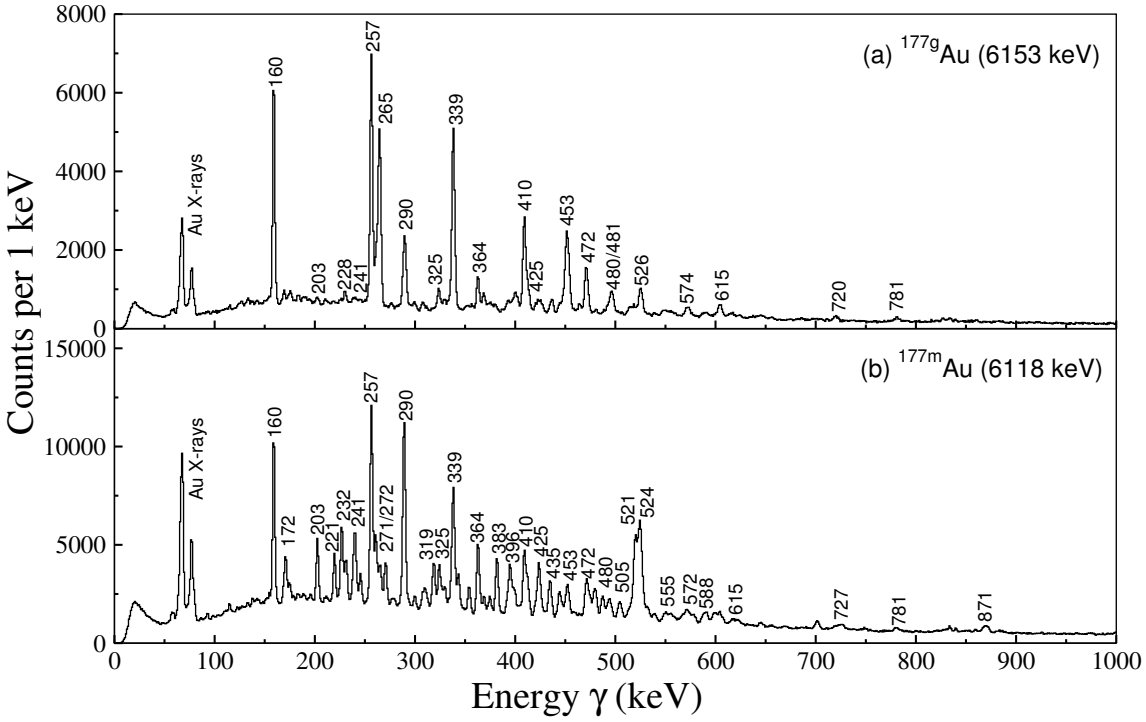

Figure 4.6: (a) Gamma-ray spectra correlated with the ground state α decay of ^{177}Au. (b) Gamma-ray spectra correlated with the α-decaying $11/2^-$ isomer of ^{177}Au. Recoil decay correlations were limited to within 3900 ms of an ion implantation into the same DSSD pixel.

time limited to 3900 ms and has a total of 2×10^6 $\alpha(^{177m}\text{Au})$-tagged γ events. The obvious difference between the tagged spectra is that, in addition to the $i_{13/2}$ band, the isomer-decay tagged spectrum contains γ rays originating from other structures in ^{177}Au.

In order to extend the level scheme for ^{177}Au the same recoil-decay correlation conditions were also used to sort two tagged γ-γ coincidence spectra. The matrices tagged on the α decays from the $1/2^+$ and $11/2^-$ states contained a total of 2.0×10^5 and 6.3×10^5 $\alpha(^{177}\text{Au})$-tagged $\gamma - \gamma$ events, respectively. The level schemes deduced from the coincidence matrices tagged on the α decay from the ground- and isomeric states in ^{177}Au are shown in Fig. 4.7 and Fig. 4.8, respectively and will be justified in the subsequent sections. The measured properties of the γ-ray transitions obtained from the matrices correlated with the α decays from the ground-state and $11/2^-$ isomers are listed in Table **??** and Table 4.3, respectively.

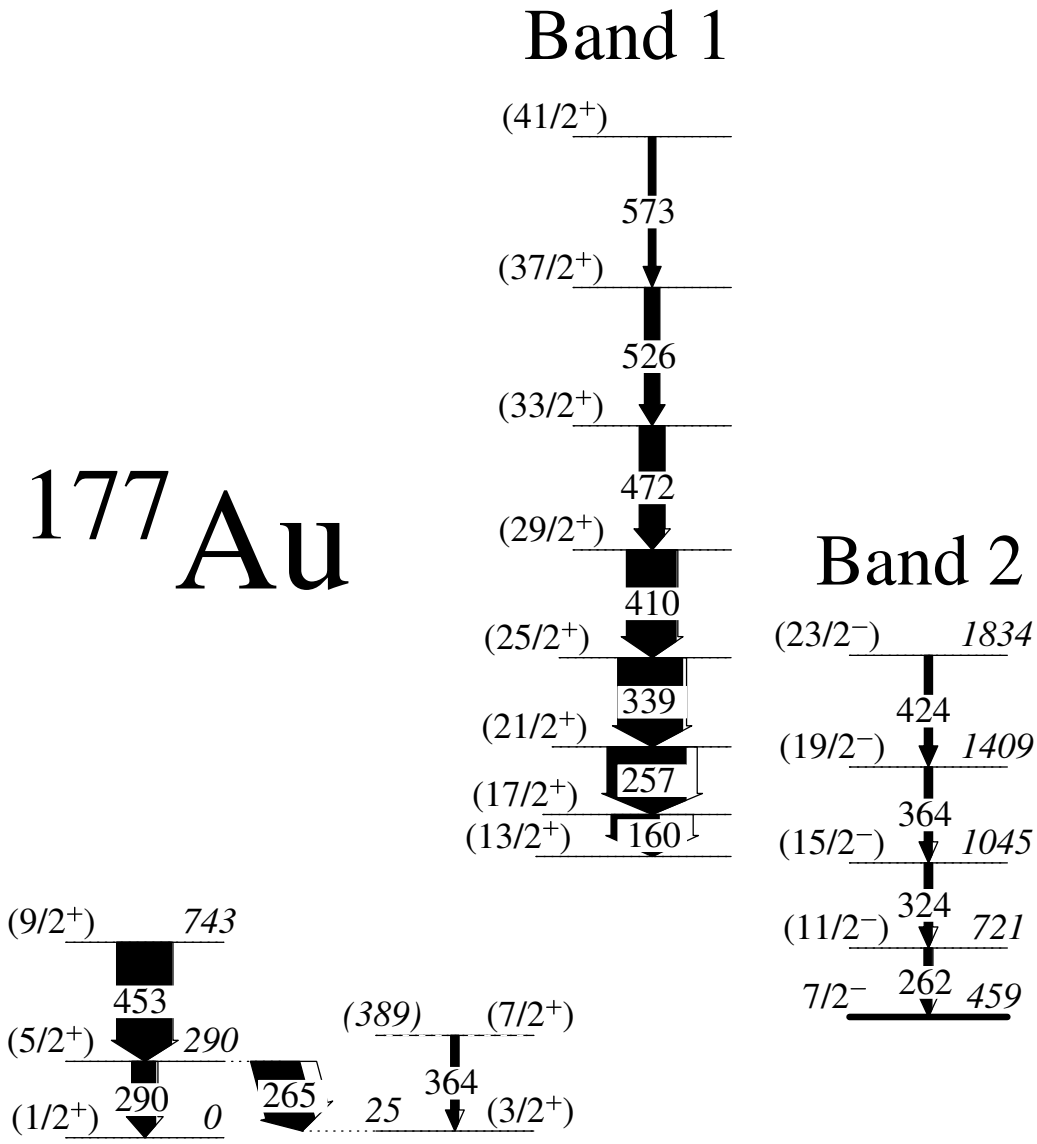

Figure 4.7: Level scheme scheme deduced for ^{177}Au from the $\gamma - \gamma$ matrix tagged with the ground state α decay. The transition energies are given in keV and their relative intensities are proportional to the widths of the arrows.

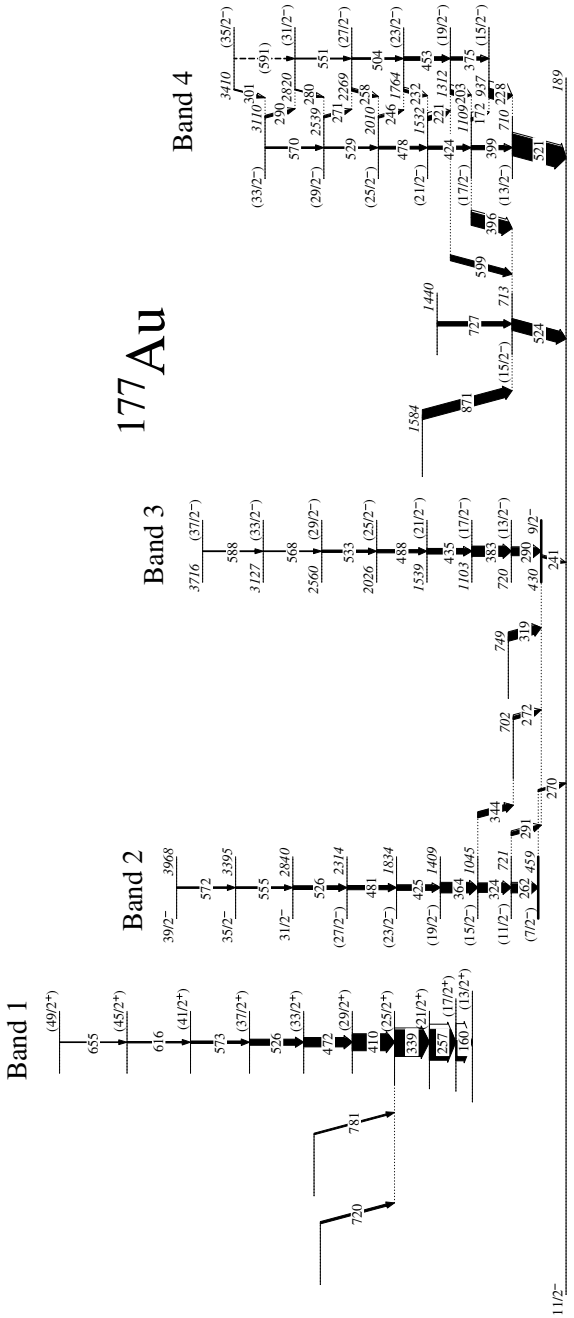

Figure 4.8: Level scheme scheme deduced for ^{177}Au from the $\gamma - \gamma$ matrix tagged with the α decay from the $11/2^-$ isomer at 189(16) keV. The transition energies are given in keV and their relative intensities are proportional to the widths of the arrows.

Table 4.2: Measured properties of γ-ray transitions assigned to ^{177}Au obtained from the $1/2^+$ $^-$ α-correlated matrix. Transition and excitation energies of the initial states have experimental uncertainties up to 1 keV.

E_γ (keV)	I_γ(%)	J_i^π	J_f^π	E_{ex} (keV)	Band
159.6	60.9(18)	$(17/2^+)$	$(13/2^+)$		1
257.2	100(3)	$(21/2^+)$	$(17/2^+)$		1
262.1	10.0(10)	$(11/2^-)$	$7/2^-$	721	2
264.8	60.2(20)	$(5/2^+)$	$(3/2^+)$	290	
290.2	30.3(10)	$(5/2^+)$	$(1/2^+)$	290	
324.6	10.0(10)	$(15/2^-)$	$(11/2^-)$	1045	2
338.9	82(3)	$(25/2^+)$	$(21/2^+)$		1
363.5	10.0(10)	$(19/2^-)$	$(15/2^-)$	1409	2
363.5	10.0(10)	$(7/2^+)$	$(3/2^+)$	389	
409.7	62.8(23)	$(29/2^+)$	$(25/2^+)$		1
425.4	10.0(10)	$(23/2^-)$	$(19/2^-)$	1834	2
452.7	69.4(22)	$(9/2^+)$	$(5/2^+)$	743	
471.8	32(3)	$(33/2^+)$	$(29/2^+)$		1
525.6	19.1(23)	$(37/2^+)$	$(33/2^+)$		1
573.5	9.3(19)	$(41/2^+)$	$(37/2^+)$		1

4.3.3 Multipolarity Assignments

The directional correlations from oriented states (DCO) method was used to assign multipolarities for the more intense transitions listed in Table 4.3. The DCO measurements were obtained by sorting the data into a $\gamma - \gamma$ matrix as outlined in Section 3.5. The angular intensities for γ rays of interest were measured by demanding coincidences with the direct feeding transition from spectra projected at the extreme and perpendicular angles relative to the beam direction. The DCO ratio was extracted using equation 3.8.

Figure 4.9 shows the DCO ratios measured for γ-ray transitions in ^{177}Au and compares these values with measurements of known stretched E2 transitions populated in ^{178}Hg taken from the same experiment. The measurements for the strongly coupled band, Band 4, which by nature has transitions with a constrained multipolarity, suggest there is not much discrimination between transitions with $\Delta I = 1$ and $\Delta I = 2$ character. The relatively high DCO ratios for the interband transitions could arise from a positive multipole mixing implying that these transitions have a mixed $M1/E2$ multipolarity. The in-band

Table 4.3: Measured properties of γ-ray transitions assigned to ^{177}Au obtained from the $11/2^-$ α-correlations. Transition and excitation energies of the initial states have experimental uncertainties up to 1 keV.

E_γ (keV)	I_γ(%)	DCO	Multipolarity	J_i^π	J_f^π	E_{ex} (keV)	Band
159.9	65.4(40)	0.80(13)	$(M1/E2)$	$(17/2^+)$	$(13/2^+)$		1
171.6	10.4(10)			$(17/2^-)$	$(15/2^-)$	1109	4
203.0	15.4(13)	1.17(47)	$(M1/E2)$	$(19/2^-)$	$(17/2^-)$	1312	4
220.6	14.2(12)	1.01(39)	$(M1/E2)$	$(21/2^-)$	$(19/2^-)$	1532	4
227.5	30.9(12)	1.45(74)	$(M1/E2)$	$(15/2^-)$	$(13/2^-)$	937	4
232.1	8.7(10)			$(23/2^-)$	$(21/2^-)$	1764	4
241.0	5.2(7)	0.9(4)	$(M1/E2)$	$9/2^-$	$(11/2^-)$	430	$3 \rightarrow 11/2^-$
245.9	5.6(8)			$(25/2^-)$	$(23/2^-)$	2010	4
257.0	100(3)	1.00(13)	$(M1/E2)$	$(21/2^+)$	$(17/2^+)$		1
258.2	6.8(9)			$(27/2^-)$	$(25/2^-)$	2269	4
261.7	29.4(9)			$(11/2^-)$	$(7/2^-)$	721	2
270.2	4.3(12)			$(7/2^-)$	$(11/2^-)$	459	$2 \rightarrow 11/2^-$
270.7	5.6(9)			$(29/2^-)$	$(27/2^-)$	2539	4
271.5	16.8(20)				$9/2^-$	702	$\rightarrow 3$
280.3	2.1(6)			$(31/2^-)$	$(29/2^-)$	2820	4
290.0	25.9(18)			$(13/2^-)$	$9/2^-$	720	3
290.2	6.4(9)			$(33/2^-)$	$(31/2^-)$	3110	4
290.9	11.1(16)			$(11/2^-)$	$9/2^-$	721	$2 \rightarrow 3$
300.6	2.4(6)			$(35/2^-)$	$(33/2^-)$	3410	4
319.4	27.1(9)	0.9(3)	$(M1/E2)$		$9/2^-$	749	$\rightarrow 3$
324.4	28.5(40)	0.73(24)	$(M1/E2)$	$(15/2^-)$	$(11/2^-)$	1045	2
338.6	85.9(28)	1.02(21)	$(E2)$	$(25/2^+)$	$(21/2^+)$		1
343.9	17.9(6)			$(15/2^-)$		1045	$2 \rightarrow$
363.6	32.3(67)	1.1(3)	$(E2)$	$(19/2^-)$	$(15/2^-)$	1409	2
374.6	10.0(13)			$(19/2^-)$	$(15/2^-)$	1312	4
383.3	31.6(11)	1.1(3)	$(E2)$	$(17/2^-)$	$(13/2^-)$	1103	3
396.0	41.3(55)			$(17/2^-)$	$(15/2^-)$	1109	$4 \rightarrow (15/2^-)$
399.1	12.7(14)	1.22(75)	$(E2)$	$(17/2^-)$	$(13/2^-)$	1109	4
409.8	52.7(35)	0.82(24)	$(E2)$	$(29/2^+)$	$(25/2^+)$		1
423.6	10.1(12)			$(21/2^-)$	$(17/2^-)$	1532	4
424.9	17.2(38)	0.87(25)	$(M1/E2)$	$(23/2^-)$	$(19/2^-)$	1834	2
435.4	17.5(12)	1.3(4)	$(E2)$	$(21/2^-)$	$(17/2^-)$	1539	3
452.7	11.5(14)	0.95(69)	$(E2)$	$(23/2^-)$	$(19/2^-)$	1764	4
471.6	29.3(25)			$(33/2^+)$	$(29/2^+)$		1
478.0	8.8(14)			$(25/2^-)$	$(21/2^-)$	2010	4
480.6	13.3(31)			$(27/2^-)$	$(23/2^-)$	2314	2
487.8	10.2(9)			$(25/2^-)$	$(21/2^-)$	2026	3
504.4	5.1(11)			$(27/2^-)$	$(23/2^-)$	2269	4
520.7	68.0(120)	0.59(14)	$(M1/E2)$	$(13/2^-)$	$(11/2^-)$	710	$4 \rightarrow 11/2^-$
523.8	35.9(115)	1.5(5)	$(M1/E2)$	$(15/2^-)$	$(11/2^-)$	713	
525.6	19.2(20)			$(37/2^+)$	$(33/2^+)$		1
525.9	11.8(28)			$(31/2^-)$	$(27/2^-)$	2840	2
528.9	4.8(10)			$(29/2^-)$	$(25/2^-)$	2539	4
533.1	7.5(8)			$(29/2^-)$	$(25/2^-)$	2560	3
551.0	3.0(10)			$(31/2^-)$	$(27/2^-)$	2820	4

Table 4.4: Table 4.3 continued.

E_γ (keV)	I_γ(%)	DCO	Multipolarity	J_i^π	J_f^π	E_{ex} (keV)	Band
555.2	5.3(16)			$(35/2^-)$	$(31/2^-)$	3395	2
567.8	2.3(5)			$(33/2^-)$	$(29/2^-)$	3127	3
570.4	5.0(12)			$(33/2^-)$	$(29/2^-)$	3110	4
572.4	4.8(13)			$(39/2^-)$	$(35/2^-)$	3968	2
572.6	7.8(20)			$(41/2^+)$	$(37/2^+)$		1
588.2	2.5(5)			$(37/2^-)$	$(33/2^-)$	3716	3
599.0	18.3(39)			$(19/2^-)$	$(15/2^-)$	1312	$4 \rightarrow (15/2^-)$
590.1	1.0(5)			$(35/2^-)$	$(31/2^-)$	3410	4
616.0	4.4(10)			$(45/2^+)$	$(41/2^+)$		1
654.7	2.1(7)			$(49/2^+)$	$(45/2^+)$		1
720.0	7.1(12)				$(25/2^+)$		$\rightarrow 1$
727.2	14(35)				$(15/2^-)$	1440	$\rightarrow (15/2^-)$
870.8	31.2(57)				$(15/2^-)$	1584	$\rightarrow (15/2^-)$

γ rays from Bands 1, 2, 3 and 4 in ^{177}Au are similar to those measured for the stretched E2 transitions in the ground-state band of ^{178}Hg. Thus these transitions are assigned as stretched E2 transitions. All multipolarity assignments are tentative due to the lack of distinction between dipole and quadrupole transitions.

4.3.4 Band 1 - The $i_{13/2}$ intruder band

The structure labelled Band 1 in Fig. 4.7 and Fig. 4.8 was first observed by Kondev *et al.* in a recoil-decay tagging experiment that exploited the GAMMASPHERE spectrometer in conjunction with the Fragment Mass Analyzer at the Argonne National Laboratory [20]. This band was interpreted as the $i_{13/2}$ proton intruder band. Kondev *et al.* noted that the $13/2^+$ band head had decay paths that proceeded to both α decaying states. Figure 4.10(a) and Fig. 4.10(b) show the spectra of γ rays in coincidence with the 160 keV ($17/2^+ \rightarrow 13/2^+$) transition extracted from the coincidence matrices tagged by the ground state and $11/2^-$ α decays, respectively. The correlation times were limited to 3900 ms.

Figure 4.11 shows γ-ray transitions in coincidence with 265 keV, 290 keV and 453 keV in addition to those in Band 1. These γ rays were identified by Kondev *et al.* and assigned to the decay path from Band 1 to the ground state, see Fig. 4.1. Figure 4.11 shows further γ ray coincidence spectra from the matrix tagged with the ground-state α decay. These spectra show that 265 keV and 290 keV are both in coincidence with the 453 keV transition

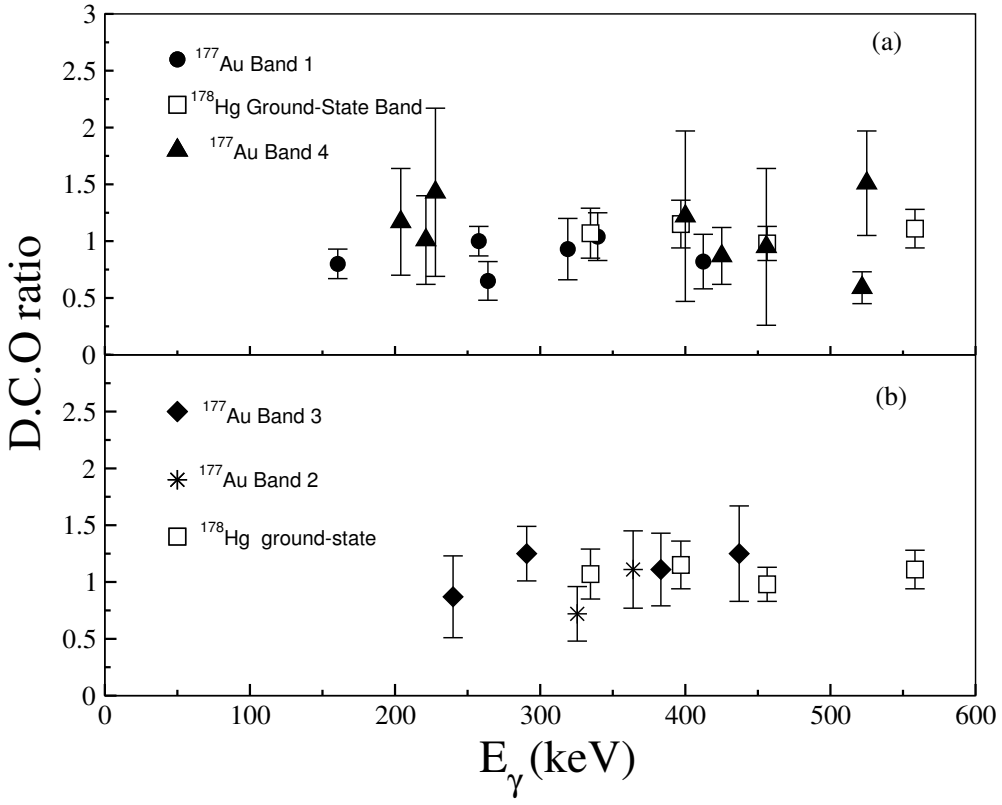

Figure 4.9: DCO ratios extracted for γ-ray transitions in ^{177}Au using recoil-decay tagged data. (a) DCO measurements for Band 1 and Band 4. (b) DCO measurements for Band 2 and Band 3. DCO measurements of known $\Delta I = 2$ transitions in the ground-state band of ^{178}Hg are shown for comparison.

but not with each other. Kondev *et al.* [20] assigned the 290 keV and 453 keV transitions to be a cascade with the former transition depopulating the $13/2^+$ bandhead directly. The 265 keV transition was assigned to form a parallel branch to the 290 keV from a nearby 9/2 or 11/2 state.

Andreyev *et al.* observed a state in ^{177}Au at an excitation energy of 31(16) keV populated by a weak α-decay branch from the $9/2^-$ isomer in ^{181}Tl [73]. This state was tentatively assigned to have a spin and parity $5/2^+$. On the basis of this information, the low-spin states are reordered so that the 453 keV transition feeds a state that is de-excited by parallel 265 keV and 290 keV γ rays. The 290 keV transition is assigned to feed the ground state, which fixes the first excited state at an excitation energy of 25(1) keV. This is consistent with the assignment of Andreyev *et al* but with a greater precision. A similar low-lying state has been seen in the γ-ray de-excitation following the α decay of the $9/2^-$

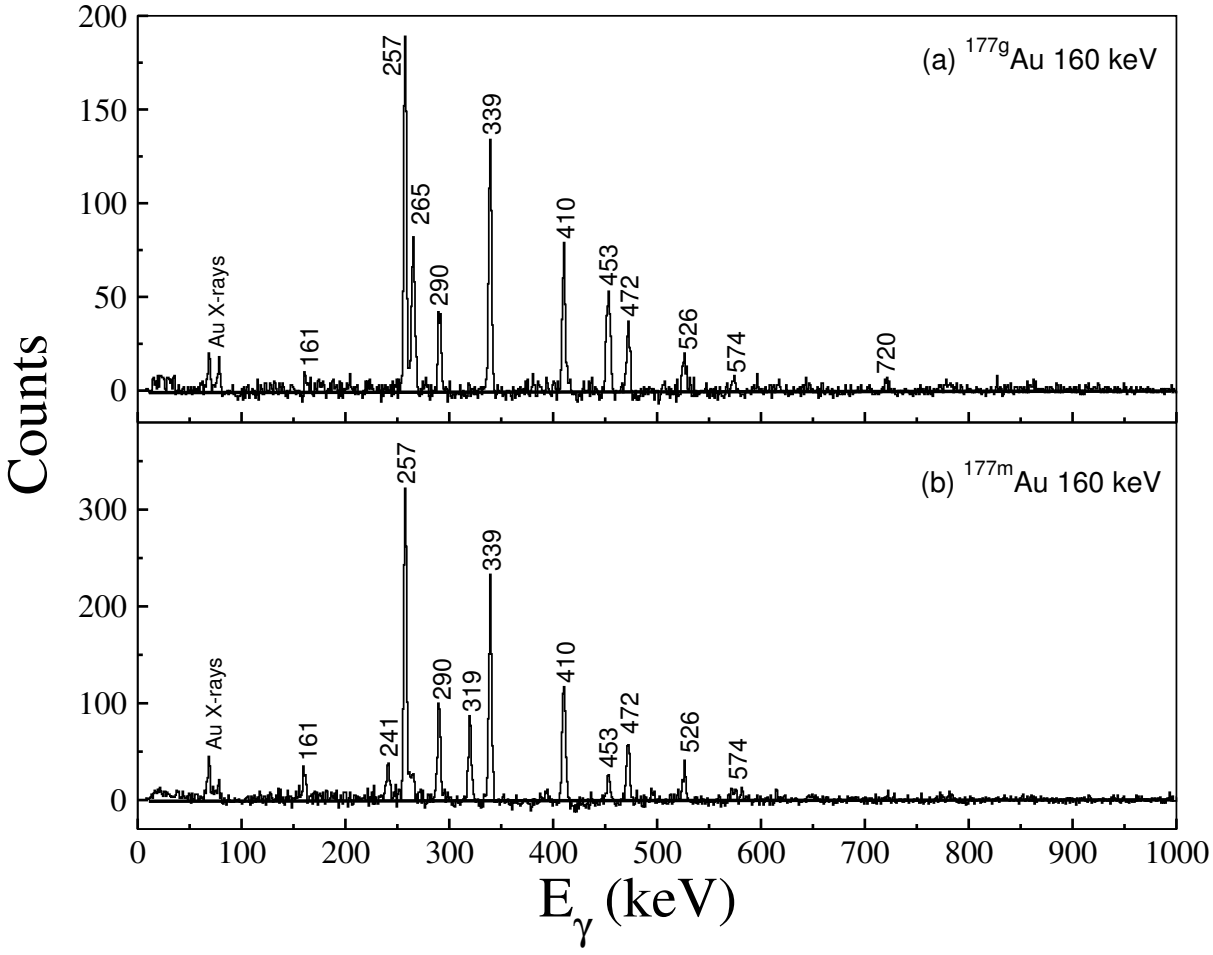

Figure 4.10: Gamma rays in coincidence with the 160 keV ($17/2^+ \rightarrow 13/2^+$) transition extracted from the recoil-decay tagged $\gamma - \gamma$ coincidence matrices. (a) Coincidences from matrix correlated with the ground-state (E_α=6153 keV) α decay. (b) Coincidences from matrix correlated with the $11/2^-$ (E_α=6118 keV) α decay.

isomer in ^{183}Tl [16]. The analogous ($3/2^+$ or $1/2^+$) state in ^{179}Au was observed by Venhart *et al.* at an excitation energy of 27.1 keV and assigned an M1 multipolarity on the basis of intensity balances.

Figure 4.10(b) shows γ rays in coincidence with the 160 keV transition from the matrix tagged by the α decay from the $11/2^-$ isomer. In this spectrum the 265 keV and 453 keV transitions are observed at much lower intensities and are likely to be present due to correlations with the overlapping ground-state α decay tail. In addition to the transitions of Band 1, γ rays at 161 keV, 241 keV, 290 keV and 319 keV are also observed. The

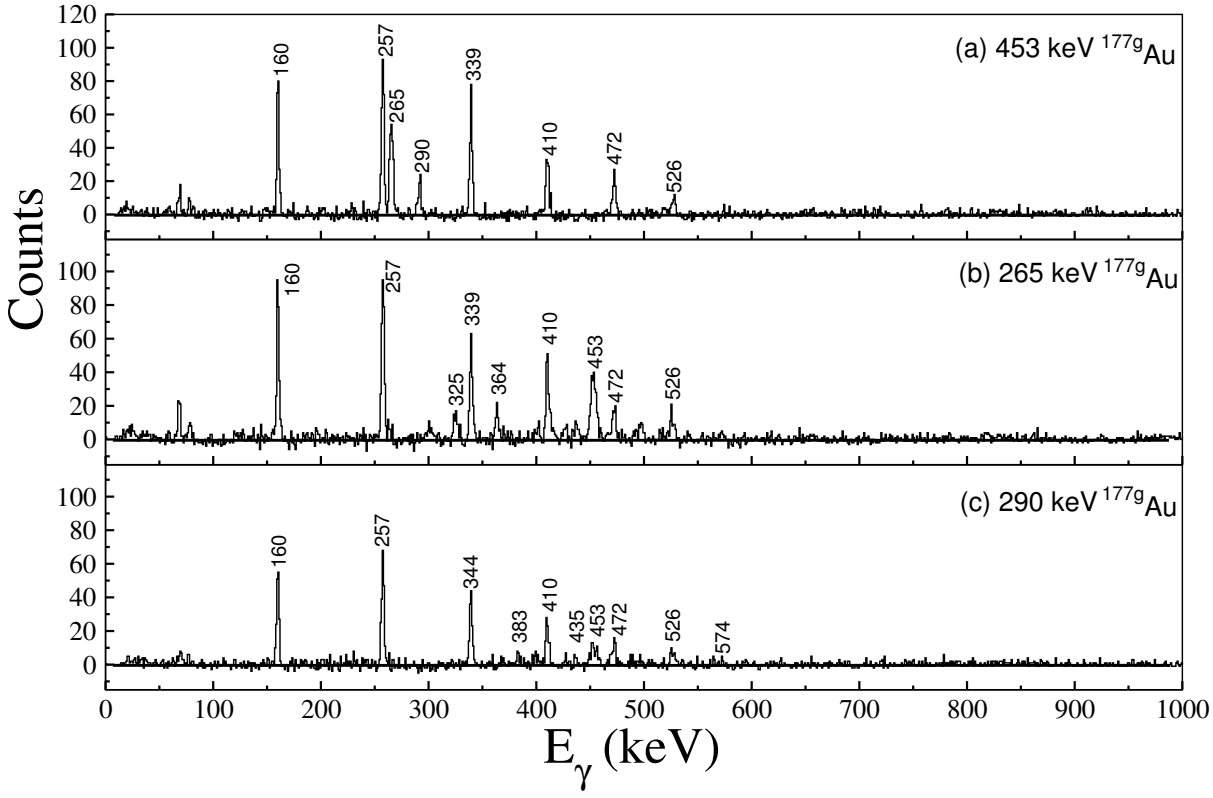

Figure 4.11: Gamma-ray coincidence spectra extracted from the recoil-decay tagged $\gamma-\gamma$ coincidence matrices correlated with the ground-state (E_α=6153 keV) α decay. (a) Gamma rays in coincidence with the 453 keV transition. (b) Gamma rays in coincidence with the 265 keV transition. (c) Gamma rays in coincidence with the 290 keV transition.

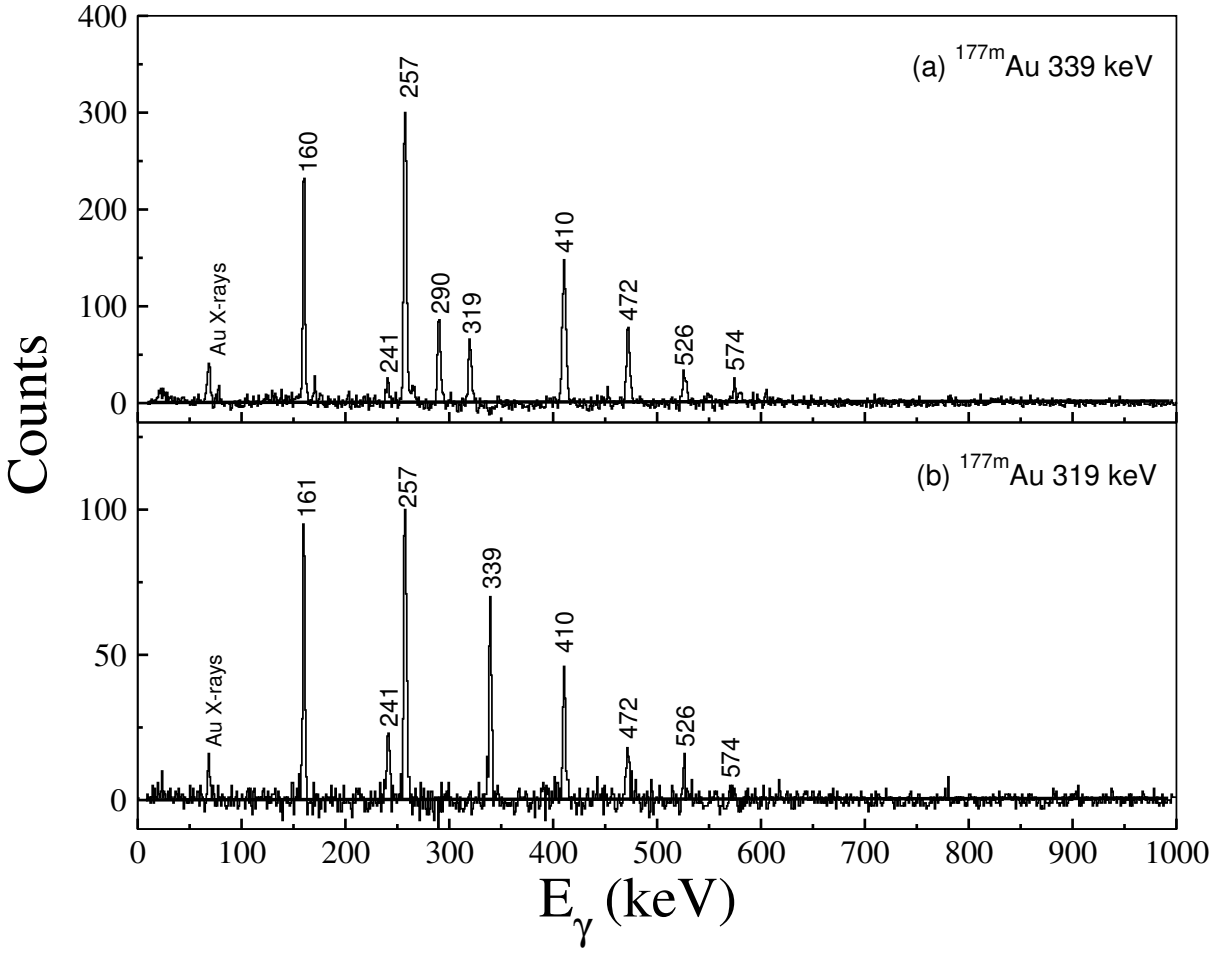

Figure 4.12: Gamma-ray coincidence spectra extracted from the recoil-decay tagged $\gamma-\gamma$ coincidence matrices correlated with the $11/2^-$ (E_α=6118 keV) α decay. (a) Gamma rays in coincidence with the 339 keV transition. (b) Gamma rays in coincidence with the 319 keV transition.

161 keV transition is also observed in Fig. 4.10(a) and cannot be placed firmly in the level scheme.

Figure 4.12(a) shows γ rays in coincidence with the 339 keV in-band transition. The 241 keV, 290 keV and 319 keV γ rays are all in coincidence with the Band 1 cascade. This 290 keV γ ray is different to the γ ray with the same transition energy associated with the cascades feeding the ground state. This is confirmed by the absence of the 265 keV and 453 keV γ rays in Fig. 4.12(a), which is extracted from the isomer-tagged matrix. It is apparent from Fig. 4.12(b) that the 319 keV transition is not in coincidence with the

290 keV transition yet both transitions are in coincidence with the 241 keV γ ray.

The 241 keV γ ray is assumed to be the same transition that was identified following the $9/2^- \rightarrow 11/2^-$ unhindered α decay from ^{181}Tl [73]. Andreyev *et al.* assigned an M1 multipolarity to this transition, which connects a $9/2^-$ state to the α-decaying $11/2^-$ isomer in ^{177}Au.

It has not been possible to observe discrete linking transitions that connect the $13/2^+$ state to the states above the α-decay states. The decay branching has been estimated by considering the ratio of transition intensities of the 290 keV, 319 keV and 453 keV transitions relative to the 339 keV transition in Band 1. The ratios for the 290 keV and 319 keV transitions were measured from the isomer tagged $\gamma - \gamma$ coincidence matrix. The transition intensities were extracted assuming multipolarities of pure E2 and M1 for the 290 keV and 319 keV, respectively. The ratio for the 453 keV transition was measured from the ground-state tagged $\gamma - \gamma$ coincidence matrix. The transition intensity was deduced assuming a pure E2 multipolarity. From these ratios the 290 keV, 319 keV and 453 keV transitions were observed to have decay branches at 29%, 33% and 38%, respectively. The decay from the $13/2^+$ is unusual since it feeds both positive and negative-parity states. The decay paths and the absence of an observed γ-ray decay will be discussed in Section 4.4.1.

4.3.5 Band 2 - The $f_{7/2}$ intruder band

The recoil-decay tagged coincidence analysis has revealed a new collective band structure, which is labelled as Band 2 in Fig. 4.7 and Fig. 4.8. Band 2 extends to an excitation energy of 3968 keV and a tentative spin-parity of $39/2^-$. The band head at an excitation energy of 459 keV decays via paths to both the ground state and the $11/2^-$ isomer. Figure 4.13 shows a spectrum of γ rays in coincidence with the 324 keV transition from the $\gamma - \gamma$ coincidence matrices correlated with both ^{177}Au α decays. The spectrum correlated with the ground-state α decay, Fig. 4.13(a), shows the transitions in Band 2 but there is no obvious evidence for discrete linking transitions to the ground state.

The isomer-decay correlated spectrum shown in Fig. 4.13(b) shows several γ rays in addition to the in-band transitions. The coincidence analysis has revealed multiple decay

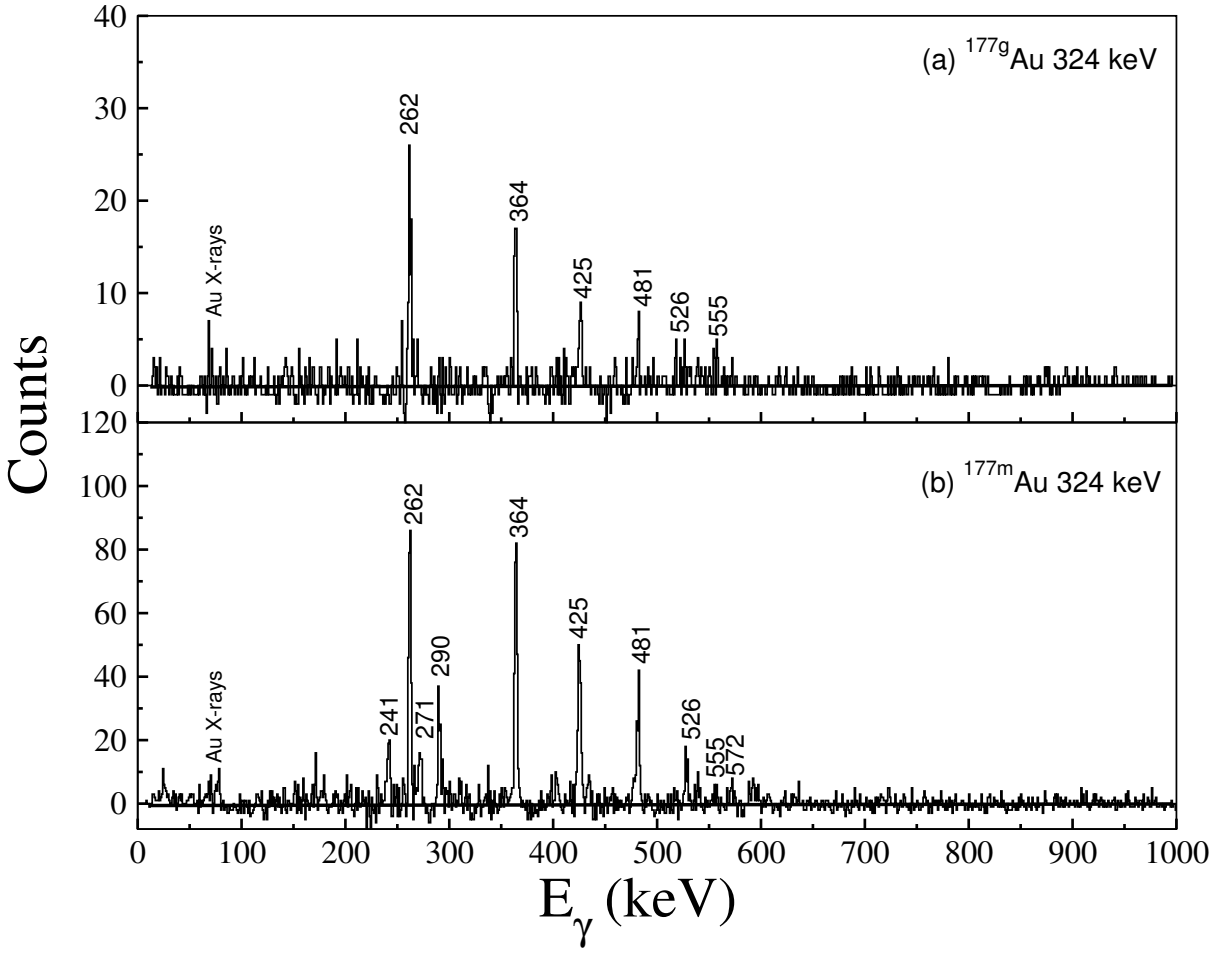

Figure 4.13: (a) Spectrum of γ rays in coincidence with the 324 keV transition in Band 2 extracted from the recoil-decay tagged $\gamma - \gamma$ coincidence matrices correlated with the ground-state (E_α=6153 keV) α decay. (b) Spectrum of γ rays in coincidence with the 324 keV transition in Band 2 extracted from the recoil-decay tagged $\gamma - \gamma$ coincidence matrices correlated with the isomer (E_α=6118 keV) α decay.

branches to the $11/2^-$ α-decaying state. There is a direct decay from the band head to the $11/2^-$ isomer via a 270 keV transition. There is an indirect route to the isomer via the $9/2^-$ state identified by Andreyev *et al.* [73] observed as a γ-ray cascade comprising a 291 keV and 241 keV transitions. A further three-step sequence of 344 keV, 272 keV and 241 keV connects the excited state at 1045 keV with the isomer, see Fig. 4.14.

Figure 4.14(b) shows γ rays in coincidence with the 364 keV transition from the $\gamma - \gamma$ coincidence matrices correlated with both α decays from ^{177}Au. Figure 4.14(a) shows that the 364 keV appears to be a self-coincident energy doublet, however the second

component is not apparent in the coincidence spectrum gated on the 364 keV transition in the isomer-correlated matrix shown in Fig. 4.14(b). This indicates that the second 364 keV transition belongs to the decay path from Band 2 to the ground state. The presence of decay paths to both α-decaying states in ^{177}Au is confirmed in the α-decay spectra in delayed coincidence with the 324 keV γ-ray transition shown in Fig. 4.15(d). The 160 keV and 324 keV from Bands 1 and 2, respectively have correlations with both ^{177}Au α decays whereas the 383 keV and 203 keV transition are connected with only the α-decay from the $11/2^-$ isomeric state. Several other transitions are common to both spectra at 414 keV and 475 keV but there is insufficient information to place these firmly into the level scheme.

The intensity of the 270 keV linking transition that connects the band head (E_x=459 keV) to the $11/2^-$ isomer has a much lower intensity than the 262 keV in-band transition that feeds the band head directly. This might suggest that the band head state is a short-lived (nanosecond) isomer, which decays downstream of the focus of the JUROGAM spectrometer resulting in a lower detection efficiency for this transition.

4.3.6 Band 3 - The $h_{9/2}$ intruder band

A band structure based on the $9/2^-$ state in ^{177}Au that was identified in the α decay of ^{181}Tl [73] was observed in the recoil-decay tagged coincidence analysis. The band is labelled as Band 3 in Fig. 4.8 and comprises seven transitions extending to a state at an excitation energy of 3716 keV and a tentative spin-parity assignment of $37/2^-$. This band was included in the evaluated nuclear structure data tables [82] but there are no further details published in the literature. An analysis of the $\gamma - \gamma$ coincidence matrices correlated with both α decays reveals that this band decays exclusively to the $11/2^-$ isomeric state. Band 3 has only a single observed linking transition from the band head to the $11/2^-$ isomer via a 241 keV transition that was also observed in the α decay of ^{181}Tl [73]. However, the $9/2^-$ band head at 430 keV is a key intermediate state in the decay paths of Bands 1 and 2 to the $11/2^-$ isomer.

Figure 4.16 shows typical γ ray coincidence spectra highlighting the transitions in

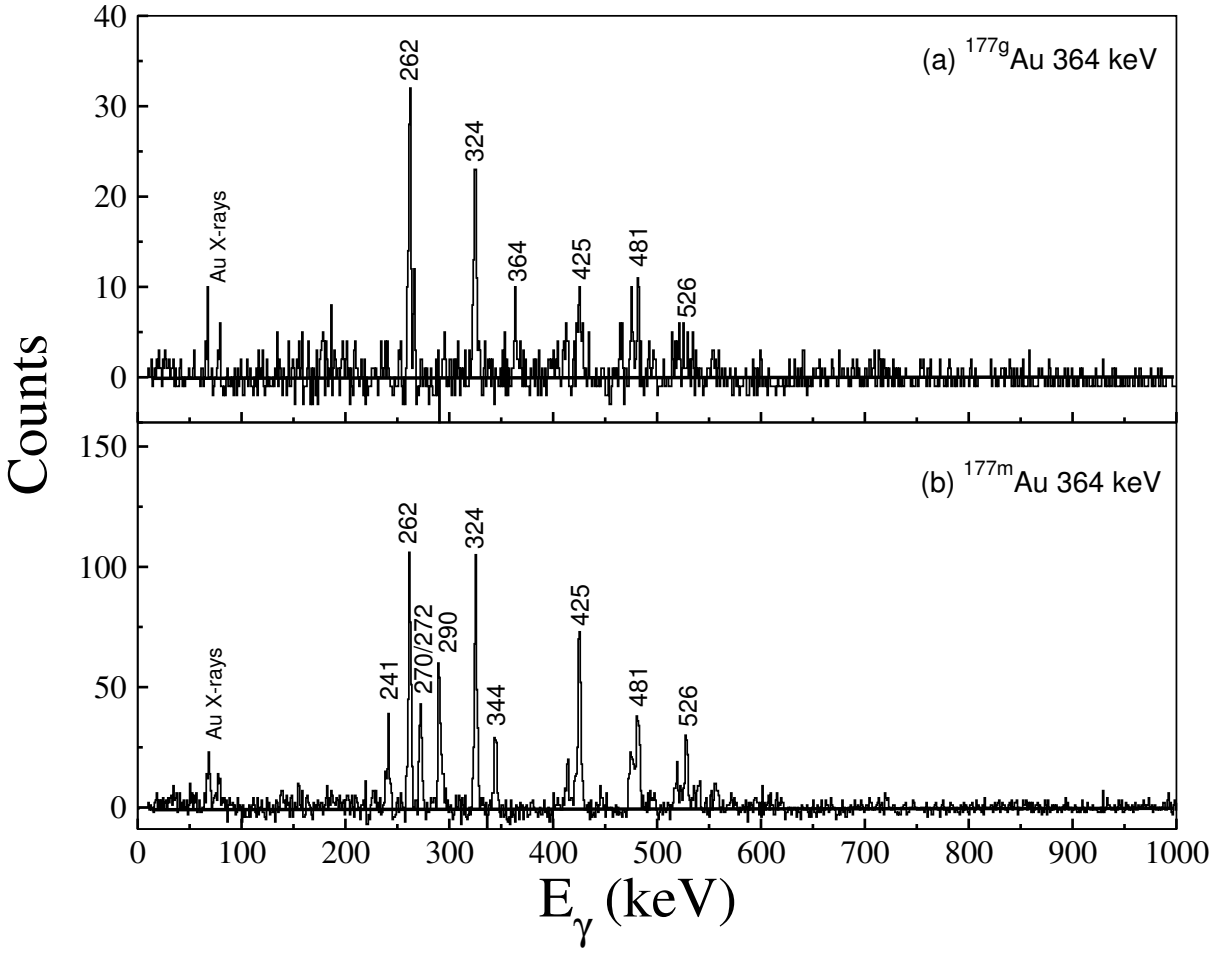

Figure 4.14: (a) Spectrum of γ rays in coincidence with the 364 keV transition in Band 2 extracted from the recoil-decay tagged $\gamma - \gamma$ coincidence matrices correlated with the ground-state (E_α=6153 keV) α decay. (b) Spectrum of γ rays in coincidence with the 364 keV transition in Band 2 extracted from the recoil-decay tagged $\gamma - \gamma$ coincidence matrices correlated with the isomer (E_α=6118 keV) α decay.

Band 3. Figure 4.16 shows the 241 keV transition, which forms the single-step decay from the band head, in addition to the transitions of Band 3. Figure 4.16 also shows a γ ray at 272 keV, which hints at another decay path via either (or both) of the states at 459 keV or 702 keV. Such a path could not be elucidated with the present data.

The relative intensity of the 241 keV linking transition is much lower than the 290 keV transition that directly feeds the band head. A complementary experiment using the SAGE γ-ray - conversion electron coincidence spectrometer [83] provides some evidence for the $9/2^-$ state being a short-lived (nanosecond) isomer [84]. A brief study of ^{177}Au

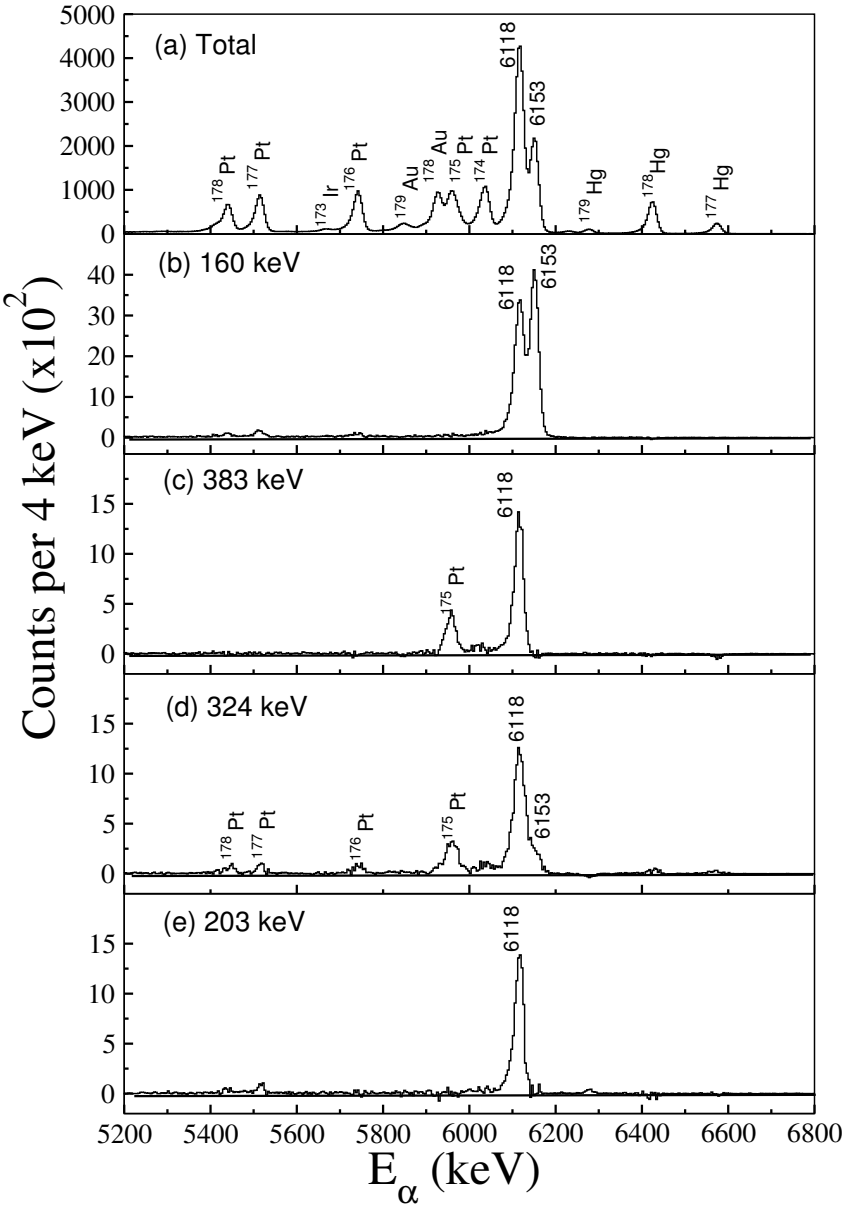

Figure 4.15: Alpha-decay spectra in delayed coincidence with selected γ-ray transitions from an $\alpha - \gamma$ matrix. (a) The matrix projection showing all α decays. (b) α particles in delayed coincidence with the 160 keV transition from Band 1. (c) α particles in delayed coincidence with the 383 keV transition from Band 3. (d) α particles in delayed coincidence with the 324 keV transition from Band 2. (e) α particles in delayed coincidence with the 203 keV transition from Band 4.

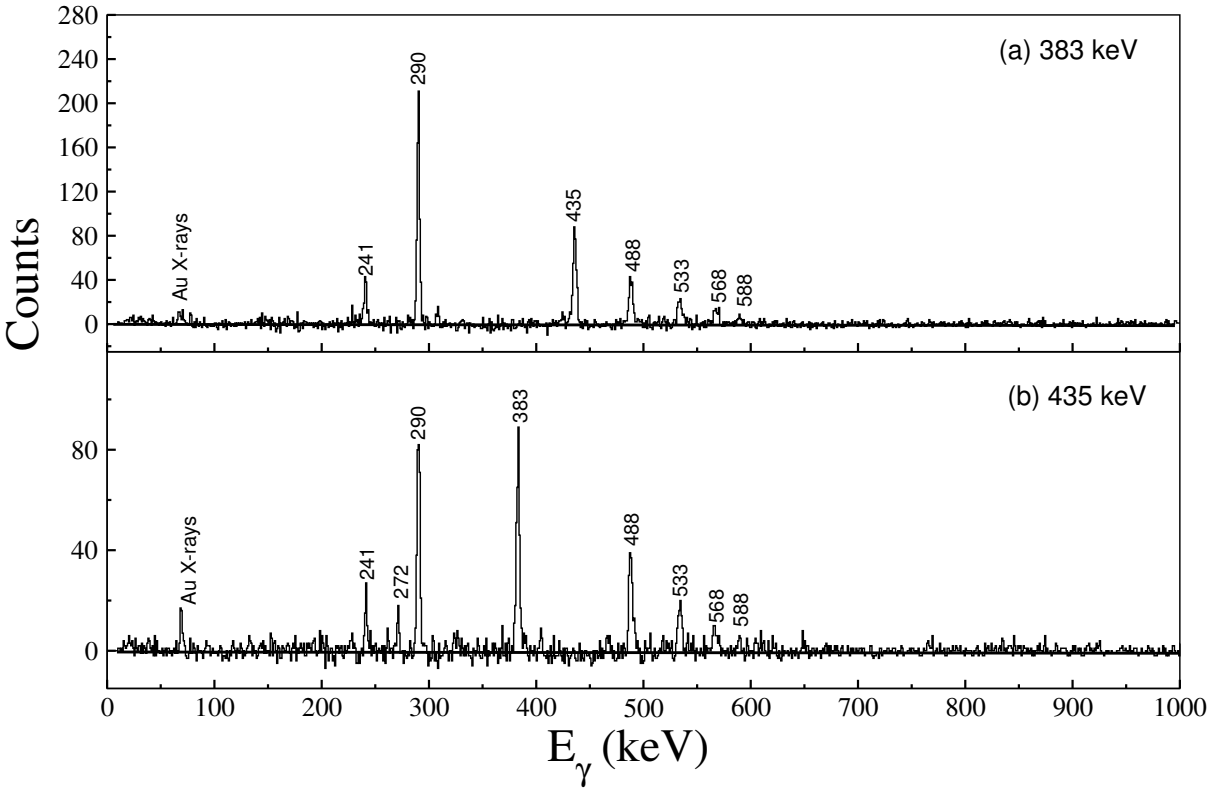

Figure 4.16: Gamma-ray spectra obtained from recoil-decay tagged $\gamma - \gamma$ coincidence matrices correlated with the isomer (E_α=6118 keV) α decay (a) Gamma rays in coincidence with the 383 keV transition. (b) Gamma rays in coincidence with the 435 keV transition.

was performed as part of the commissioning experiments of the SAGE spectrometer. An objective of the commissioning experiments was to test the capabilities of the SAGE spectrometer for establishing transition multipolarities by measuring internal conversion coefficients. The measurements revealed anomalous conversion coefficients for the 241 keV transition, which could not be reconciled with the in-beam measurements reported here. The anomalous measurments were attributed to a nanosecond lifetime of the $9/2^-$ state. If the $9/2^-$ state was a nanosecond isomer, the γ rays would be measured with a lower detection efficiency since they would be emitted from a point downstream from the focus of the SAGE spectrometer array. However, the conversion electrons were transported to the SAGE Si detector in the magnetic field of the solenoid and experienced no comparable loss in detection efficiency. These conditions provided an explanation of the spurious conversion coefficients and, with the spectra from the present work, support the scenario

that the $9/2^-$ state is a nanosecond isomer.

Bands 2 and 3 have states at excitation energies of 721 keV and 720 keV that decay via γ rays with transition energies at 291 keV and 290 keV, respectively. It is tempting to consider that these are not distinct states that are accidentally degenerate but the same state. Figure 4.16(a) shows γ rays in coincidence with the 383 keV transition that feeds the 720 keV state directly. If the 324 keV transition from Band 2 and the 383 keV transition fed the same state then the 262 keV transition that depopulates the 721 keV state in Band 2 should be observed in Fig. 4.16(a). There is no evidence for this transition in the spectrum therefore it is concluded that these near degenerate states are distinct and separate.

4.3.7 Band 4 and its decay paths.

Figure 4.17(a) and Fig. 4.17(b) show γ rays in coincidence with the 228 keV and 203 keV transitions, respectively using the matrix correlated with the α-decay from the $11/2^-$ isomer. These spectra show two groupings of γ rays at low and high energy. The γ-ray coincidence analysis has revealed that these transitions form a strongly coupled band structure, which is labelled as Band 4 in Fig. 4.8. The strongly coupled band in ^{177}Au was included in the evaluated nuclear structure data tables [82] but there are no further details published in the literature. In this work the band is observed up to an excitation energy of 3410 keV and spin $(35/2^-)$. The recoil-decay tagged γ-ray coincidence analysis reveals that the strongly coupled band decays exclusively to the $11/2^-$ isomer. Three decay paths from Band 4 to the $11/2^-$ isomer have been identified. Figure 4.17(a) shows a 521 keV transition that connects the lowest energy level observed in the strongly coupled band (E_x=710 keV) with the $11/2^-$ α-emitting isomer. A further decay path is observed from the 1109 keV state via a 396 keV transition to an intermediate state at 713 keV, which decays directly to the $11/2^-$ isomer through a 524 keV γ ray. A third weak decay branch is observed from the 1312 keV level that proceeds via a 599 keV transition to the 713 keV level, which is depopulated via the 524 keV γ-ray transition, see Fig. 4.18(b).

In addition to the 599 keV γ ray depopulating the strongly coupled band, the state at

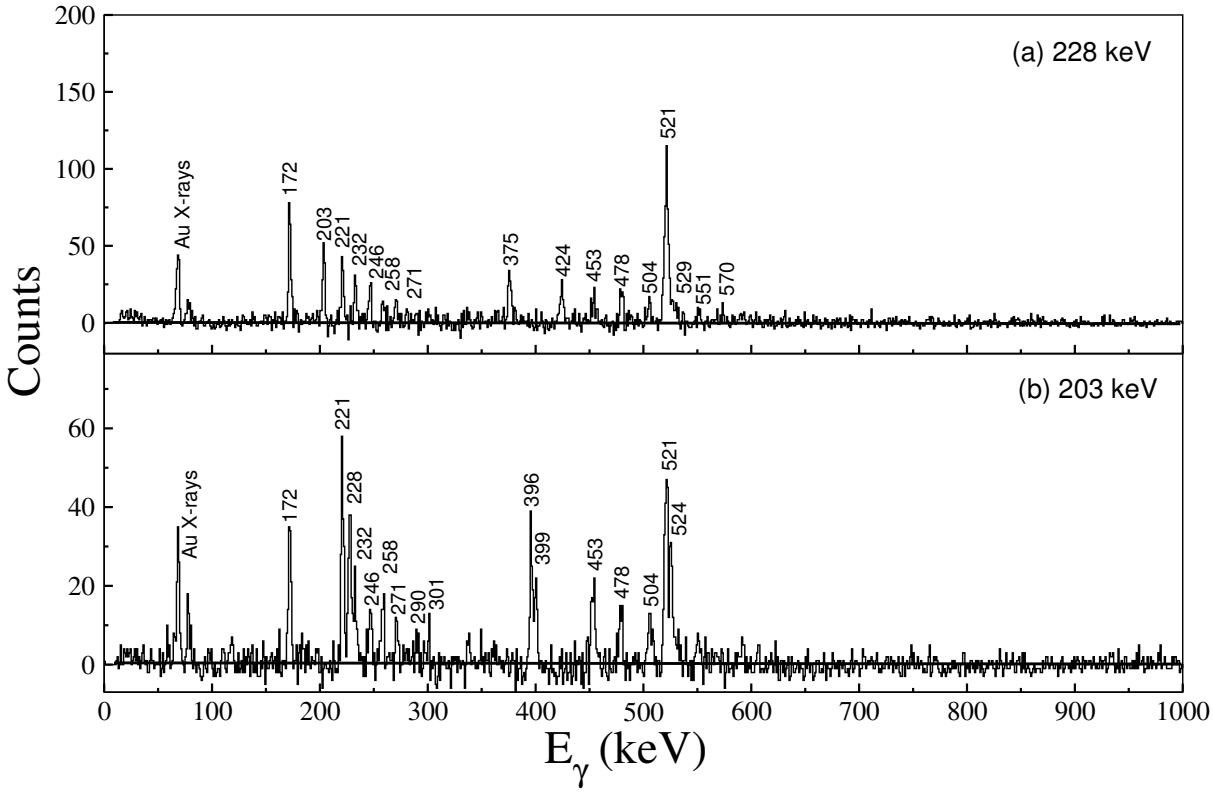

Figure 4.17: Gamma-ray spectra obtained from recoil-decay tagged $\gamma - \gamma$ coincidence matrices correlated with the isomer (E_α=6118 keV) α decay showing transitions in the strongly coupled band (Band 4) in ^{177}Au. (a) Gamma rays in coincidence with the 228 keV transition. (b) Gamma rays in coincidence with the 203 keV transition.

713 keV is fed by 727 keV and 871 keV γ rays, which depopulate other parallel configurations. The coincidence relationships between the 524 keV transition depopulating the 713 keV state and its feeding transitions are shown in Fig. 4.18. It has not been possible to deduce the multipolarities of these transitions in this experiment.

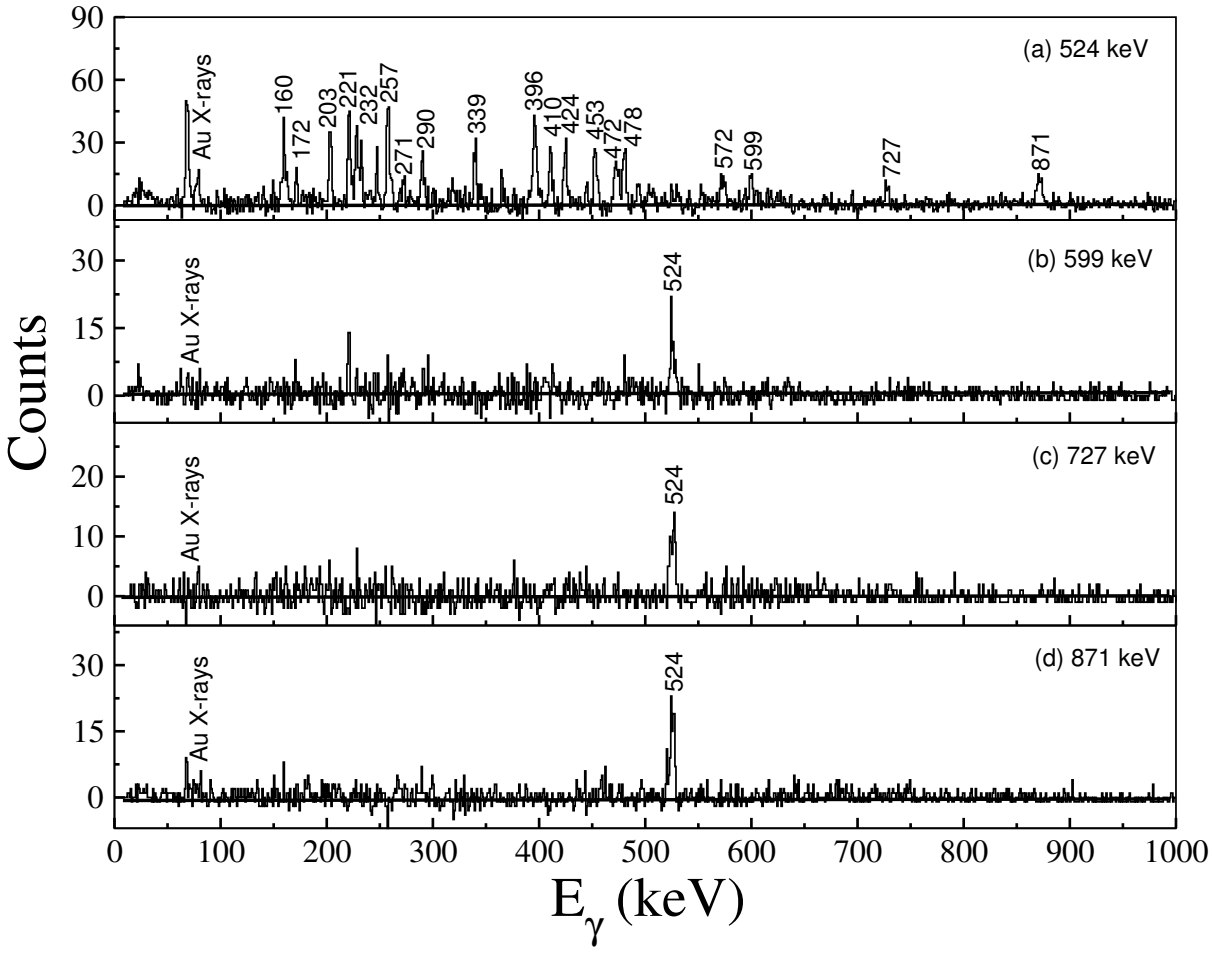

Figure 4.18: Gamma-ray spectra obtained from recoil-decay tagged $\gamma - \gamma$ coincidence matrices correlated with the isomer (E_α=6118 keV) α decay showing transitions feeding the 713 keV state in ^{177}Au. (a) Gamma rays in coincidence with the 524 keV transition. Contamination from transitions in Band 1 is seen due to an overlapping peak from the 526 keV transition. (b) Gamma rays in coincidence with the 599 keV transition. (c) Gamma rays in coincidence with the 727 keV transition. (b) Gamma rays in coincidence with the 871 keV transition.

4.4 Discussion

The ^{177}Au nucleus has one unpaired proton that forms the basis for the coexisting structures identified in this experiment. Figure 4.19 shows a representative Nilsson diagram for the $Z \sim 82$ region. At low excitation energy, the single proton can occupy the $3s_{1/2}, 2d_{3/2}$ and $1h_{11/2}$ states below the $Z = 82$ shell gap. Laser spectroscopy measurements performed at the CERN-ISOLDE facility have established the ground-state spin and parity to be a $I^{\pi} = 1/2^{+}$ configuration [77] .

The low-lying isomer at an excitation energy of 189(16) keV [73] is an yrast trap based on a proton-hole in the $h_{11/2}$ state. The energy level systematics deduced from the previous works on the Au isotope chain shows that the excitation energy of the $\pi h^{-1}_{11/2}$ band head is almost constant from the line of stability (^{189}Au) to the proton drip line (^{171}Au), see Figure 4.20. However, the excitation energy of $\pi h^{-1}_{11/2}$ proton-hole structure increases with increasing neutron number due to the reduced valence space as the $N = 126$ closed shell is approached.

Figure 4.19 shows that the $Z = 82$ shell gap is sufficiently narrow at certain quadrupole deformations to allow coexisting configurations to be built on proton excitations across the closed shell. Intruder configurations based on $1p-4h$ excitations can be formed by exciting the single proton into the steeply downward-sloping $\pi f_{7/2}$ ($1/2^{-}[530]$), $\pi h_{9/2}$ ($9/2^{-}[505]$, $1/2^{-}[541]$, $3/2^{-}[532]$) and $\pi i_{13/2}$ ($1/2^{+}[660]$) orbitals.

4.4.1 The intruder states

The states that have been observed in the present work are likely to be based on proton-hole excitations across the $Z = 82$ shell gap. The relative excitation energies of the band head configurations in ^{177}Au can provide constraints on theoretical models that predict single-particle energies near the proton drip line. The excitation energies of the intruder states in ^{177}Au are fixed except for the band head of the $i_{13/2}$ intruder configuration. The coincidence spectra shown in Fig. 4.10 and Fig. 4.11 indicate that there are decay paths to the positive-parity ground state and the negative-parity $11/2^{-}$ isomer, see Fig. 4.21. However, no discrete linking transitions have been identified. The non-observation of

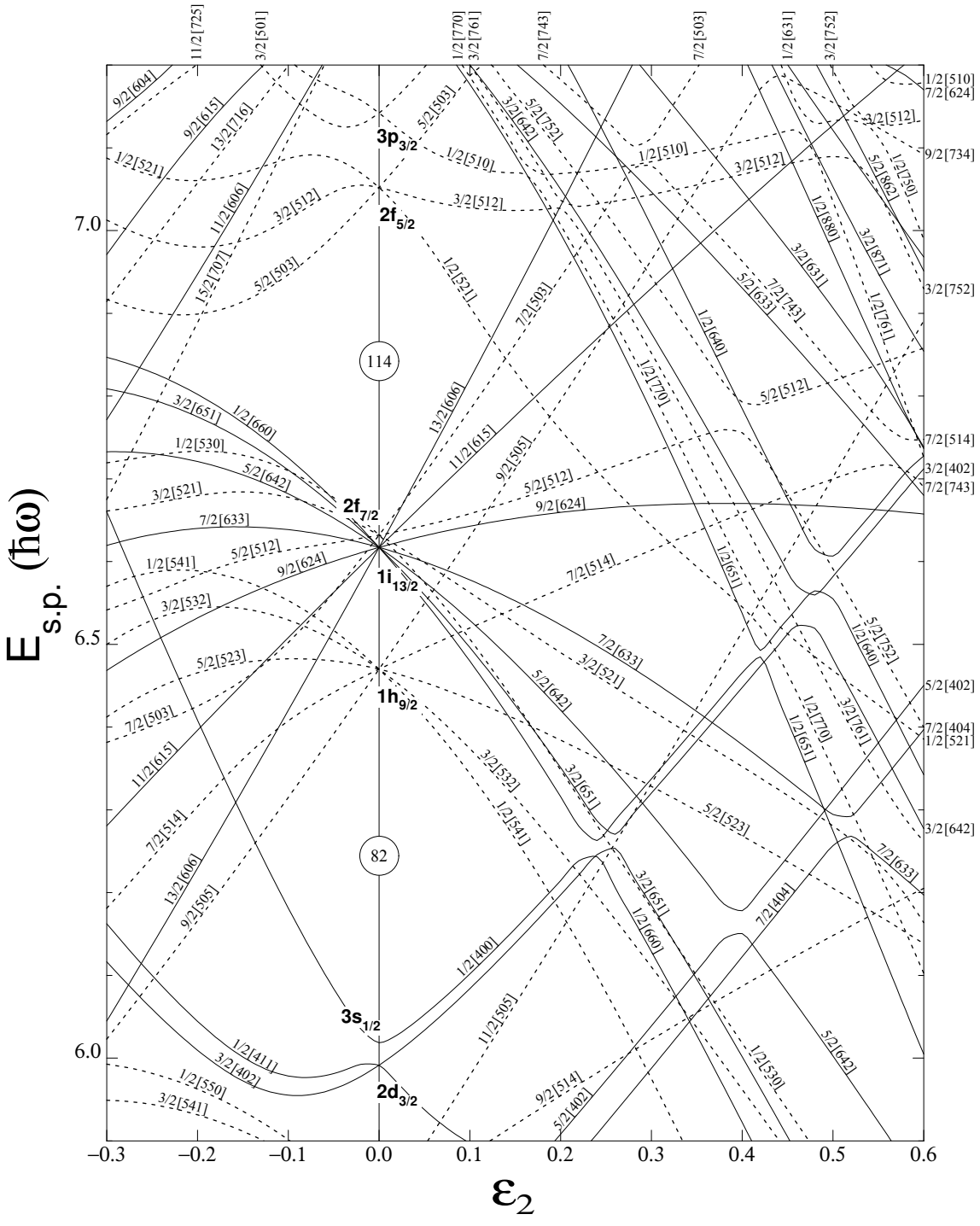

Figure 4.19: A Nilsson diagram appropriate for the $Z \sim N \sim 82$ region showing how the degeneracy of the spherical shell model states is relieved as a function of quadrupole deformation ϵ_2. This figure is reproduced from the *Table of Isotopes* [44].

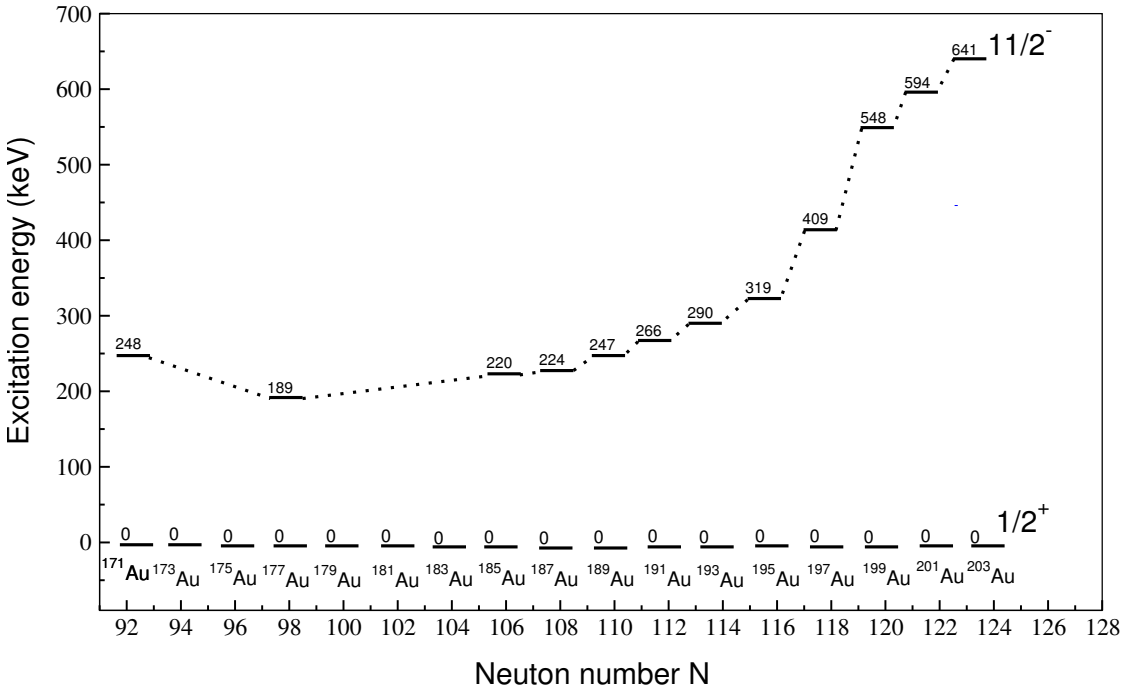

Figure 4.20: The excitation energy of the $11/2^-$ states associated with $\pi h_{11/2}^{-1}$ proton-hole structure as a function of neutron number in the odd-A Au isotopes.

linking transitions could suggest that the $13/2^+$ band head is only marginally higher in excitation energy than the states it feeds. Assuming that the unseen low-energy transitions have an intensity balance with the subsequent transitions in the decay path observed in JUROGAM the number of counts in the γ-ray peaks N_{counts} would be given by

$$N_{counts} = \frac{I_{(T,d)}\eta_f}{1+\alpha_f}, \tag{4.4}$$

where $I_{(T,d)}$ is the intensity of the transition depopulating the $13/2^+$ band head while η_f and α_f are the detection efficiency and the internal conversion coefficient[1] of the unseen transitions, respectively. The number of counts estimated as a function of transition energy is shown in Fig. 4.22.

The assumed parity-changing E1 transitions to the $(11/2^-)$ and $(13/2^-)$ states that are depopulated by the 319 keV and 290 keV transitions, respectively show that the number of counts in the γ-ray peaks increases rapidly above 40 keV. Figure 4.22 shows the extreme cases obtained by assuming either a pure M1 or E2 multipolarity for the transition feeding

[1]All internal conversion coefficients in this work have been taken from BRICC [85].

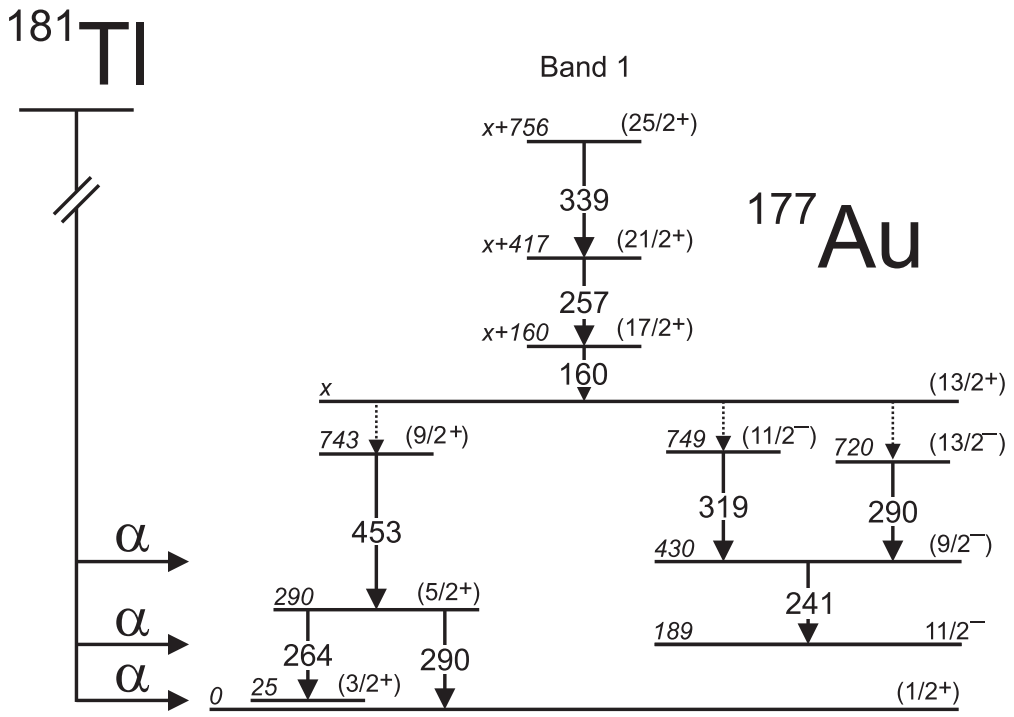

Figure 4.21: Partial level scheme showing the decay paths from the $13/2^+$ state the $11/2^-$ isomer and the $1/2^+$ ground state.

the 743 keV level. The curve is shallow for both multipolarities but increases sharply as a function of energy. The estimates shown in Fig 4.22 constrain the $13/2^+$ excitation energy to be no more than 40 keV above the 749 keV $(11/2^-)$ level. The curves in Fig. 4.22 reflect the poor detection efficiency for low-energy γ rays, which are stopped by the aluminium can surrounding the HPGe crystal in the JUROGAM spectrometers. The estimates also show the dominance of the internal conversion process for low-energy transitions in this heavy nucleus.

The excitation energies of the intruder band heads in this mass region have a parabolic dependence on the neutron number. Figure 4.23 shows the variation of the $13/2^+$ state excitation energy relative to the $9/2^-$ state [3]. The $9/2^-$ reference is chosen since the decay paths from the $i_{13/2}$ intruder to the ground state have not been established completely across the range of isotopes. The range of values deduced for the $13/2^+$ excitation energy in ^{177}Au appear to fit the systematic trend with respect to neutron number. It is clear that the parabola for the $i_{13/2}$ intruder states minimises below the neutron-midshell

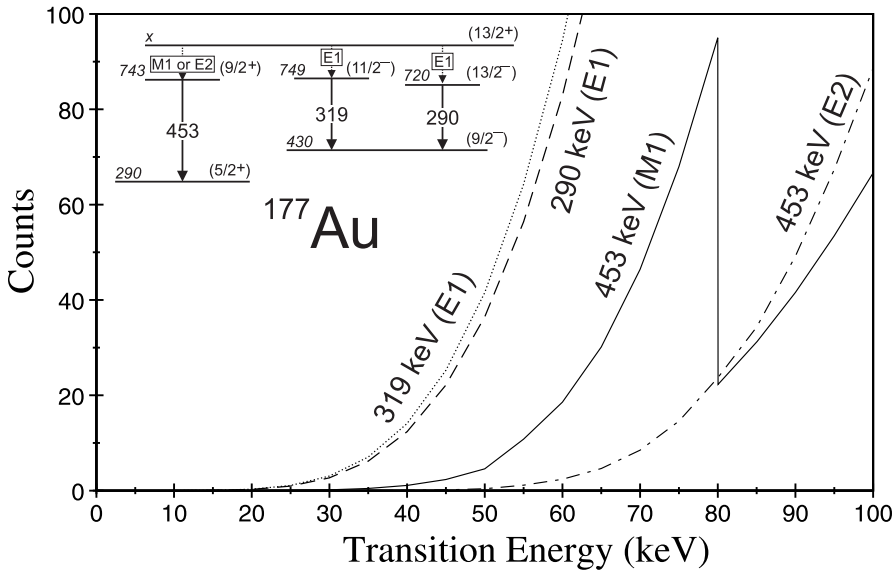

Figure 4.22: Peak area estimates for γ-ray transitions depopulating the $13/2^+$ state. The calculations assume a single-step decay with an intensity that balances with the subsequent transition in the decay path. The estimates are labelled by the multipolarity of the transition decaying from the $13/2^+$ state and the energy of the subsequent transition. The inset shows a partial level scheme indicating the decay paths and assigned multipolarities.

(N=104). Figure 4.24 shows the variation of the collective levels in the $i_{13/2}$ intruder band as a function of neutron number. The excitation energy of the $17/2^+$, $21/2^+$ and $25/2^+$ states decrease smoothly with neutron number down to $N = 98$. The in-band transition energies increase sharply below N=98 perhaps indicating a lower deformation resulting in a higher excitation energy of the $i_{13/2}$ intruder configuration. Thus it is likely that the $i_{13/2}$ intruder parabola reaches a minimum at $N = 98$.

The kinematic moment of inertia can be extracted from the level scheme and provides information on the degree of deformation. Figure 4.25(a) compares the kinematic moment of inertia $\mathcal{J}^{(1)}$ for the prolate bands in ^{186}Pb [11] and ^{188}Pb [10] and the oblate bands in ^{192}Po and ^{194}Po [87]. These bands provide a reference to which the bands in ^{177}Au are compared. The bands in ^{177}Au can be considered as a proton coupled to the ^{176}Pt core [88] or a proton hole coupled to a ^{178}Hg core [89, 90, 91]. Figure 4.25(b) compares the

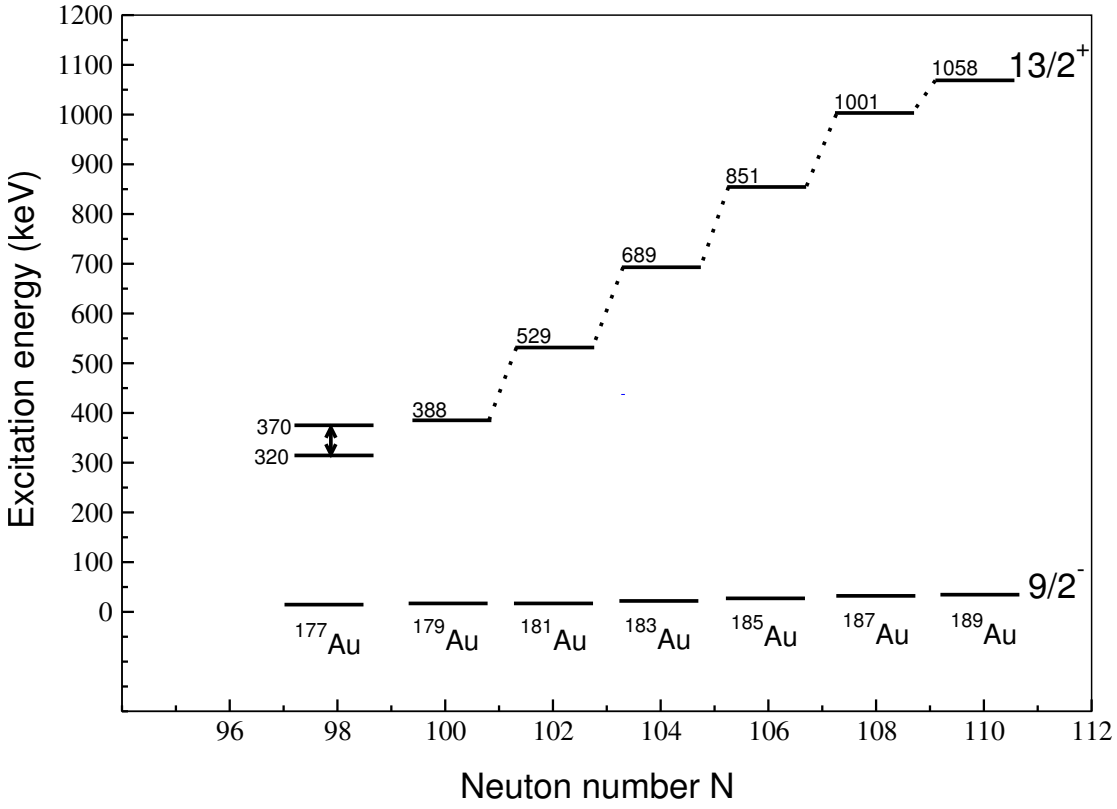

Figure 4.23: The variation of the $\pi i_{13/2}$ intruder band head ($13/2^+$) relative to the $\pi h_{9/2}$ ($9/2^-$) band head. A range of values for the excitation energy of the $13/2^+$ state are given for ^{177}Au. The data for the heavier isotopes is taken from references [86, 3]

cores to the reference bands shown in Fig. 4.25(a). Both cores have oblate ground states that are crossed by a prolate band at low spin. The core configurations are prolate at spins $I > 6$. Figure 4.25(c) shows the kinematic moments of inertia of the intruder bands in ^{177}Au and compares their moments of inertia with the core configurations. The $i_{13/2}$ band, Band 1, has the highest moment of inertia corresponding to a well deformed prolate shape. Band 2 and Band 3 have moments of inertia are very similar to the moments extracted for the cores and are consistent with prolate shapes. The prolate deformation of the ^{176}Pt and ^{178}Hg cores is predicted to be $\beta_2 \sim 0.25$ from potential energy surface calculations [89, 92]. The prolate band in ^{176}Pt has been measured at $\beta_2 = 0.208(13)$ ($\epsilon_2 = 0.184(11)$) [88]. Band 2 and Band 3 in ^{177}Au are likely to have similar deformations.

The band head of the second prolate intruder band, Band 2, lies at an excitation energy of 459 keV. This excitation energy fits with the systematic trends established for

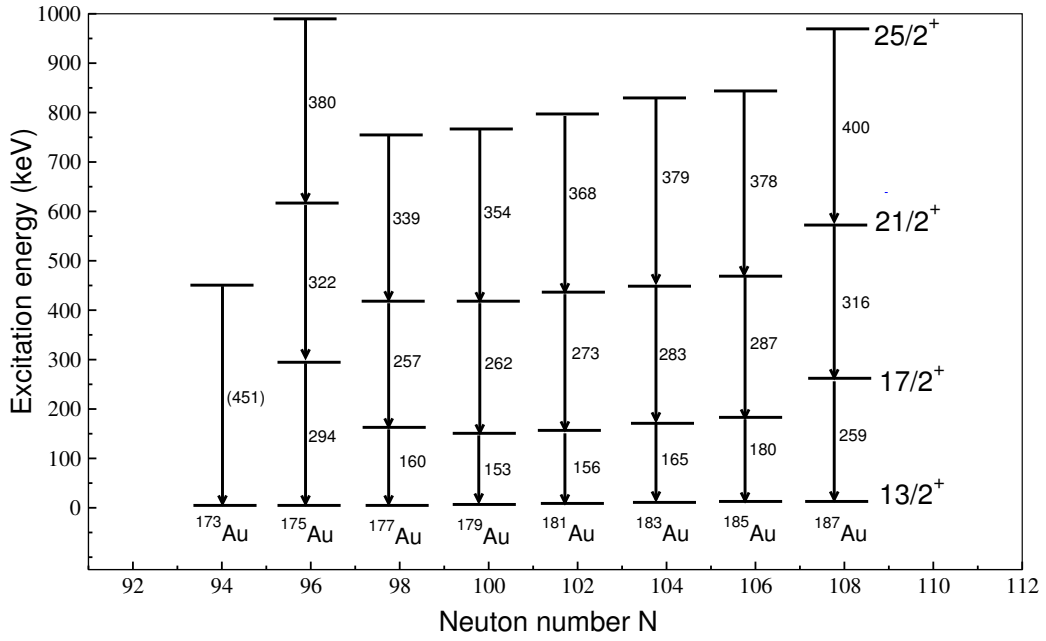

Figure 4.24: The variation of the $17/2^+$, $21/2^+$ and $25/2^+$ states in the $\pi i_{13/2}$ intruder band relative to the $13/2^+$ band head. The data for the heavier isotopes are taken from references [86, 3]

.

the mixed $\pi(f_{7/2} \oplus h_{9/2})$ configurations shown in Figure 4.26 [76, 75]. Figure 4.26 shows a trend of decreasing excitation energy of the $7/2^-$ states relative to $9/2^-$ states with decreasing neutron number down to ^{179}Au ($N = 100$). An slight increase in excitation energy is observed from ^{179}Au to ^{177}Au, which is attributed to passing the minimum of the intruder parabola at $N = 100$. The trend reveals that the energy difference of the $\pi f_{7/2}$ and $\pi h_{9/2}$ single-particle states are closest in energy in ^{179}Au and the $\pi h_{9/2}$ is always lower in excitation energy across the isotopic chain.

The $\pi(f_{7/2} \oplus h_{9/2})$ configuration has decay paths to the positive-parity ground state and the negative-parity $11/2^-$ isomer, see Sec. 4.3.5. Figure 4.27 shows a partial level scheme highlighting the decay paths to both α-decaying states. The decay to the ground state is not fully identified although a 364 keV transition is part of the decay sequence. The observation of the 364 keV transition places some constraints on the various scenarios

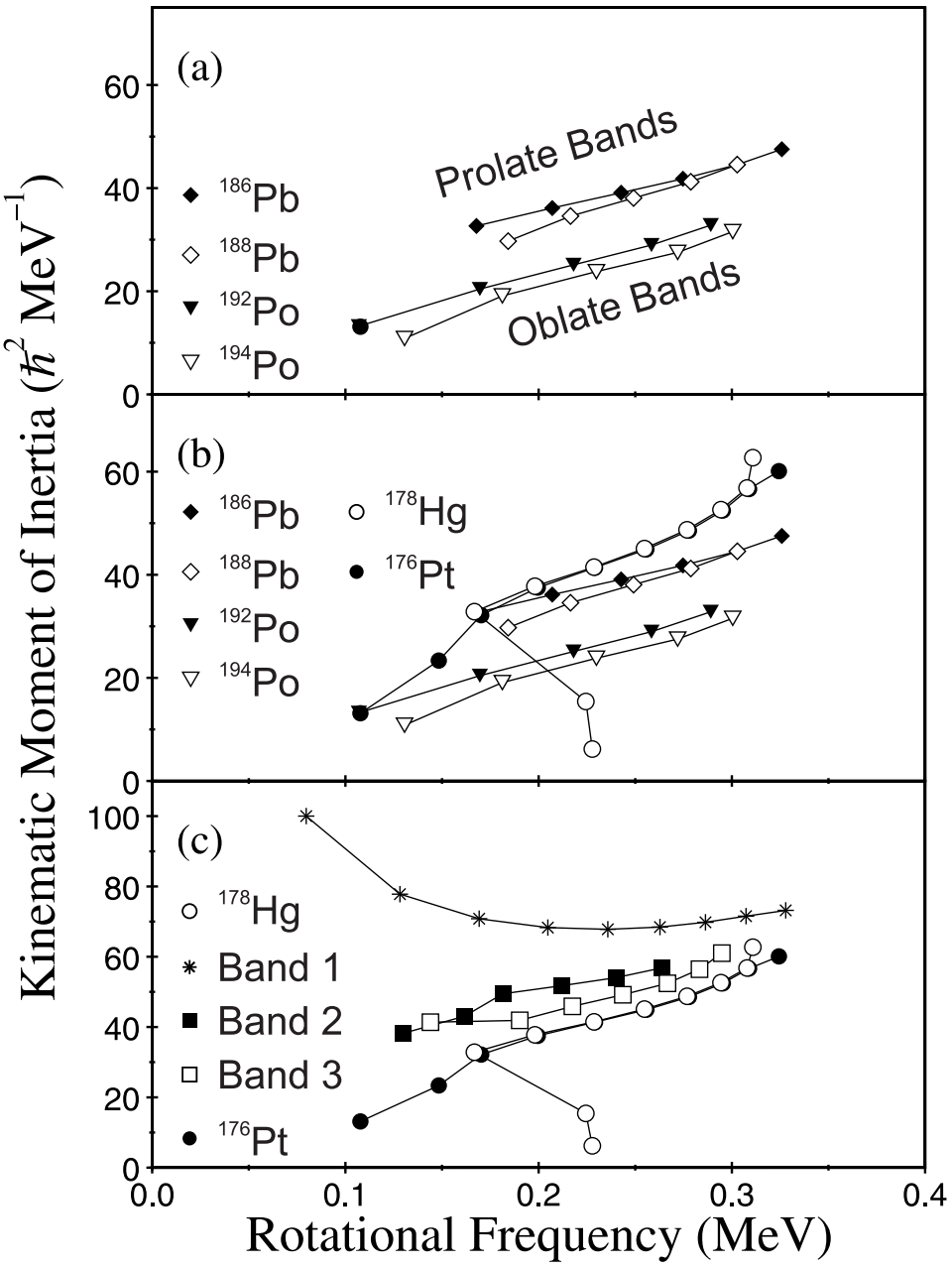

Figure 4.25: Kinematic moments of inertia ($\mathcal{J}^{(1)}$) as a function of rotational frequency. (a) Typical $\mathcal{J}^{(1)}$ values in this mass region for for prolate bands exemplified by ^{186}Pb and ^{188}Pb and oblate bands exemplifed by ^{192}Po and ^{194}Po. (b) Comparison of the $\mathcal{J}^{(1)}$ values for the reference bands shown in panel (a) and the ^{176}Pt and ^{178}Hg cores. (c) Comparison of the $\mathcal{J}^{(1)}$ values for the intruder bands in ^{177}Au with the ^{176}Pt and ^{178}Hg cores.

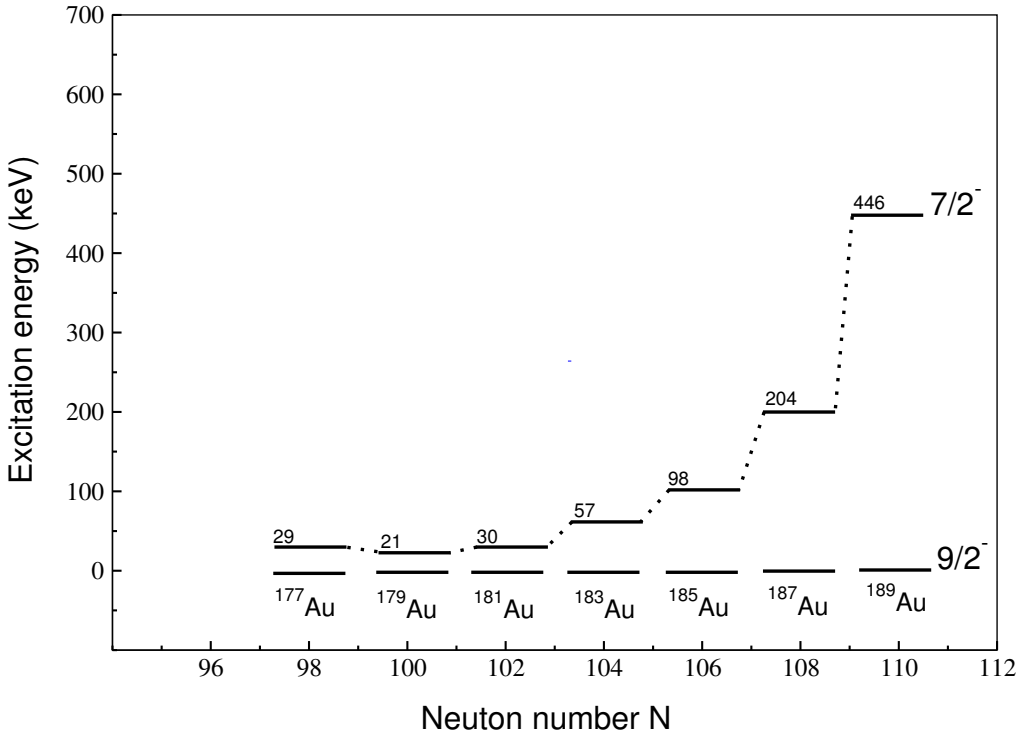

Figure 4.26: The variation of the $\pi(f_{7/2} \oplus h_{9/2})$ intruder band head $(7/2^-)$ relative to the $\pi h_{9/2}$ $(9/2^-)$ band head. The data for the heavier isotopes are taken from reference [16].

for defining the decay path. It is unlikely that the 364 keV transition de-excites the $7/2^-$ band head directly since this would result in a state at low excitation energy, which would open the possibility of γ-ray transitions from the 290 keV or 743 keV levels or maybe even an α decay branch from ^{181}Tl. Since there is no evidence for γ rays or α decays at the appropriate energy for this scenario it seems more likely that the 364 keV transition feeds either the ground state or the first excited state at 25 keV. A direct feeding of the ground state is would lead to a 96 keV γ-ray transition, which is not observed in this analysis. Another hypothesis for a single-step transition is that the 364 keV transition feeds the 25 keV level from an initial state at 389 keV. This would require a single γ-ray transition at 71 keV to complete the decay path. This γ ray would overlap with the K_α X-rays

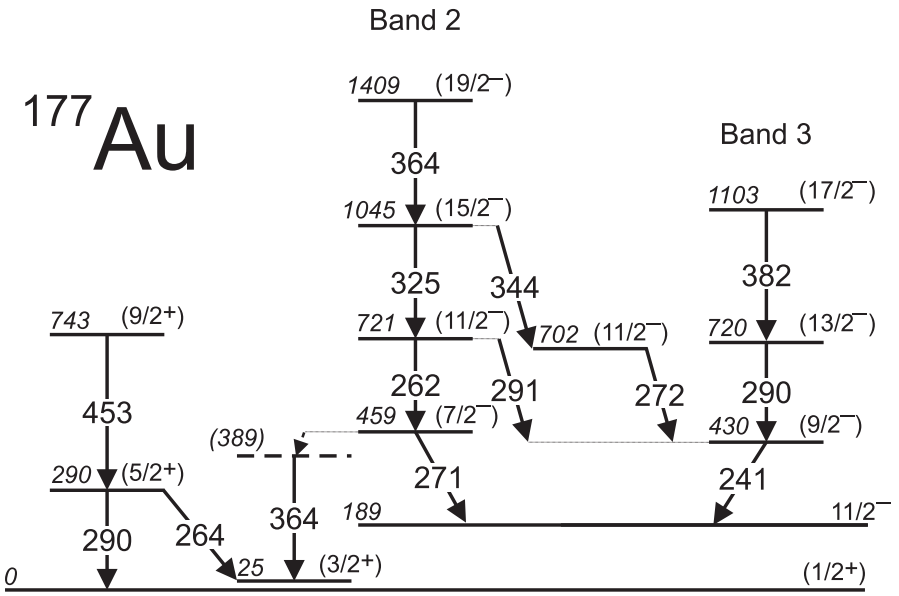

Figure 4.27: Partial level scheme showing the decay paths from the $7/2^-$ state to the $1/2^+$ ground state.

and the present experiment lacks the sensitivity to probe this scenario in detail. It is also possible that the decay path could proceed through several low-energy transitions, which would be difficult to observe due to detection efficiency limitations and competing internal conversion processes.

The state at 430 keV is identified as a $9/2^-$ state in the α-decay measurements of Andreyev *et al.* [73]. The band built on this state, Band 3, is assigned as the $\pi h_{9/2}$ intruder configuration based on the $1/2^-[541]$ Nilsson orbital. The kinematic moment of inertia for this band is shown in Fig. 4.25(c) and is very similar to the $\mathcal{J}^{(1)}$ values extracted for the $\pi(f_{7/2} \oplus h_{9/2})$. These bands are similar in structure and Band 3 is assigned to be a collective band with a prolate shape.

Band 3 is the only intruder structure that does not have a decay path to both the ground state and the $11/2^-$ isomer. The absence of a decay path from Band 3 may imply that a parity-changing transition of higher multipolarity from the $9/2^-$ band head to the low-spin states is required, which is unlikely to be competitive.

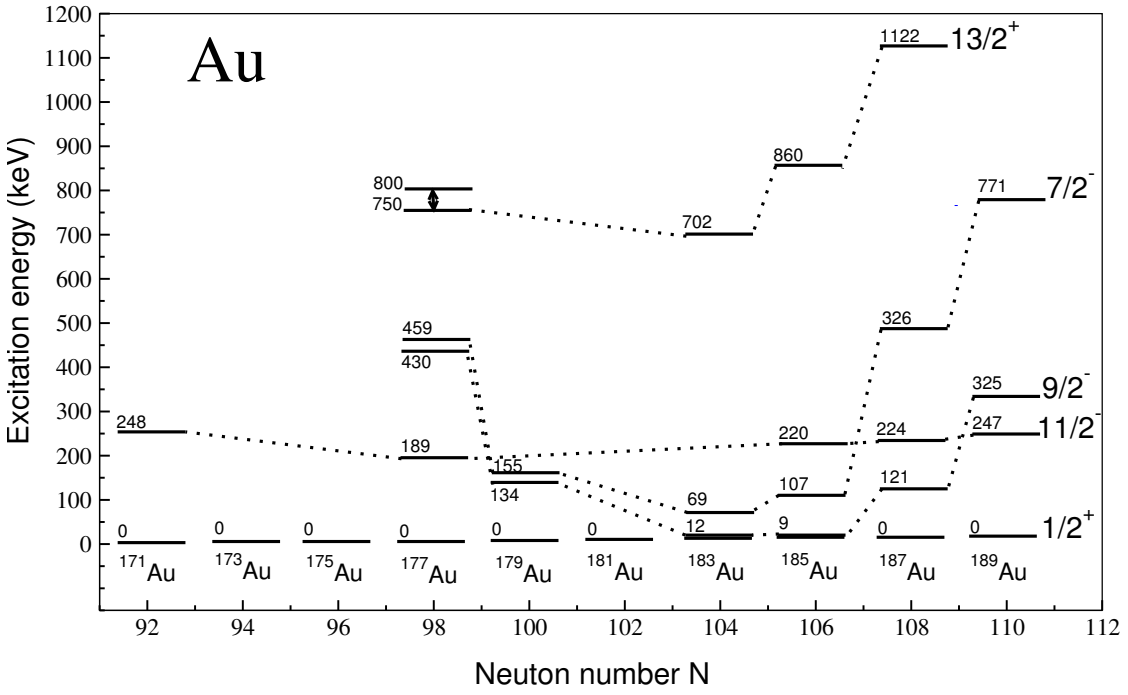

Figure 4.28: Variation intruder band heads in the Au isotopes as a function of neutron number.

In summary, Fig. 4.28 shows the evolution of the intruder parabolas as a function of neutron number relative to the ground state.

4.4.2 The hole states

Band 4 is a unique observation in the neutron-deficient Au isotopes below the neutron midshell since it is a well-developed band that is firmly placed in the level scheme. For the heavier Au isotopes the strongly coupled bands have either a few interconnected states or appear in the level schemes as floating bands of undefined excitation energy [75, 76]. Hence the strongly coupled band in ^{177}Au provides an excellent opportunity to probe shape coexistence and elucidate information on the underlying core structure.

The DCO measurements for the strongly coupled band confirm that the in-band transitions are consistent with a stretched E2 multipolarity assignment, see Fig. 4.9 and Table 4.3. The inter-band γ rays are constrained by the coincidence relations to be $\Delta I = 1$ transitions however the DCO ratios extracted for these transitions are hard to distinguish from the ratios extracted for the in-band (E2) transitions. This could imply that there

must be a positive multipole mixing ratio $\delta_{E2/M1}$. The sign of the multipole mixing ratio is related to the single-particle g-factors such that

$$sign[\delta_{E2/M1}] = sign\left[\frac{g_K - g_R}{Q_0}\right], \tag{4.5}$$

where $g_R \sim Z/A$. Since the strongly coupled band must be built on a deformation aligned (high-Ω) orbital it seems likely that Band 4 is built on a $\pi h_{11/2}$ configuration. An odd proton in the $h_{11/2}$ orbital would give a positive value for the multipole mixing ratio since $g_K < g_R$, which is consistent with the DCO measurements.

In order to provide confirmation of the configuration assignment for the strongly coupled band B(M1:$I \rightarrow I-1$)/B(E2:$I \rightarrow I-2$) ratios of reduced transition probabilities have been measured. Coincidences with the strongest transitions above the state of interest were applied in the recoil-decay tagged $\gamma-\gamma$ matrix correlated with the $11/2^-$ α decay. Ratios of reduced transition probabilities were extracted from experimental γ-ray branching ratios of competing ΔI = 1 and ΔI = 2 transitions using

$$\frac{B(M1: I \rightarrow I-1)}{B(E2: I \rightarrow I-2)} = 0.697\lambda_{out/in}\frac{[E_\gamma(\Delta I=2)]^5}{E_\gamma(\Delta I=1)]^3}, \tag{4.6}$$

where E_γ is given in MeV and the units of the resulting $B(M1: I \rightarrow I-1)/B(E2: I \rightarrow I-2)$ ratio are $(\mu_N/\text{eb})^2$. The measurements are recorded in Table 4.5.

The ratios of reduced transition probabilities $B(M1: I \rightarrow I-1)/B(E2: I \rightarrow I-2)$ extracted from the strongly coupled band are compared with the predictions of the semi-classical formalism of Dönau and Frauendorf [93, 94] in Fig. 4.29. The calculations assumed deformation parameters of $\beta_2 = 0.25$ and $\gamma = 0°$ and use g-factors taken from Woods-Saxon cranking calculations. The experimental ratios are consistent with the assignment of a proton-hole configuration $(\pi h_{11/2})^{-1}$ based on the $11/2^-[505]$ Nilsson state originating from the $h_{11/2}$ subshell. Indeed, the $\pi h_{11/2}$ state is the only deformation aligned high-Ω state near the Fermi surface that could support a strongly coupled band.

Figure 4.30(a) compares the kinematic moment of inertia for the strongly coupled band in ^{177}Au with the $\mathcal{J}^{(1)}$ values of the Pt and Hg cores. The $h^{-1}_{11/2}$ band has moments of

Table 4.5: Measured γ-rays branching ratios λ and $B(M1: I \to I-1)/B(E2: I \to I-2)$ ratios for the strongly coupled band (Band 4) in ^{177}Au.

E_γ (keV)	J_i^π	J_f^π	$B(M1: I \to I-1)/B(E2: I \to I-2)$ $(\mu_N/\text{eb})^2$	λ
171.6	$(17/2)^-$	$(15/2)^-$	1.39(9)	0.99
399.1	$(17/2)^-$	$(13/2)^-$		
203.0	$(19/2)^-$	$(17/2)^-$	1.39(12)	2.23
374.6	$(19/2)^-$	$(15/2)^-$		
220.6	$(21/2)^-$	$(19/2)^-$	0.63(4)	0.70
423.6	$(21/2)^-$	$(17/2)^-$		
232.1	$(23/2)^-$	$(21/2)^-$	0.74(6)	0.70
452.7	$(23/2)^-$	$(19/2)^+$		
245.9	$(25/2)^-$	$(23/2)^-$	0.39(4)	0.32
478.0	$(25/2)^-$	$(21/2)^-$		
258.2	$(27/2)^-$	$(25/2)^+$	3.32(35)	2.50
504.4	$(27/2)^-$	$(23/2)^-$		
270.7	$(29/2)^-$	$(27/2)^-$	0.49(6)	0.33
528.9	$(29/2)^-$	$(25/2)^-$		
280.3	$(31/2)^-$	$(29/2)^-$	1.07(26)	0.66
551.0	$(31/2)^-$	$(27/2)^-$		

inertia that are similar to the moments extracted for the cores. Figure 4.30(b) compares the moments of inertia of Band 4 with the $\mathcal{J}^{(1)}$ values of the intruder bands. The $\mathcal{J}^{(1)}$ values for Band 4 are similar to those for the $\pi(f_{7/2} \oplus h_{9/2})$ (Band 2) and $\pi h_{9/2}$ (Band 3) configurations. Thus the strongly coupled band is assigned to have a prolate shape. Furthermore, the $\mathcal{J}^{(1)}$ for Band 4 shows that there is little signature splitting, which is also consistent with an axially symmetric prolate shape.

The $11/2^-$ α-decaying isomer is interpreted as continuing the trend of a $\pi h_{11/2}$ hole coupled to the $^{A+1}$Hg core. The Hg cores are oblate in their ground states and at low spin [12]. Thus the $11/2^-$ isomer is likely to be an oblate configuration. The $\pi h_{11/2}$ hole should also couple to the excitations of the ^{178}Hg core such as the oblate 2_1^+ state and the 0_2^+ prolate intruder state. Figure 4.31(a) compares the variation of the second $11/2^-$ state as a function of neutron number with the intruder parabola for the 0_2^+ state in the $^{A+1}$Hg cores. The figure highlights the sparseness of data available for the strongly coupled bands in the light Au isotopes. However, if the excited state at 710 keV is the $11/2^-$ band head it follows the extrapolated Hg intruder parabola closely. Thus the strongly coupled

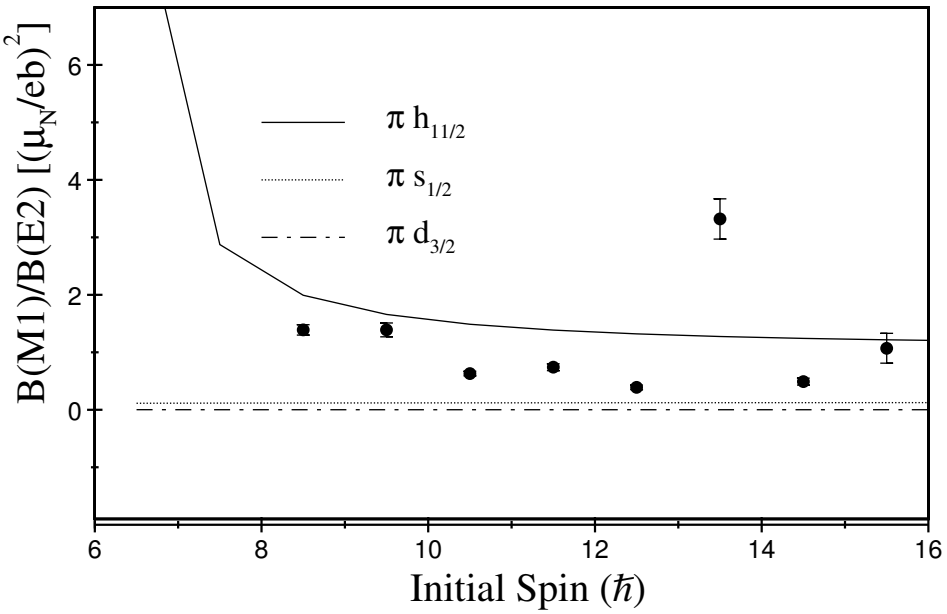

Figure 4.29: Experimental $B(M1 : I \rightarrow I-1)/B(E2 : I \rightarrow I-2)$ ratios of reduced transition strengths as a function of initial spin for ^{177}Au. Measured values (solid circles) are compared with the predictions of the semiclassical model of Dönau and Frauendorf for the $\pi s_{1/2}$ (dotted line), $\pi d_{3/2}$ (dot-dashed line) and $\pi h_{11/2}$ (solid line) configurations.

band is assigned to be the $\pi h^{-1}_{11/2} \otimes ^{178}\mathrm{Hg}(0^+_2)$ configuration. Figure 4.31(b) compares the 713 keV state (524 keV relative to the $11/2^-$ isomer) and the firmly placed $15/2^-$ states in the heavier Au isotopes with the 2^+_1 state in the $^{A+1}$Hg cores. There is good agreement in the excitation energies and so the state at 713 keV is assigned to be an oblate $\pi h^{-1}_{11/2} \otimes ^{178}\mathrm{Hg}(2^+_1)$ configuration formed by coupling the odd proton hole to the first 2^+ state in the ^{178}Hg core.

The low-lying oblate states in the ^{178}Hg core are crossed by $2p{-}4h$ prolate intruder configurations at low spin ($I \sim 6\hbar$), see Fig. 4.30(a). The situation is similar in ^{177}Au since the prolate strongly coupled band decays to oblate $11/2^-$ and $15/2^-$ states. If the 710 keV state is the $11/2^-$ band head and the 521 keV γ ray is a $I \rightarrow I$ transition that connects a prolate excited state to an oblate isomer there is a possibility for an electric

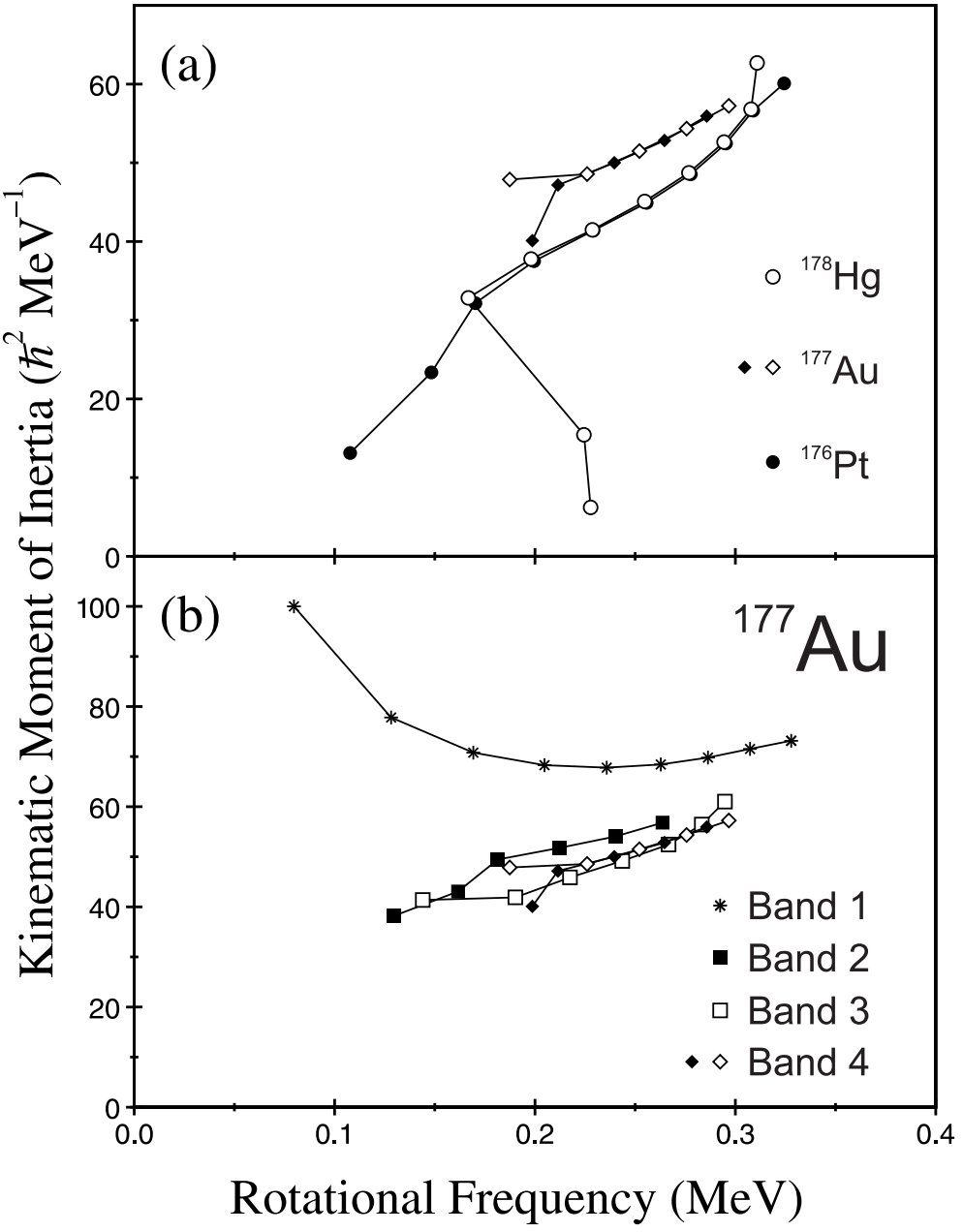

Figure 4.30: Kinematic moments of inertia ($\mathcal{J}^{(1)}$) as a function of rotational frequency. (a) Comparison of the $\mathcal{J}^{(1)}$ values for the strongly coupled band in ^{177}Au with those extracted for the ^{176}Pt and ^{178}Hg cores. (b) Comparison of the $\mathcal{J}^{(1)}$ values for Band 4 and the intruder bands in ^{177}Au.

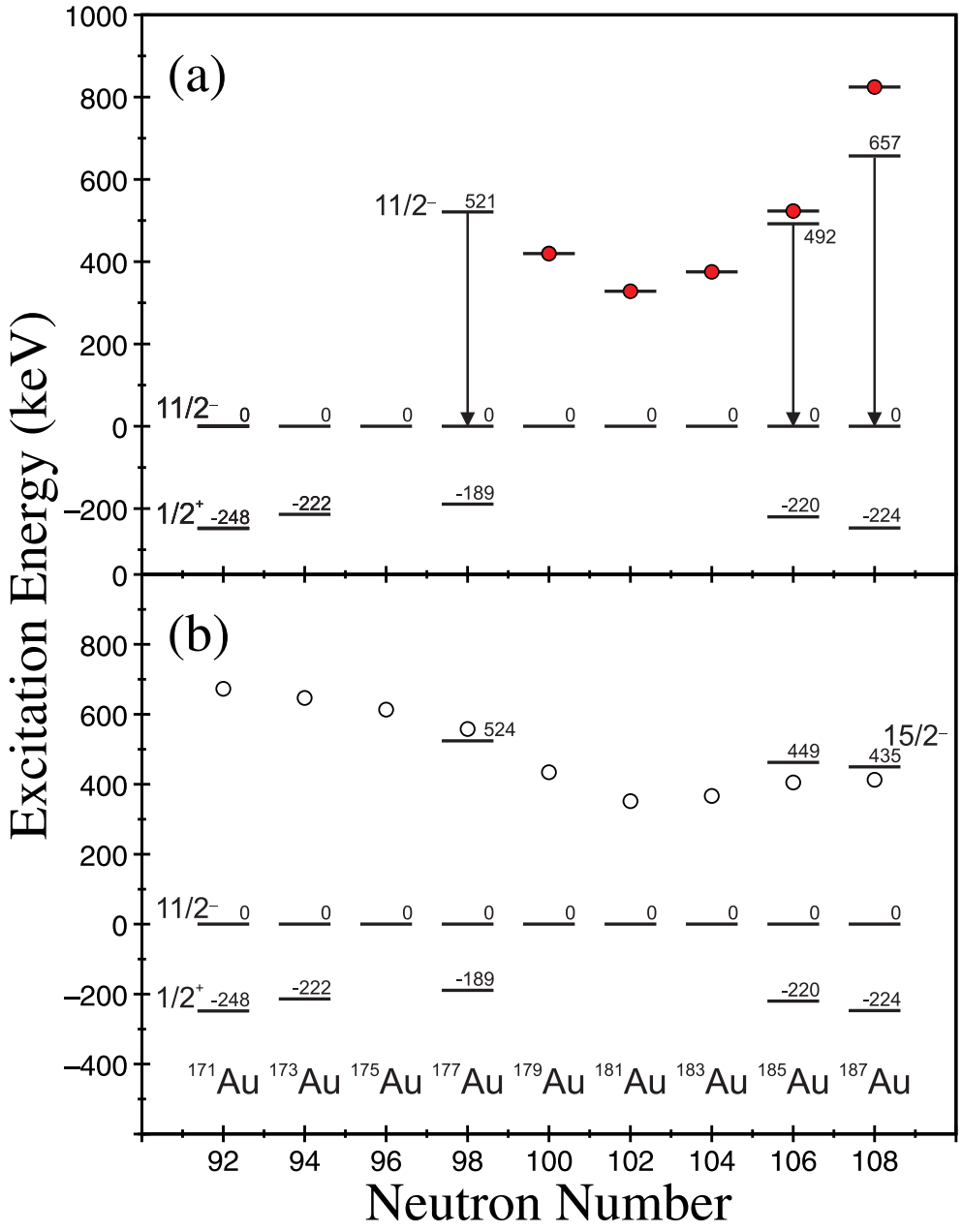

Figure 4.31: Energy level systematics of the light odd-A Au isotopes. The ground state $1/2^+$ states and excited $11/2^-$ states are displayed. The α-decaying $11/2^-$ isomer is used as a reference level. (a) Excitation energy comparison of the second $11/2^-$ states in the Au isotopes with the 0_2^+ states in the $^{A+1}$Hg cores (filled red circles with horizontal lines). Alternative spin and parity assignments for the 521 keV state in ^{177}Au are discussed in the text. (b) Excitation energy comparison of the $15/2^-$ states in the Au isotopes with the 2_1^+ states in the $^{A+1}$Hg cores (open circles).

Table 4.6: The contribution of the internal conversion components of various transitions to the measured $K_{\alpha+\beta}$ X-ray yields.

Label	Gate	Conversion contribution to X-ray yield
A	521 keV	$I_{399} + I_{227} + I_{172} + I_E + I_F + I_G$[1]
B	399 keV	$I_{521} + I_E + I_G$
C	228 keV	$I_{521} + I_D + I_E + I_F + I_G$
D	172 keV	$I_{521} + I_{227} + I_E + I_G$

monopole contribution to the transition intensity. The measurement of electric monopole (E0) transitions between $I_i \rightarrow I_f$ where $I_i = I_f$ provides important information on coexisting states since the monopole strengths are sensitive to mixing between coexisting states and changes in the charge distribution of the nucleus [95]. Mixed E0+M1+E2 transitions have been identified in the neutron-deficient nuclides, ^{185}Au$_{106}$ and ^{187}Au$_{108}$ proceeding from $11/2^-_2$ to the $11/2^-_1$ states, which arise from coupling a single $h_{11/2}$ proton hole to the excitations of the respective Hg and Pt cores [18].

The presence of electric monopole transitions between $I \rightarrow I$ transitions can also be indicated by an imbalance in the γ-ray intensity of transitions feeding and depopulating an excited state. To obtain a reliable feeding intensity for the excited $11/2^-$ state in ^{177}Au it is necessary to consider the total transition intensity comprising both conversion electron and γ-ray emission. A converted transition is followed by the emission of X rays arising from the subsequent rearrangement of atomic electrons. Thus, the internal conversion coefficients can be deduced indirectly from the K X-ray intensities. There are many transitions in the level scheme that proceed by internal conversion and contribute to the K X-ray peak so it is crucial to understand the character of the transitions directly feeding the band head. Since the band is strongly coupled, the 399 keV transition is compelled to be an electric quadrupole (E2) transition while the 228 keV interband transition is likely to be a mixed M1/E2 transition. The K X-ray yield arising from the conversion of the 228 keV transition can be deduced by measuring the K X-ray yields from different coincidence spectra and defining a set of simultaneous equations that can be solved to isolate the individual contribution. Figure 4.32 shows a schematic level scheme and Table 4.6 lists the contributions of internally converted transitions to the K X-ray yields. The difference

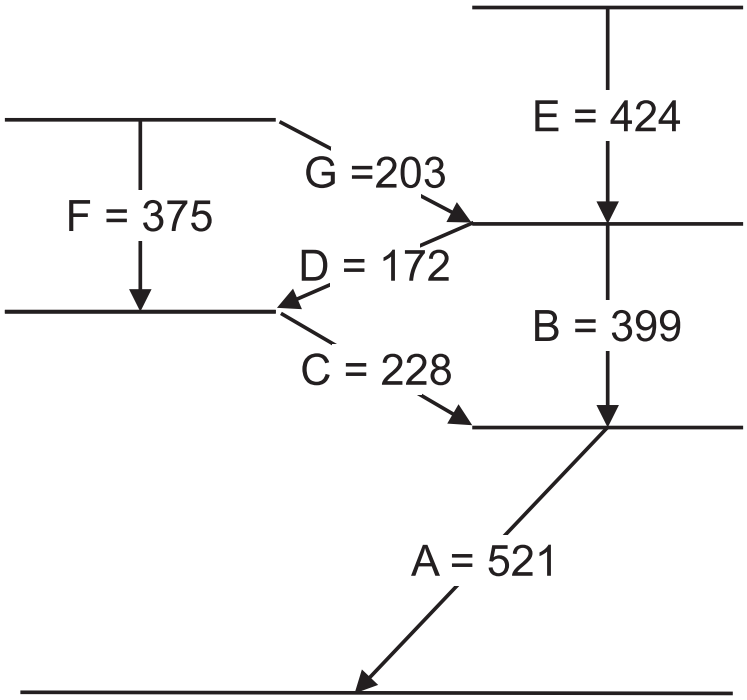

Figure 4.32: Schematic level scheme to aid the deduction of the internal conversion coefficient for the 228 keV transition.

between the summed (K_α and K_β) X-ray peaks in the coincidence spectra D and B isolate the internal conversion coefficient for the 227 keV transition such that

$$\frac{[I(K_\alpha)/\varepsilon_{K_\alpha} + I(K_\beta)/\varepsilon_{K_\beta}]_{172}}{\varepsilon_{172}} - \frac{[I(K_\alpha)/\varepsilon_{K_\alpha} + I(K_\beta)/\varepsilon_{K_\beta}]_{399}}{\varepsilon_{399}} = \left(\frac{\alpha_K(228)}{\omega_K}\right), \quad (4.7)$$

where ε_x is the detection efficiency for transition x keV and ω_K is the K fluorescence factor that accounts for the competition from Auger emission. The ω_K factor was estimated to be 0.952(6) using the semi-empirical formula of Hagedoorn and Wapstra [96] such that

$$\left(\frac{\omega_K}{1-\omega_K}\right)^{1/4} = A + BZ + CZ^3, \quad (4.8)$$

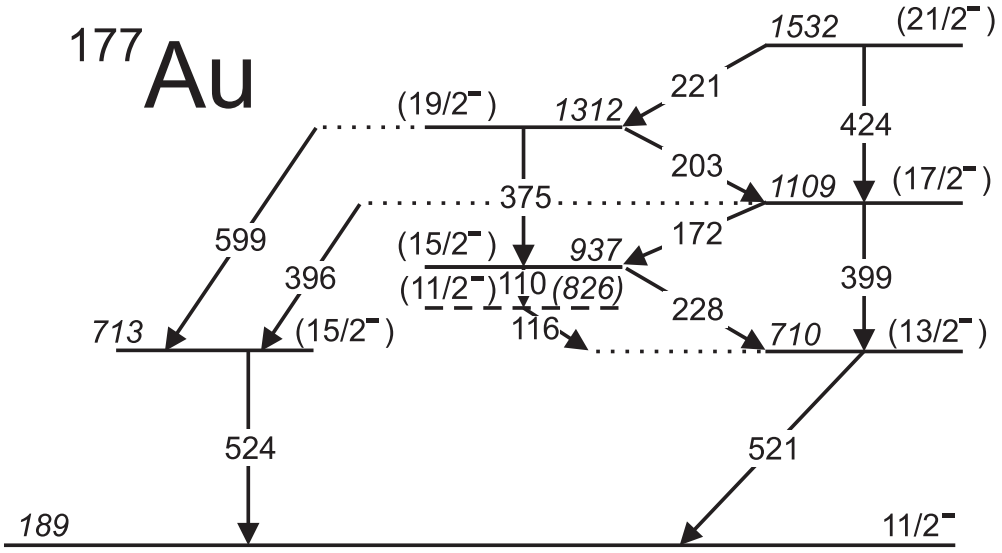

Figure 4.33: Partial level scheme showing the decay paths from the strongly coupled band in ^{177}Au. A candidate two-step decay path from the $15/2^-$ state comprising the 110 keV and 116 keV transitions seen in the tagged singles spectrum is included for the purpose of discussion. These transitions cannot be established in the coincidence analysis firmly and are labelled as tentative.

where Z is the atomic number. The measured difference in K X-ray intensity leads to a conversion coefficient for the 228 keV transition of 0.58(23), which compares well with the BRICC estimates for a pure M1 transition of 0.588(9) [85]. On the basis of these measurements it is assumed that the 228 keV is a pure M1, which represents a worst case scenario for establishing the feeding intensity. If an E0 component is present in the 521 keV transition, the transition intensity should be lower than the sum of the transition intensities of the direct feeding transitions. It is apparent from these measurements that the intensity of the 521 keV is larger than the sum of the feeding transition intensities. Indeed there is a small missing intensity that could indicate another feeding path to the 710 keV level. The intensity measurements suggest that there is no tangible E0 component in the 521 keV transition. It would seem likely from these measurements that the 710 keV

state is not $11/2^-$ thereby removing the possibility of an electric monopole component.

The whereabouts of the $11/2^-$ band head remains an open question. Figure 4.33 shows a partial level scheme that outlines a hypothesis that the $11/2^-$ band head is pushed to higher excitation energy by mixing with the $11/2^-$ isomeric state. This would result in the $13/2^-$ state being the lowest energy state in Band 4 and could explain the absence of an electric monopole component to the 521 keV transition. The level scheme allows the possibility of other transitions de-exciting the 937 keV ($15/2^-$) state and provides a mechanism for explaining the missing feeding intensity to the 710 keV level. The spectra in Fig. 4.6(b) and Fig. 4.17(b) are both correlated with the $11/2^-$ α decay and show a γ ray at 116 keV, which could be a candidate for the $15/2^- \rightarrow 11/2^-$ or $11/2^- \rightarrow 13/2^-$ transition. This matter cannot be resolved in the present experiment and is left to be resolved in future work.

Chapter 5

Summary

This thesis reports the results from a recoil-decay tagging experiment performed at University of Jyväskylä Accelerator Laboratory using the JUROGAM γ-ray spectrometer in conjunction with the RITU gas-filled separator and GREAT focal plane spectrometer. Highly selective recoil-decay correlations with the ground-state and $11/2^-$ α decays of ^{177}Au allowed the unambiguous assignment of γ-ray transitions to this proton-unbound nucleus. A detailed $\gamma - \gamma$ coincidence analysis revealed several new collective structures. In addition to the known $\pi i_{13/2}$ prolate band, bands based on the $\pi f_{7/2} \oplus h_{9/2}$ and $\pi h_{9/2}$ intruder configurations were identified for the first time. Kinematic moments of inertia suggest that these collective structures are built on similar deformations to their underlying ^{176}Pt and ^{178}Hg cores ($\beta_2 = 0.25$).

It has been possible to link all bands with the exception of the $\pi i_{13/2}$ band into the level scheme thereby fixing the excitation energies of the different configurations. This provides a useful constraint on the theoretical models aiming to reproduce single-particle energies near the proton drip line. The intruder excitation energies follow parabolas as a function of neutron number. This work reveals that the band head configurations in ^{177}Au are at higher energies than the heavier odd-A isotope ^{179}Au, which fixes the parabola minimum to be at $N = 100$. The $\pi i_{13/2}$ band is not linked into the level scheme, however it has been possible to use intensity balance arguments to limit the excitation energy of this intruder structure to be in the range 750 keV - 850 keV. The $\pi i_{13/2}$ intruder configuration in ^{177}Au

has the highest excitation energy of the Au isotopes below the neutron midshell reflecting the lower average deformation of ^{177}Au relative to the heavier isotopes.

The $\pi f_{7/2} \oplus h_{9/2}$ and $\pi h_{9/2}$ intruder configurations are assigned to be prolate structures on the basis of their kinematic moments of inertia. This work fixes the minimum excitation energy difference between the $7/2^-$ and $9/2^-$ band heads at $N = 100$ and confirms that the energies of these configurations do not invert *i.e.* the $\pi h_{9/2}$ orbital is always at a lower excitation energy than the $\pi f_{7/2}$ orbital in the Au isotopes. The intensity balances in the decay paths from the $7/2^-$ and $9/2^-$ band heads imply that they are isomeric and have nanosecond lifetimes. There is some complementary evidence from SAGE experiments to support this assertion. It has also been demonstrated that both the $\pi i_{13/2}$ and $\pi f_{7/2} \oplus h_{9/2}$ bands have decay paths from their band heads to the positive-parity ground state and the negative-parity $11/2^-$ isomer, which is an unusual feature. The $\pi h_{9/2}$ intruder decays exclusively to the $11/2^-$ isomeric state.

Excited states formed by coupling the odd $\pi h^{-1}_{11/2}$ proton hole to excitations of the ^{178}Hg core have been identified. This work has established an oblate $\pi h^{-1}_{11/2} \otimes ^{178}\mathrm{Hg}(2^+_1)$ state and a prolate strongly coupled band based on the $\pi h^{-1}_{11/2} \otimes ^{178}\mathrm{Hg}(0^+_2)$ configuration. The strongly coupled band is unusual in the neutron-deficient Au isotopes since it extends to high spin and is linked into the level scheme, which fixes the excitation energies of the excited states. An intensity balance measurement suggest that there is no electric monopole component to the 521 keV linking transition that connects the lowest observed state in the band to the $11/2^-$ isomer. This implies that the lowest level in the strongly coupled band is not the $11/2^-$ band head. The $11/2^-$ band head is hypothesised to be pushed to a higher excitation energy above the $13/2^-$ state by mixing with the $11/2^-$ isomer and possible other nearby states. The presence of electric monopole transitions in ^{177}Au is unresolved in this work. However, there are exciting possibilities for future experiments investigating ^{177}Au and nearby nuclei using the SAGE γ-ray - conversion electron spectrometer with selective tagging techniques to detect this emissions directly. The work presented in this thesis provides some encouragement for future experiments aimed at identifying new structures in other odd-Z nuclei near the proton drip line.

Bibliography

[1] A. Bohr and B.R. Mottelson, *Nuclear Structure Volume 1: Single-Particle Motion*. W. A. Benjamin Inc, New York, USA, 1969.

[2] A. Bohr and B.R. Mottelson, *Nuclear Structure Volume 2: Nuclear Deformation*. W. A. Benjamin Inc, New York, USA, 1975.

[3] K. Heyde and J. L. Wood *Rev. Mod. Phys.*, vol. 83, p. 1467, Nov 2011.

[4] T.E. Cocolios *et al. Phys. Rev. Lett*, vol. 106, p. 052503, 2011.

[5] J.E. García-Ramos, V. Hellemans and K. Heyde *Phys. Rev. C.*, vol. 84, p. 014331, 2011.

[6] K. Nomura, R. Rodriguez-Guzman, and L. M. Robledo *Phys. Rev. C.*, vol. 87, p. 064313, 2013.

[7] M. Bender, P.-H. Heenen, and P.-G. Reinhard *Rev. Mod. Phys.*, vol. 75, p. 121, 2003.

[8] J.M. Yao, M. Bender, and P.-H. Heenen *Phys. Rev. C.*, vol. 87, p. 034322, 2013.

[9] J. Bonn, G. Huber, H.-J. Kluge, L. Kugler, and E.W. Otten, *Phys. Lett. B.*, vol. 38, p. 308, 1972.

[10] G.D. Dracoulis, G.J. Lane, A.P. Byrne, T. Kibédi, A.M. Baxter, A.O. Macchiavelli, P. Fallon, and R.M. Clark *Phys. Rev. C.*, vol. 69, p. 054318, 2004.

[11] A.N. Andreyev *et al. Nature*, vol. 405, p. 430, 2000.

[12] N. Bree *et al.* vol. 112, p. 162701, 2014.

[13] P.M. Davidson, G.D. Dracoulis, T. Kibédi, A.P. Byrne, S.S. Anderssen, A.M. Baxter, B. Fabricius, G.J. Lane, and A.E. Stuchbery. *Nucl. Phys.*, vol. A 657, p. 219, 1999.

[14] T. Kibedi, G.D. Dracoulis, A.P. Byrne and P.M. Davidson *Nucl. Phys.*, vol. A 567, no. 1, p. 183, 1994.

[15] T. Kibedi, G.D. Dracoulis, A.P. Byrne, and P.M. Davidson *Nucl. Phys.*, vol. A 688, no. 1, p. 669, 2001.

[16] M. Venhart *et al. Phys. Lett. B*, vol. 695, p. 82, 2011.

[17] D. Rupnik, E. F. Zganjar, J. L. Wood, P. B. Semmes and P. F. Mantica *Phys. Rev. C.*, vol. 58, p. 771, 1998.

[18] C.D. Papanicolopulos, M.A. Grimm, J.L. Wood, E.F. Zganjar, M.O. Kortelahti, J.D. Cole, and H.K. Carter *Z. Phys. A.*, vol. 330, p. 371, 1988.

[19] M.O. Kortelahti, E.F. Zganjar, H.K. Carter, C.D. Papanicolopulos, M.A. Grimm, and J.L. Wood *J. Phys. G.*, vol. 14, p. 1361, 1988.

[20] F.G. Kondev *et al. Phys. Lett. B*, vol. 512, p. 268, 2001.

[21] H. Watkins *et al. Phys. Rev. C.*, vol. 84, p. 051302, 2011.

[22] K.-H. Schmidt, R. S. Simon, J.-G. Keller, F. P. Hessberger, G. Münzenberg, B. Quint, H.-G. Clerc, W. Schwab, U. Gollerthan and C.-C. Sahm *Phys. Lett. B*, vol. 168, p. 39, 1986.

[23] R. S. Simon, K.-H. Schmidt, F. P. Hessberger, S. Hlavac, M. Honusek, G. Münzenberg, H.-G. Clerc, U. Gollerthan and W. Schwab *Z. Phys. A*, vol. 325, p. 197, 1986.

[24] E. S. Paul, P. J. Woods, T. Davinson, R. D. Page, P. J. Sellin, C. W. Beausang, R. M. Clark, R. A. Cunningham, S. A. Forbes, D. B. Fossan, A. Gizon, J. Gizon, K. Hauschild, I. M. Hibbert, A. N. James, D. R. LaFosse, I. Lazarus, H. Schnare, J. Simpson, R. Wadsworth, and M. P. Waring *Phys. Rev. C*, vol. 51, p. 78, Jan 1995.

[25] C. W. Beausang and J. Simpson. *J. Phys. G*, vol. 22, p. 527, 1996.

[26] T. Enqvist, P. Heikkinen, H. Kettunen, P. Kuusiniemi, M. Leino, A. -P. Leppanen, C. Scholey and J. Uusitalo *Nucl. Instrum. Methods. Phys. Res. B*, vol. 204, p. 138, 2003.

[27] M. Leino *Nucl. Instrum. Methods. Phys. Res. B*, vol. 126, p. 320, 1997.

[28] J. Uusitalo *et al. Nucl. Instrum. Methods. Phys. Res. B*, vol. 204, p. 638, 2003.

[29] J. Sarén, J. Uusitalo, M. Leino and J. Sorri *Nucl. Instrum. Methods. Phys. Res. A*, vol. 654, p. 508, 2011.

[30] R. D. Page, A. N. Andreyev, D. E. Appelbe, P. A. Butler, S. J. Freeman, P. T. Greenless, R. -D. Herzberg, D. G. Jenkins, G. D. Jones, P. Jones, D. T. Joss, R. Julin, H. Kettunen, M. Leino, P. Rahkila, P.H. Regan, J. Simpson, J. Uusitalo, S. M. Vincent and R. Wadsworth *Nucl. Instrum. Methods. Phys. Res. B*, vol. 204, p. 634, 2003.

[31] I. H. Lazarus *et al. IEEE Trans. Nucl. Sci.*, vol. 48, no. 3, p. 567, 2001.

[32] C. F. von Weizsäcker. *Z. Phys.*, vol. 96, p. 431, 1935.

[33] H. A. Bethe and R. F. Bacher *Rev. Mod. Phys.*, vol. 8, p. 82, 1936.

[34] N. Bohr and F. Kalckar *Kgl. Danske Videnskab. Selskab, Mat-fys. Medd.*, vol. 14, p. 10, 1937.

[35] M. G. Mayer *Phys. Rev.*, vol. 74, p. 235, 1948.

[36] O. Haxel, J. H. D. Jensen and H. E. Suess *Phys. Rev.*, vol. 75, p. 1766, 1949.

[37] R. D. Woods and D. S. Saxon *Phys. Rev.*, vol. 95, p. 577, 1954.

[38] E. S. Paul *Private Communication.*

[39] M. G. Mayer *Phys. Rev.*, vol. 75, p. 1969, 1949.

[40] P. Ring and P. Schuck, *The Nuclear Many-Body Problem.* Springer, 2004.

[41] D. L. Hill and J. A. Wheeler *Phys. Rev.*, vol. 89, p. 1102, 1953.

[42] Z. Szymanski, *Fast Nuclear Rotation.* Clarendon Press, Oxford, UK, 1983.

[43] S. G. Nilsson *Kgl. Danske Videnskab. Selskab, Mat-fys. Medd.*, vol. 29, p. 16, 1954.

[44] R. B. Firestone and and V.S. Shirley, *Table of Isotopes 8th Edition*, vol. 2. John Wiley and Sons Inc.

[45] K. E. G. Löbner, M. Vetter and V. Hönig *Nucl. Data. Tables. A*, vol. 7, p. 495, 1970.

[46] J. M. Blatt and V. F. Weisskopf, *Theoretical Nuclear Physics.* Dover Publications Inc, New York, USA, 1952.

[47] H. Frauenfelder, R. M. Steffen, S. R. de Groot, H. A. Tolhoek and W. J. Huiskamp, *Alpha, Beta and Gamma-ray Spectroscopy, Volume 2, edited by K. Siegbahn.* North Holland Publishing Company, New York, USA, 1979.

[48] M. E. Rose, *Alpha, Beta and Gamma-ray Spectroscopy, Volume 2, edited by K. Siegbahn.* North Holland Publishing Company, New York, USA, 1979.

[49] J. H. Hamilton, *Internal Conversion Processes.* Academic Press, New York and London, 1966.

[50] K. S. Krane, *Introductory Nuclear Physics.* John Wiley & Sons, 1988.

[51] G. Gamow *Z. Phys.*, vol. 51, p. 204, 1928.

[52] R. W. Gurney and E. U. Condon *Nature*, vol. 122, p. 439, 1928.

[53] R. W. Gurney and E. U. Condon *Phys. Rev.*, vol. 33, p. 127, 1929.

[54] J. Rasmussen in *Alpha-, Beta- and Gamma-Ray Spectroscopy* (K. Siegbahn, ed.), pp. 701 – 743, Amsterdam: Elsevier, 1968.

[55] D. Rupnik, E. F. Zganjar, J. L. Wood, P. B. Semmes and W. Nazarewicz *Phys. Rev. C.*, vol. 51, p. R2867, 1995.

[56] J. O. Newton, F. S. Stephens, R. M. Diamond, W. H. Kelly and D. Ward *Nucl. Phys.*, vol. A 141, p. 631, 1969.

[57] C. W. Beausang *et al. Nucl. Instrum. Methods. Phys. Res. A*, vol. 313, p. 37, 1992.

[58] G. Duchene *et al. Nucl. Instrum. Methods. Phys. Res. A*, vol. 432, p. 90, 1999.

[59] P. J. Nolan, D. W. Gifford and P. J. Twin. *Nucl. Instrum. Methods. Phys. Res. A*, vol. 236, p. 95, 1985.

[60] L. Hildingsson, C. W. Beausang, D. B. Fossan, W. F. Piel Jr, A. P. Byrne and G. D. Dracoulis. *Nucl. Instrum. Methods. Phys. Res. A*, vol. 252, p. 91, 1986.

[61] D. Seddon, *Private Communication.*

[62] M. Leino *et al. Acta Physica Polonica.*, vol. B 26, p. 309, 1995.

[63] P. Rahkila *Nucl. Instrum. Methods. Phys. Res. A*, vol. 595, pp. 637–642, 2008.

[64] D. C. Radford. *Nucl. Instrum. Methods. Phys. Res. A*, vol. 361, p. 297, 1995.

[65] H. J. Rose and D. M. Brink *Rev. Mod. Phys.*, vol. 39, p. 306, 1967.

[66] K. S. Krane, R. M. Steffen and R. M. Wheeler *Bulletin of the American Physical Society*, vol. 17, p. 928, 1972.

[67] J.L Wood, W. Heyde, K. Nazarewicz, M. Huyse, P. Van Duppen *Phys. Rep.*, vol. 215, p. 101, 1992.

[68] K. Heyde, P Van Isacker, M. Waroquier, J.L Wood, R.A. Meyer *Phys. Rep.*, vol. 102, p. 291, 1983.

[69] J.L. Wood and K. Heyde. *Rev. Mod. Phys.*, vol. 83, p. 1467, 2011.

[70] P.M. Davidson, G.D. Dracoulis, T. Kibedi, A.P. Byrne, S.S. Anderssen, A.M. Baxter, B. Fabricius, G.J. Lane and A.E. Stuchbery *Nucl. Phys.*, vol. A 568, no. 1, p. 90, 1994.

[71] M. O. Kortelahti *et al. J. Phys.*, vol. G 14, p. 1361, 1988.

[72] A. Siivola *et al. Nucl. Phys.*, vol. A 109, p. 231, 1968.

[73] A.N. Andreyev *et al. Phys. Rev.*, vol. C80, p. 024302, 2009.

[74] M. Venhart *et al Phys. Lett.*, vol. B695, p. 78, 2011.

[75] A.J. Larabee *et al. Phys. Lett.*, vol. B169, p. 21, 1986.

[76] W. F. Mueller *et al Phys. Rev.*, vol. C59, p. 2009, 1999.

[77] A.N. Andreyev *et al. in preparation*, 2014.

[78] H. Gauvin, R. L. Hahn, Y. Le Beyec, M. Lefort and J. Livet *Nucl. Phys.*, vol. A208, p. 360, 1973.

[79] C. Cabot, C. Deprun, H. Gauvin, B. Lagarde, Y. Le Beyec and M. Lefort *Nucl. Phys.*, vol. A241, p. 341, 1975.

[80] P. J. Sellin *et al. Z. Phys.*, vol. A338, p. 245, 1991.

[81] R. D. Page *et al. Phys. Rev.*, vol. C53, p. 660, 1996.

[82] F. G. Kondev *Nuclear Data Sheets*, vol. 98, p. 801, 2003.

[83] J. Pakarinen *Eur. Phys. J.*, vol. A50, p. 53, 2014.

[84] A. K. Mistry *Private communication.*

[85] T. Kibedi, T. W. Burrows, M. B. Trzhaskovskaya, P. M. Davidson, and C. W. Nestor., Jr. *Nucl. Instrum. Methods. Phys. Res. A*, vol. 589, p. 202, 2008.

[86] A. Thornthwaite *Private communication.*

[87] K. Helariutta *et al. Eur. Phys. J.*, vol. A 6, p. R1337, 1999.

[88] G. D. Dracoulis, A. E. Stuchbery, A. P. Byrne, A. R. Poletti, S. J. Poletti, J. Gerl and R. A. Bark *J. Phys.*, vol. G12, p. L97, 1986.

[89] M. P. Carpenter *et al. Phys. Rev. Lett*, vol. 78, p. 3650, 1997.

[90] F. G. Kondev *et al. Phys. Rev.*, vol. C61, p. 011303, 2000.

[91] F. G. Kondev *et al. Phys. Rev.*, vol. C62, p. 044305, 2000.

[92] R. Bengtsson, T. Bengtsson, J. Dudek, G. Leander, W. Nazarewicz and J. Y. Zhang *Phys. Lett*, vol. B183, p. 1, 1987.

[93] F. Dönau *et al. Nucl. Phys.*, vol. A471, p. 469, 1987.

[94] F. Dönau and S. Frauendrof *Proceedings of the Conference on High Angular Momentum Properties of Nuclie, Oak Ride, 1982*, vol. , edited by N. R. Johnson (Harwood Academic, New York), p. p143, 1983.

[95] J. L. Wood, E. F. Zganjar, C. De Coster and K. Heyde *Nucl. Phys.*, vol. A 651, p. 323, 1999.

[96] H. L. Hagedoorn and A. H. Wapstra *Nucl. Phys.*, vol. 15, p. 146, 1960.